POLITECNICO
MILANO 1863

SCHOOL OF CIVIL, ENVIRONMENTAL AND LAND MANAGEMENT ENGINEERING
MASTER OF SCIENCE IN ENVIRONMENTAL AND LAND PLANNING ENGINEERING

DESIGNING EFFICIENT RESERVOIR FILLING STRATEGIES USING SEASONAL DROUGHT FORECASTS

Master Thesis by:
Lorenzo Caviglioni
Matr. 875837

Advisor:
Prof. Andrea Castelletti

Co-Advisor:
Marta Zaniolo

Academic Year 2018 – 2019

Acknowledgments

Abstract

Climate change and growing population are expected to severely affect freshwater availability by the end of 21th century. Many river basins, especially in developing countries, are likely to become more prone to periods of reduced water supply, risking considerable impacts on society, environment, and economy. The construction of new dams has the potential to bring significant social and economic benefits, but in the past several negative impacts have been associated with dam construction. The existing literature concerning optimal or strategic dam planning mainly focused on sizing and siting of dams and its associated impacts; these are certainly important, but for many dams the most severe impact are not associated to regime operations, but to the construction and the filling phases. The construction phase often requires the resettlement of local populations and the preparation of the construction site, and the subsequent filling phase can have non-negligible implications downstream the dam. Extreme precaution towards downstream impacts would require transiting very high percentages of inflow resulting in multi-decadic filling time. A more efficient strategy for upstream interests would tend to speed up the impoundment of water to maximize hydropower production, generating minimal or negligible inflows for several years downstream. In this process, the hydroclimatic variability plays a key role: if the filling occurs in an extremely wet period, the downstream impact is very low, instead in a dry period the impacts will be amplified. The state of global teleconnections stongly influences the hydroclimatic variability, thus introducing a long-term source of predictability on hydrological fluctuations that can be exploited to design efficient filling operations. This study investigates different reservoir filling strategies, in particular, assessing the role that medium and long-term forecasts can play to better inform the impounding strategy, eventually modulating it over time to adapt to the hydroclimatic variability. The proposed methodology is demonstrated onto the case study of the Omo-Turkana basin in Ethiopia, where the construction and filling of Gibe III dam raised the strong opposition of the local community and international organizations. The thesis suggests a retrospective analysis

of Gibe III filling to evaluate the impacts of alternative filling strategies, and demonstrate how the availability of long-term forecasts could prove extremely useful. Rainfall and temperature data necessary for this thesis were retrieved from satellite data comparing and correcting three precipitation remote sensing datasets (TRMM, CHIRPS and TAMSAT) and two temperature remote sensing datasets (MERRA-2 and ORH). Then, the selected and corrected precipitation dataset (TAMSAT) and temperature (MERRA-2) data are employed to compute two drought indexes: SPI and SPEI. Thirdly, we detected the relevant teleconnections in the area. For each phase of the considered climate signals, our approach identifies relevant anomalies in Sea Surface Temperature that influence the local hydrologic conditions which are first aggregated via Principal Component Analysis and then used as input in a multi-variate forecast model of season-ahead drought condition in the Omo basin. The filling strategies that were implemented and tested are designed to respect natural seasonal inflow variability while accounting for the forecasted state of water resources, allowing a larger fraction of the inflow to be released when a drought is forecasted. Results show that the correlation between teleconnections and local variables in the area is relevant, and can be exploited to produce reliable and accurate forecasts, e.g., 9 months ahead SPEI predictions demonstrate hindcast accuracy of $R^2 = 0.84$. The proposed filling strategies are compared with the actual strategy employed for the filling of Gibe III and demonstrate a potential to significantly decrease downstrem impacts during filling transient, for instance by maintaining the level of downstream lake Turkana up to one meter higher than historically.

Summary

Si prevede che i cambiamenti climatici e la crescita della popolazione influenzeranno gravemente la disponibilità di acqua entro la fine del 21° secolo. Molti bacini fluviali, soprattutto nei paesi in via di sviluppo, rischiano di diventare più inclini a periodi di riduzione dell'approvvigionamento idrico, andando incontro a notevoli impatti sulla società, sull'ambiente e sull'economia. La costruzione di nuove dighe ha il potenziale per portare significativi benefici sociali ed economici, ma in passato molti impatti negativi sono stati associati alla loro costruzione. La letteratura precedente si occupa principalmente di pianificazione ottimale o strategica della diga focalizzando l'attenzione sul dimensionamento e l'ubicazione con i relativi impatti; questi sono certamente importanti, ma per molte dighe il vero impatto non è dato dalle operazioni di regime, ma dalle fasi di costruzione e di riempimento. La fase di costruzione implica il reinsediamento delle popolazioni locali e la preparazione del sito di costruzione, e la successiva fase di riempimento può avere implicazioni non trascurabili con la riduzione della portata a valle della diga. Una strategia di riempimento attenta agli impatti a valle richiederebbe di far transitare percentuali molto alte di afflusso con tempi di riempimento multi-decennali. Una strategia più efficiente per gli interessi a monte tenderebbe ad accelerare il più possibile il sequestro dell'invaso per massimizzare la produzione di energia idroelettrica, generando afflussi minimi o trascurabili per diversi anni a valle. In questo processo, la variabilità idro-climatica gioca un ruolo chiave: se il riempimento avviene in un periodo estremamente umido, l'impatto a valle è molto basso, invece in un periodo di siccità gli impatti saranno amplificati. Lo stato delle teleconnessioni globali influisce fortemente sulla variabilità idroclimatica, introducendo così una fonte a lungo termine di prevedibilità sulle fluttuazioni idrologiche che possono essere sfruttate per progettare efficienti operazioni di riempimento. Questo studio indaga diverse strategie di riempimento dei serbatoi, in particolare, valutando il ruolo che possono avere le previsioni a medio e lungo termine per meglio informare la strategia di riempimento, eventualmente modulandola nel tempo per adattarsi alla variabilità

idro-climatica. La metodologia proposta è dimostrata sul caso studio del bacino Omo-Turkana in Etiopia, dove la costruzione e il riempimento della diga di Gibe III hanno sollevato la forte opposizione della comunità locale e delle organizzazioni internazionali. La tesi suggerisce un'analisi retrospettiva del riempimento di Gibe III per valutare quale impatto potrebbero avere strategie di riempimento alternative, e dimostra come la disponibilità di previsioni a lungo termine potrebbe rivelarsi estremamente utile. I dati di precipitazione e di temperatura necessari per questa tesi sono stati ottenuti da dati satellitari confrontando e correggendo tre dataset di precipitazione (TRMM, CHIRPS e TAMSAT) e due dataset di temperatura (MERRA-2 e ORH). Dopodichè, i dati di precipitazione (TAMSAT) e di temperatura (MERRA-2) che sono stati selezionati e corretti vengono utilizzati per calcolare due indici di siccità: SPI e SPEI. In terzo luogo, abbiamo rilevato le teleconnessioni pertinenti nell'area. Per ogni fase dei segnali climatici considerati, la nostra procedura identifica le anomalie rilevanti nelle Sea Surface Temperature (SST) che influenzano le condizioni idrologiche locali che vengono prima aggregate tramite un'analisi della componente principale (PC) e poi utilizzate come input in un modello di previsione multi-variata della condizione di siccità della stagione successiva nel bacino dell'Omo. Le strategie di riempimento che sono state implementate e testate hanno l'obiettivo di rispettare la naturale variabilità di afflusso stagionale, tenendo conto dello stato previsto delle risorse idriche, consentendo di rilasciare una frazione maggiore di portata quando si prevede una siccità. I risultati mostrano che la correlazione tra le teleconnessioni e le variabili locali nell'area è rilevante e che si è in grado di sfruttarla per previsioni affidabili, ad esempio, le previsioni di SPEI con 9 mesi di anticipo dimostrano un'accuratezza con $R^2 = 0.84$. Le strategie di riempimento proposte sono confrontate con la strategia effettivamente impiegata per il riempimento di Gibe III e possiamo vedere che le strategie proposte dimostrano un potenziale per ridurre significativamente gli impatti di valle durante l'orizzonte di riempimento, ad esempio mantenendo il livello del lago Turkana a valle fino a un metro più alto di quello storico.

Contents

List of Figures

List of Tables

1 Introduction

1.1 Dam filling

Climate change and growing population are expected to severely affect freshwater availability by the end of 21th century. Many river basins, especially in developing countries, are likely to become more prone to periods of reduced water supply, risking considerable impacts on society, environment, and economy, thus emphasizing the need to rethink the way water resources are managed at the regional and river basin scale. Dams are constructed for many purposes, including flood prevention, irrigation, and hydroelectric power. With the tens of thousands of existing large dams around the world, and the ever-increasing demand for water and power, dams will continue to make a significant impact on modern day life (*McCartney and King*, 2011). Worldwide, many countries rely upon hydropower for a substantial portion of their electricity production. In developing countries, rapid urbanization and population growth will result into increasing demand for decades to come and electricity remains a key ingredient for improving the lives of millions of people (*Ledec and Quintero*, 2003).

The construction of new dams have the potential to bring significant social and economic benefits, but in the past several negative impacts have been associated with dam construction. These impacts can be contained through a better planning and management of dams (*McCartney and King*, 2011). Dam management in regime conditions is the object of an extensive literature (for reviews see *Labadie* (2004), *Castelletti et al.* (2008)) and planning issues have been more

recently addressed from the point of view of dam optimal sizing, location, and numerosity (*Chang et al.*, 1996; *Becue et al.*, 2002; *Awchi and Abdul-Majeed*, 2004; *Deltares*, 2010; *Castelletti et al.*, 2018). These are certainly important, but for many dams the real impact is not the regime operations, but the construction and the filling phases. These aspects of dam planning are often neglected, despite they can occupy almost 10%, in some cases more, of the expected life of an infrastructure. This elements are crucial especially for large reservoirs, with the pivotal example of the Grand Ethiopian Renaissence dam (GERD), where the filling transient may take from 4 to 20 years, one fifth of the projected dam life (*Zhang et al.*, 2016). In such cases, it is crucial to guarantee an acceptable system performance during the filling period by designing appropriate strategies to reduce downstream impacts. While there have been numerous recent studies debating the long-term economic, sectoral, resource and social implications of the GERD, less attention has been devoted to potential impacts on riparian countries during the reservoir filling stage. Given the massive reservoir volume and large interannual variations in Blue Nile streamflow, the manner in which the reservoir is filled is critical. Ethiopia has an incentive to fill the reservoir rapidly to begin generating hydropower, while downstream countries prefer a modest filling rate to minimize the possible impacts on dependent lives and livelihoods. When river basins are transboundary, moreover, basin-wide conflicts due to impoundment may translate into sovranational conflicts, as in the case of the above mentioned GERD on the Blue Nile (encompassing Ethiopia, Sudan, and Egypt), in Zambesi river basin with Kariba dam conflicts between Zambia, Zimbabwe and Mozambique (**?**) or HoaBinh reservoir in the Red river basin (China, Vietnam, Laos, *Castelletti et al.* (2012)).

Reservoir filling strategies can be designed as a water balance between inflow to the reservoir, based on hydroclimatic conditions, and outflow, based on impoundment/release strategies and evaporation. The rate at which the reservoir is filled has direct implications for hydropower generation, and downstream releases and associated impacts. In non-stationary climates, characterized by the strong presence of climate signals and teleconnections which influence the interannual variability of local hydro-meteorology (*Diro et al.*, 2011; *Degefu et al.*, 2017; *Penso*, 2018), deciding the filling strategies becomes more complex. The same filling rates can have very different results in terms of time employed for filling the dam, and downstream impacts in dry or wet years, and a wise filling strategy should account for it.

A number of studies have investigated the filling policies of GERD dam in Ethiopia evaluating the effect of the dam on Blue Nile riparian countries under hydroclimatic variability and climate change. *King and Block* (2014) and

Liersch et al. (2017) assess the implications of climate variability and emerging climate change within Ethiopia, which cast further uncertainty on potential filling policies and system operations. *Zhang et al.* (2016) introduce simulations of probabilistic streamflow via wavelet analysis in order to define the response of different categories of filling strategy towards wetter or drier conditions. *Wheeler et al.* (2016) analyze implications for downstream water resources using a river basin planning model with a wide range of historical hydrological conditions and increasing coordination between the co-riparian countries.
All these studies have analyzed the problem of dam filling from different perspectives, mainly for GERD, where the conflict had global resonance. However, none of these works explicity considered hydro-climatic variability and the possibility of reducing its uncertainty through forecasts during the dam filling operations. The peculiarity of this work with respect to the previous body of work on GERD, is that we explicitly consider the non-stationarity characterizing the Ethiopian climate and design filling strategies based on season-ahead predicted state of water resources using seasonal forecasts designed accounting for the state of climate signals. The procedure is applied to a large reservoir in southern Ethiopia, namely, the Gibe III dam on Omo river terminating in Kenyan lake Turkana.
The filling operations of Gibe III dam started in January 2015 impounding in the reservoir the equivalent of an average year of streamflow of the Omo river, in the span of around 2 years, and thus significantly reducing the water provision to downstream stakeholders and altering the natural regime. This endangered the fragile ecosystems and the livelihoods of the tribes, which are closely linked to the river and its annual flood. Filling the Gibe III reservoir caused a significant reduction of inflow to the downstream Lake Turkana and the consequent drop in Turkana level. The annual flooding of the Omo River feeds the rich biodiversity of the region and guarantees the food security of the tribes especially as rainfall is low and erratic and they depend on it to practice flood recession agriculture using the rich silt left along the river banks by the slowly receding waters.
The starting point and the duration of filling process are key factors especially in climate regime which alternates wet season and dry season. The duration and impacts caused by filling operations can be estimated using average conditions, but when the filling process starts may occur seasons that deviate from the average conditions and could produce different impacts compared to those calculated first. Thus, the medium or long term forecasts give information on how the seasons will present, allowing to modulate the filling rate, trying to protect downstream if the expected season is dry, and instead allowing a faster

fill if we expect wet season. To produce these medium and long-term forecasts we can rely on teleconnections. Moreover, in our case study the state of global teleconnections stongly influences the climate in terms of rainfall (*Diro et al.*, 2011; *Degefu et al.*, 2017; *Penso*, 2018) and streamflow (*Degefu and Bewket*, 2017), thus the timeline of filling operations must take into account the seasonality and the period of climate signals, through the use of medium and long-term forecasts based on global teleconnections with 9-12 months lead time.

1.2 Teleconnection detection and precipitation forecast

Teleconnection patterns are defined by NOAA (*NOAA*, 2018) as a recurring and persistent, large-scale pattern of pressure and circulation anomalies which affects large geographical areas. These patterns typically last for several weeks to several months, but their effects can sometimes last for several consecutive years, thus representing an important part of both the interannual and interdecadal variability of the atmospheric circulation (*NOAA*, 2018). All teleconnection patterns are an effect of internal atmospheric dynamics and are a naturally occurring result of the interaction of the atmospheric circulation with the land and ocean surfaces. In particular, great amount of energy is absorbed or dispersed when a region's Sea Surface Temperature (SST) changes, and even slow or contained variations may have great effects on some climate patterns and consequently on the climate variability.
The El Niño Southern Oscillation (ENSO), the North Atlantic Oscillation (NAO), the Pacific Decadal Oscillation (PDO), the Atlantic Multidecal Oscillation (AMO), and the Indian Ocean Dipole (IOD) are the main teleconnection patterns in the globe (*Araghinejad and Meidani*, 2013). They were demonstrated to have a relevant impact large-scale changes in the atmospheric wave and jet stream patterns, as well as influence temperature, rainfall, storm tracks, and jet stream location/intensity over vast areas. Thus, they are often the culprit responsible for abnormal weather patterns occurring simultaneously over seemingly vast distances.
Multiple studies in the last decades have recognized the connection between large-scale climate phenomena and hydroclimatology worldwide (*Ward et al.*, 2014; *Poveda and Mesa*, 1997; *Lavers et al.*, 2013; *Grantz et al.*, 2005) and this information has been exploited to improve the forecasts. Accounting for the correlation between rainfall and streamflow anomalies, and changes in large-scale ocean atmospheric patterns, led to improvements in long-lead forecast through the development of statistical approaches that relate 'at site' hydrology to large-

scale ocean-atmosphere state variables providing useful seasonal to interannual forecasts (*Araghinejad et al.*, 2006; *Samale et al.*, 2017). For season-ahead statistical prediction models, SST anomalies are documented as the best performing large-scale precipitation predictor field, based on the theory that the lower atmosphere is forced by large-scale anomalous surface processes (*Zimmerman et al.*, 2016).

Forecasts, coupled with flexible operating rules, may lead to optimal or more efficient reservoir management of storage and release volumes based on expected probabilistic future conditions (*Block*, 2011). In the past, medium and long-term forecasts were generally inaccurate and of scarse interest, but recently seasonal climate forecasting capabilities have significantly advanced, both for physically-based global climate models, and for data driven models, thanks to a better physical understanding of the climate system, that allow to reliably expand the forecast lead time, i.e., the length of time between the issuance of a forecast and the occurrence of the phenomena that were predicted.

Many studies considered the Ethiopian region where our study is focused, demonstrating the influence that the SST in the equatorial Pacific, the northwest Pacific and the Gulf of Guinea all exert on the main rainy season in various parts of Ethiopia. In the case of the equatorial Pacific, a warm anomaly reduces rainfall in northeast and western part of Ethiopia, while a cold anomaly has the opposite effect (*Diro et al.*, 2011). Summer rainfall over central and western Ethiopia is negatively associated with SSTs over the equatorial east Pacific and Indian Ocean (*Diro et al.*, 2011). New regional insight is found regarding East Africa, in particular that October-November rainfall over southern Ethiopia is positively associated with equatorial east Pacific SSTs and with the Indian Ocean Dipole (IOD) (*Degefu and Bewket*, 2017).

Block and Rajagopalan (2007) proposed a framework for ensemble forecast of Kiremt season (June-September) precipitation for the upper Blue Nile basin within Ethiopia. A nonparametric approach based on local polynomial regression is adapted for generating ensemble forecasts that demonstrate significant overall skill, and very high skills during extreme wet and dry years compared to climatological forecast utilized by the Ethiopian National Meteorological Services Agency. In the same river basin, a dynamically linked system was developed, including forecast, rainfall-runoff, and hydropower models, in order to compare benefits and reliability generated by forecasts ensembles against a climatology-based approach, commonly practiced in most water resources systems (*Block*, 2011).

Block and Goddard (2011) evaluates different precipitation prediction techniques from statistical and dynamical models, and their combination, to potentially

augment prediction skill over the Blue Nile basin in Ethiopia. This work considers to what degree greater skill or reliability in a particular prediction technique translates through hydropower management models given their nonlinear response. The climate forecast-hydropower system is sufficiently flexible to allow water managers to attain an optimal balance between benefits and the dependability of energy delivery, by varying exceedance probability and target energy thresholds, with the added benefit of forecast guidance.
Wolde-Georgis (1997) utilizes ENSO information to improve drought early warning and to mitigate the adverse impacts of droughts through forecasts that can provide an early warning with many months of lead time.

1.3 Objective of the thesis

The objective of this thesis is to produce reliable long-term drought forecasts, based on the state of global teleconnections and demonstrate their operational potential in informing the filling of subtropical reservoirs. The Gibe III dam in the Omo-Turkana river basin is used as study.
First of all, we compare and select different satellite data to identify the most suitable for the study area in terms of precipitation and temperature, then we correct them with bias tecniques utilizing in-situ observations. Secondly, these meteorological data are used to compute traditional drought indexes at multiple spatial and temporal aggregations. From our analysis, Standardized Precipitation and Evaporation Index (SPEI) is identified as a key index to detect and characterize droughts in the basin.
Thirdly, we apply the Nino Index Phase Analysis, which employs a data mining techique to capture the state of multiple climatic signals (i.e., teleconnections) from detected relevant anomalies in Sea Surface Temperature on a seasonal time scale. The state of teleconnections is then used as input to a non-linear model calibrated to forecast one season ahead SPEI index, proxy for the basin drought conditions.
Finally, we exploit the drought index forecasts to implement several reservoir filling strategies that take into account the state of water resources during the reservoir filling years. Such strategies demonstrate the ability to reduce the impacts of reservoir filling for the environment and economic activities downstream the dam.

1.4 Thesis outline

The thesis is structured as follows.
Chapter 2 describes the Omo-Turkana basin case study, including its geomorphological features, climate and hydrological regime, main stakeholders involved, and the data and model used for the numerical analysis of this thesis.
Chapter 3 provides the description of the Methods and Tools employed in this study. First, we describe the methodology to compare and correct satellite data in order to find the most suitable product for the area of interest. Then, we present the computational procedure of two widely used drought indexes used to characterize the state of water resources in a basin (SPI and SPEI). After that, we present the NIPA procedure designed to detect the effects of different climate teleconnections on the local scale and we describe a non-linear forecast model used to predict the local hydroclimatic variable of interest based on the state of climate signal. Finally, we describe a methodology for the implementation of different reservoir filling strategies using teleconnection-based seasonal forecasts.
Chapter 4 contains the results of this thesis. The first section is devoted to the comparison and correction of satellite derived climate data in terms of their coherence with the available ground observations. The second section illustrates the results of the computation of two traditional drought indexes, SPI and SPEI, respectively based on precipitation only, and precipitation and temperature. SPEI index is finally deemed more suitable to characterize drought in the basin given the relevance of the temperature in local hydrological processes. The following section applies the NIPA procedure for the detection of relevant climate signals to forecast SPEI index through a non-linear model. Finally, the last part reports the result of an application of the produced long term drought forecat to significantly improve Gibe III reservoir filling strategies.
Chapter 5 sums up the conclusions from this study and suggests further research about the topic.

2

Study site

2.1 Omo-Turkana basin

The Omo-Turkana basin is almost 190,000 km^2 and includes Omo river basin (60,000 km^2) and lake Turkana basin (130,000 km^2) (Fig 2.1).
The Omo river is one of the main Ethiopian rivers, it originates in the rainy mountainous area of the Shewan highlands, and flows southwards into lake Turkana, constituting around 90% of the lake incoming water. In its 760 km course, the river rapidly streams through a steep inaccessible area, before slowing its pace as it nears the lowlands of the lower Omo valley. Its most important tributary is the Gibe river, smaller tributaries include the Wabi, Denchya, Gojeb, Mui, and Usno rivers (*Avery*, 2013).

Lake Turkana is situated in a closed basin within the East African Rift Valley which extends over Ethiopia in the north, Kenya in the south, and Sudan and Uganda in the west. Lake Turkana is Kenya's largest lake, Africa's fourth largest lake, and the world's largest desert lake (*Avery*, 2012). The lake was formely named lake Rudolf in 1888, after the Crown Prince of Austria, and nowadays it is also known as the *Jade Sea* for its remarcable color caused by algae.
Lake Turkana has a maximum depth of nearly 110 m and an average depth of 30 m, and extends up to 250 km long and $15-30$ km wide, with an average surface area of nearly 6750 km^2 (*Velpuri and Senay*, 2012). Turkana is an endorheic lake with no river outflows and the lake losses occur through evaporation, while the inflow is primarily provided by the Omo river and southern

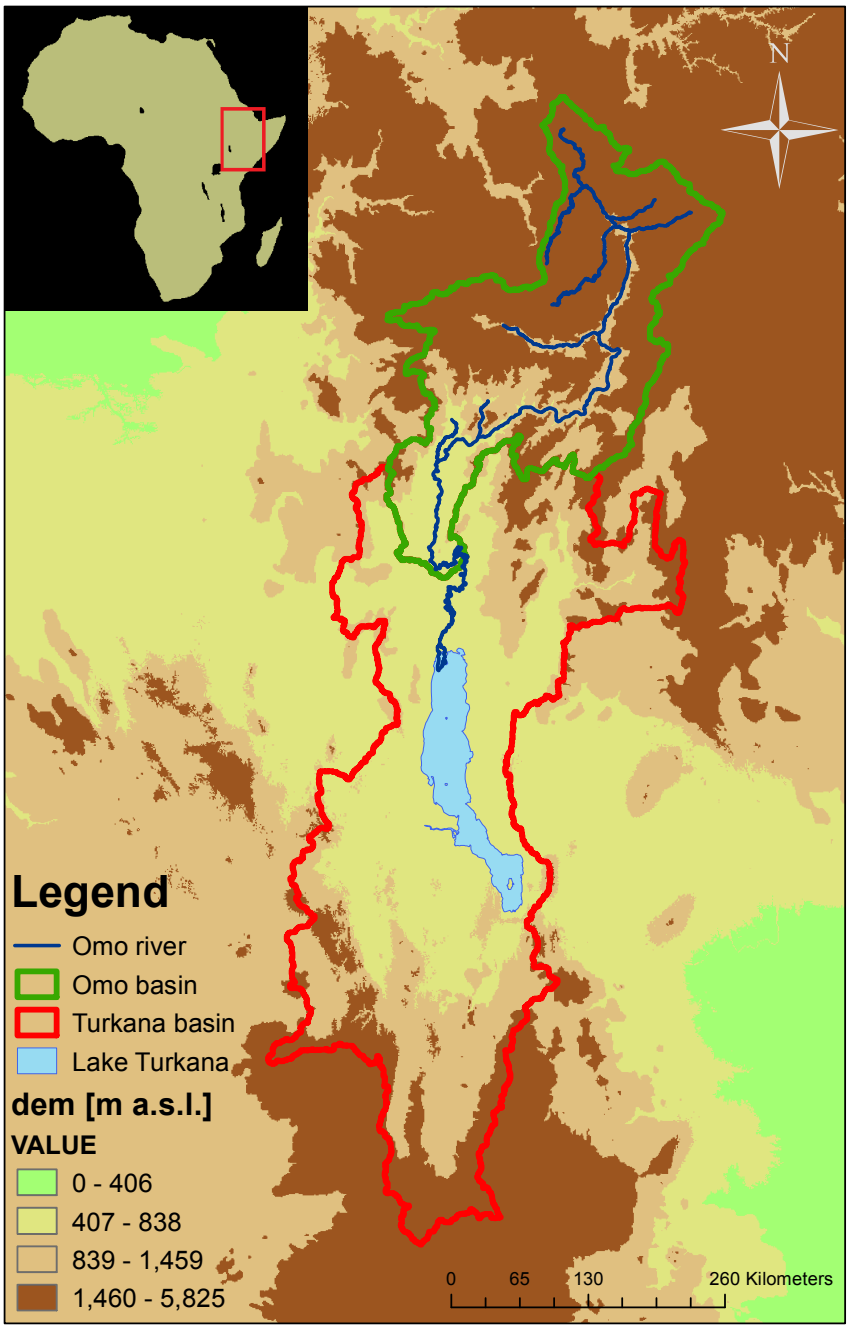

Figure 2.1: Omo-Turkana basin.

tributaries, Kerio and Turkwel.
Recently, a massive hydroelectric power production project has been implemented with the costruction of several dams along the Omo river and an irrigation development of sugarcane plantations. With a total fall of about 1800 m (from an elevation of 2300 m at its source to 500 m at lake Turkana inlet), the river is particularly suitable for hydroelectric generation. To exploit its river hydropower potential, the Ethiopian Electic Power Corporation (EEPCo) has interrupted the natural course of the river and its affluent with a series of dam, namely the Gibe cascade. The Gibe cascade includes the existing Gibe I dam (184 MW, on the Gilgel Gibe river) and Gibe II power station (420 MW) as well as the newly concluded Gibe III (1870 MW). In addition, in 2016 the construction of Koysha dam started. While Gibe I and II are conjunctively operated for hydropower production only, Gibe III and Koysha dams are expected to also provide water to irrigate the extensive sugar plantations in the lower Omo valley (*Avery*, 2012). This man-made changes might impact the water level of lake Turkana, due to reservoir filling and the abstraction of water from Omo river for irrigation purpose, and alter the hydrological cycle.

2.2 Climate and hydrological regime

Ethiopia's varied topography has created three climatic zones depending on the elevation: a cool zone, which covers the central sections of the western and eastern parts of the Ethiopian Highlands above 2400 metres altitude, a temperate zone, which consists of parts of Ethiopian Highlands ranging in altitude between 1500 metres and 2400 metres, and a hot zone which generally comprises areas below 1500 metres altitude.
The climate of the Omo basin ranges from a tropical sub-humid climate in the northern and middle catchment, which comprises most of the Omo basin, to a hot-arid climate in the southern parts of the basin (which includes the semi-desert of lake Turkana in Kenya).
Within this climate zones, three seasons can be identified, characterized by different patterns of precipitations and atmospheric pressure as follows (*Avery*, 2012):

- The *Keremt season*: the main rainy season, usually lasting from June to September
- The *Belg season*: the light rains season, usually from March to May
- The *Bega season*: the dry season, that last from October to February

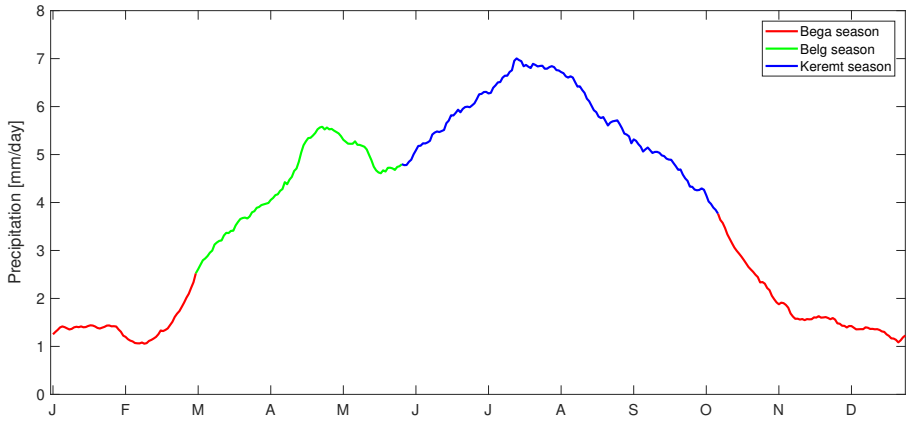

Figure 2.2: Omo basin rainfall from ground stations dataset obtained through a moving average between 1998 and 2008 precipitation with a 30 days window span.

This rainy seasons are recognizable in Figure 2.2, which depicts the average cumulated precipitation of the Omo basin for the years between 1998 and 2008 with the characteristic three seasons described above. Figure 2.3 shows how the rainfall pattern substantially varies within the watershed. In the northern part of the basin, where the Wolkite station is located, precipitation shows a marked unimodal distribution with a pronounced peak in August and a long dry season from November to March. In the central part (Bonga station), a trapezoidal distribution can be observed with a quite constant rainfall from May to September and a less pronounced dry season from December to February. In the southern part (Laske station), a marked bimodal pattern is visible with a higher peak in April and a secondary peak in October. The variation of the rainfall pattern in the watershed contributes to the natural regulation of the lower Omo River flows (*SOGREAH*, 2010). This peculiar precipitation pattern determines the streamflow of the Omo river, which shows an unimodal hydrograph at the inlet of lake Turkana, with a peak flow in August and a baseline flow from December to April (Figure 2.4). This figure refers to the natural flow because it is a monthly mean from 1956 and 1994, when the dams had not yet been built. Lake Turkana level is influenced by different factors, such as the intra-annual oscillation due to Omo river discharge fluctuations. On the longer term, significant drops in the lake level are witnessed in correspondence to severe drought events and dam impounding along the Omo river which temporarily substracts great amount of water volume. It is also well known that Lake Turkana displays long term oscillations due to the influence of several teleconnection pattern in the area. Figure 2.5 illustrates the trajectory of Lake

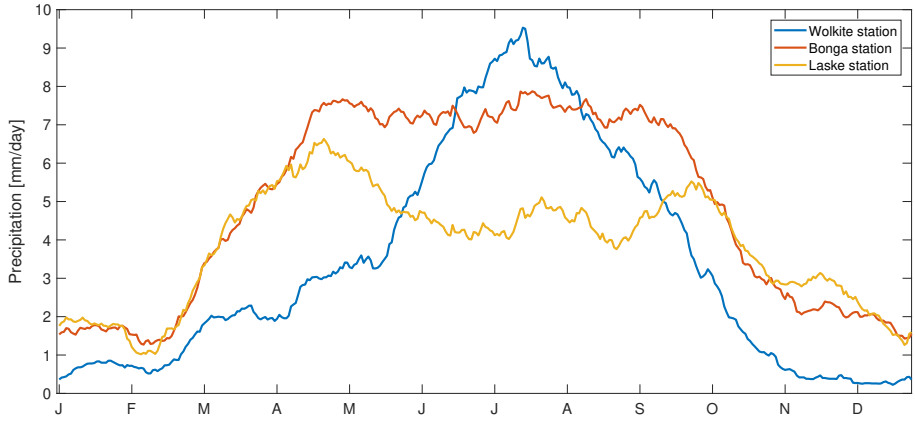

Figure 2.3: Typical rainfall pattern of three Omo basin zones. Wolkite in the north, Bonga in the middle and Laske in the south part of the basin.

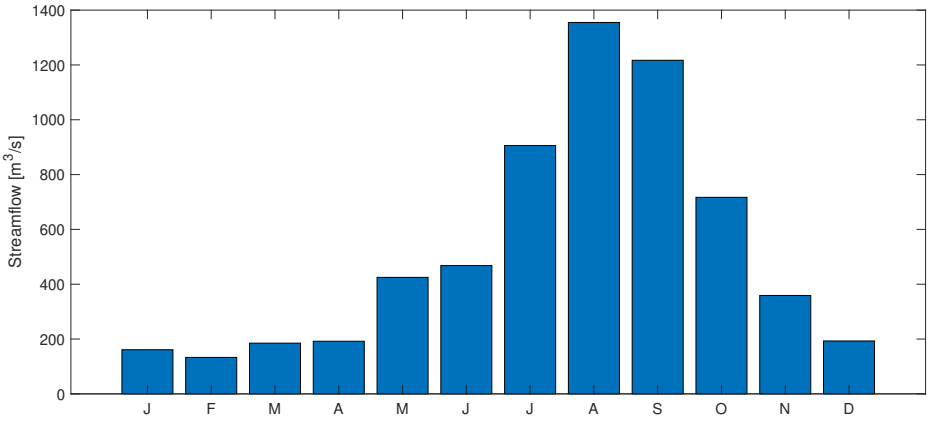

Figure 2.4: Monthly mean Omo river flow at Omorate from 1956 to 1994 (*Avery* (2012)).

Turkana level from 1999 to 2017 with an initial period of strong loss of water level with a minimum peak in 2005 and a later fluctuating pattern until 2015, when the flow rate peaks following a decreasing period due to drought events and Gibe III filling (*Belete et al.*, 2015; *Bloszies and Forman*, 2015).

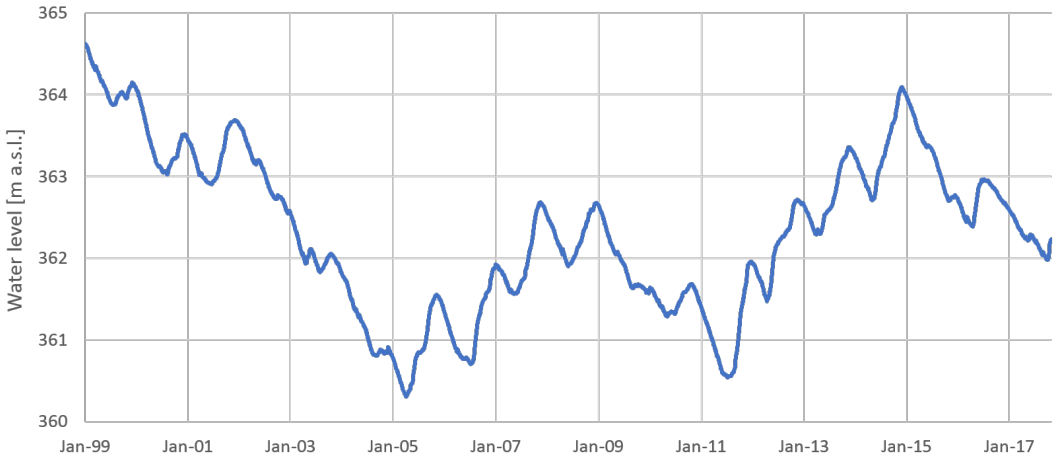

Figure 2.5: Lake Turkana level from 1999 to 2017.

2.3 Main stakeholders

The Omo river is particularly suitable for hydroelectric generation, due to the difference of elevation between the northern part and the southern part, and this indeed motivated government to regulate the natural course of the river through a series of dams. The filling operations of Gibe III dam started in January 2015 and lasted almost two years (*Avery*, 2012) impounding in the reservoir the equivalent of an average year of streamflow of the Omo river, and thus significantly reducing water provision to downstream stakeholders. The stakeholders that we identified to be possibly impacted by dam filling operations are the following:

- **Hydropower**
- **Environment**
- **Recession agriculture**
- **Lake Turkana fisheries**
- **Environment of Lake Turkana**

In the following subsections, each stakeholder will be further described.

2.3.1 Hydropower

Ethiopia is one of the fastest growing economies in the world and to manage this rapid development the government redacted a *Growth and Transformation Plan* (*Commission*, 2015) that adresses the fast growing demand for energy and a strategy to minimize the deficit between supply and demand, eventually even allowing electricity export.
Ethiopia is considered to be a country with one of the highest hydropower potentials in Africa (*SOGREAH*, 2010). For this reason, the government decided to allocate enormous investments into infrastructures of hydropower sector, which led to the construction to the Grand Ethiopian Renaissence Dam (6000 MW) and Gilgel-Gibe III (1870 MW), that together will increase the electricity generation capacity in the country of 234 % (*Boulos*, 2017). Construction of a cascade of hydropower schemes (Fig. 2.6) commenced on the Omo River with the Gibe I (184 MW) commissioned in 2004, the Gibe II hydropower project (420 MW) followed and was commissioned in 2010, with Gibe III's construction (1870 MW) having commenced in 2006 (*Avery*, 2012); the government plans to continue the Gilgel-Gibe hydro dam cascade with the addition of the Koysha dam (2160 MW).

2.3.2 Environment

The overall Omo valley is strictly connected with river regime and suscetible to a river flow change. The lower Omo floodplain crosses a semi-arid to arid savannah and its nutrient rich floods provide a rich annual resource for wildlife, fish and people over a vast and variable area.
Seasonality of the lake and access to fishing localities shifting with seasons is a key component of indigenous communities settled along lake Turkana. The annual flood pulse from the Omo river, combined with the prevailing winds and currents in the lake, combine to establish peculiar seasonal differences. The lake is exposed to strong winds during certain months, with the prevailing winds from the southeast being a critical factor in the mixing of lake waters and nutrients (*Carr*, 2017).

2.3.3 Recession agriculture

Recession agriculture is a fundamental component of livelihoods in the lower Omo Basin. In most years, during August and September the lower Omo valley experiences seasonal river flooding, caused by heavy rains falling upstream between April and August. The river overflows its banks and floods the land

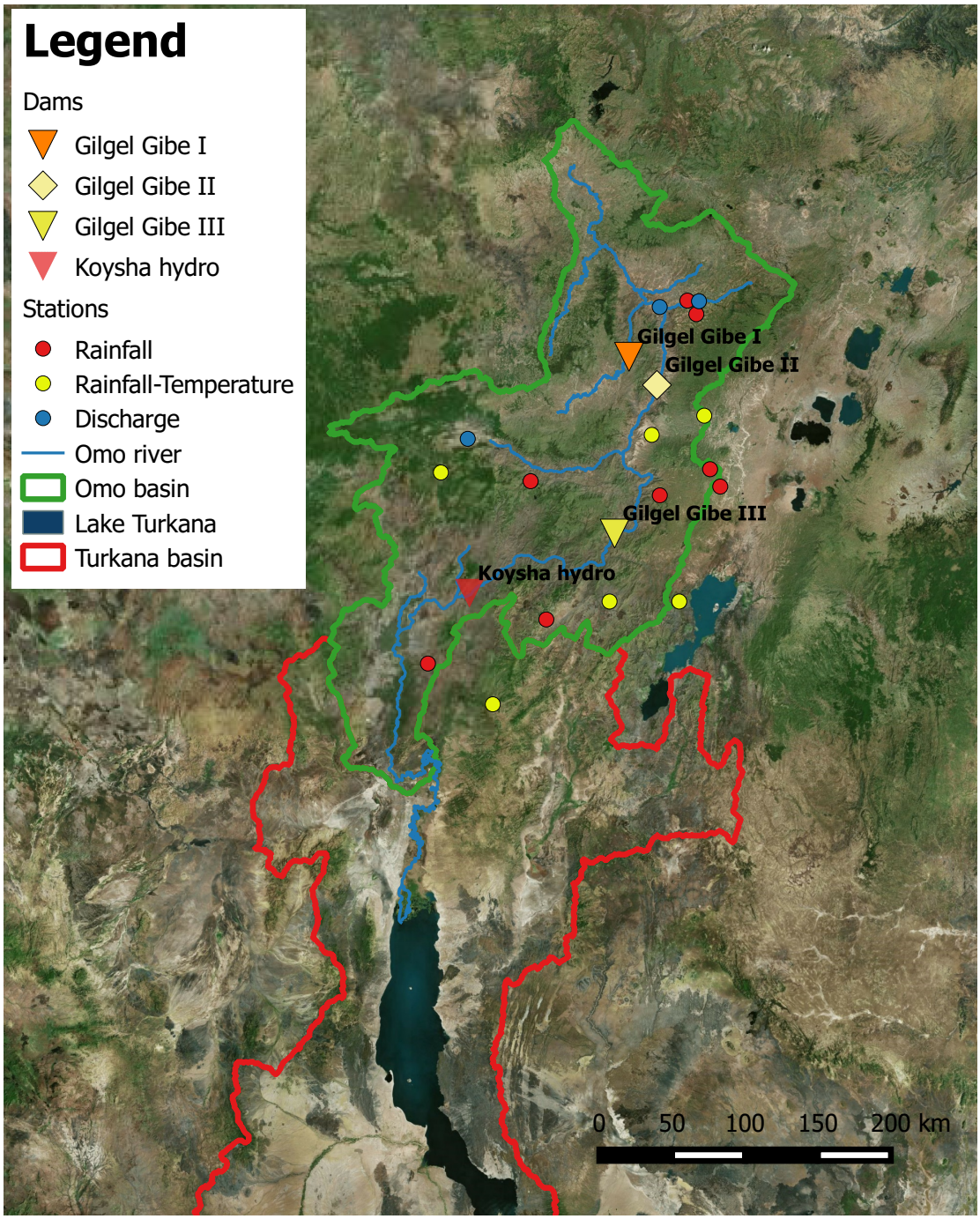

Figure 2.6: Hydropower cascade along Omo river and ground stations available in the region.

along its borders creating the perfect terrain to cultivate when the water recedes 2-3 weeks later to allow planting from September to October. Heavy flooding also renews oxbow lakes, such as lake Dipa, giving access to large areas of well-inundated land for cultivation.
The numerous Omo valley tribes practice a sophisticated system of recession agriculture and seasonal grazing, systems that enable significant populations to secure subsistence with marginal environmental impacts on other species and ecosystem services.
The majority of the lower Omo population is dependent upon access to local natural resources and particularly highly dependent on the Omo river flood cycle (*SOGREAH*, 2010).

2.3.4 Lake Turkana fisheries

The Turkana's aquatic ecology has evolved directly from its former Nile fluvial connection, and is affected by the presence of an high saline level that make it the most saline lake in East Africa containing freshwater fauna. Salinity is already at a critical level for various species and at the extinction level for mollusks.
The productivity of lake Turkana's fisheries is profoundly linked to volume and annual patterns of water inflow from the Omo river. These linkages are driven by the influence of hydrology on fish habitat and food availability, breeding cues, and catchability (*Gownaris et al.*, 2017). The upstream flooding dilutes the lake water and lower the salinity levels in the northern parts, in particular nitrogen, one of the most important factors limiting the fisheries production, is also transported into the lake through Omo waters.
Instead, a water level decline will initially lead to an increase in the availability of litoral habitats, productivity will be degraded due to the loss of seasonal inundation cycles. Water level decline will also lead to a reduction in open water habitat and productivity, as the river is the major source of nutrients to the nitrogen-limited lake (*Gownaris et al.*, 2017).

2.3.5 Environment of Lake Turkana

Since the Omo supplies 90 per cent of the water entering Kenya's Lake Turkana, the regulation of the Omo flows will alter the hydrological inflow patterns to Lake Turkana. This will directly impact the ecology of the lake, which is the Kenya's largest lake, and the world's largest desert lake. The alteration of the downstream hydrological regime is a well established cause of ecological degradation and to evaluate the alteration inducted to lake Turkana we used

indicators of hydrologic alteration.
The general approach for the definition of hydrologic alteration indexes is first to define a series of biologically relevant hydrologic attributes that characterize intra-annual variation in water conditions and then to use an analysis of the inter-annual variation in these attributes as the foundation for comparing the hydrological regimes before versus after a system has been altered by various human activities (*Richter et al.*, 1996; *Bizzi et al.*, 2012).
Salinity is an important element for the system ecology. For its calculation equation 2.12 has been used, which was also stated in *Avery* (2012). Any dramatic reduction in river inflow will lead to a reduction in lake volume and increase in salt concentration.

2.4 Model

The conceptual model of Omo-Turkana system includes the hydropower cascade along Omo river with Gibe I, II and III dams and terminates in the lake Turkana. The water transport across river reaches is computed with a plug-flow model, while mass balance equations (eq. 2.1) are computed for the entire reservoir with a daily time-step. Streamflow data available are obtained by ETH university through Topkapi model, a fully-distributed physically-based hydrologic model. This model describes only the reservoir filling phase and not considered the regime operations.

$$s_{t+1} = s_t + n_{t+1} - r_{t+1} \tag{2.1}$$

where s_t is the storage of the lake at time t, n_{t+1} is the net inflow to the reservoir that enters the lake in the interval $[t, t+1)$, i.e., the difference between inflows, evaporation and other losses, and r_{t+1} is the release from the reservoir in the interval $[t, t+1)$. In our simulations, we will adopted the historical release for Gibe I, and try different release policies for Gibe III is calculated as:

$$r_{t+1} = f(s_t, u_t) \tag{2.2}$$

where the function f describes the non-linear relationship between the decision u_t and the release r_{t+1} given the constraints on maximum and minimum feasible release, and u_t is a feedback operating rule.

$$u_t = f(n_t, I_t) \tag{2.3}$$

The release decision is a function of the inflowing water n_t and additional in-

formation I_t depending on the predicted state of water resources in the region. The output of the model are the hydrological trajectories (storage, release, water level) for lake Turkana and each reservoir implemented, the performance of the system under the defined Gibe III filling strategy with respect to the following objectives:

- **Hydropower**, maximize hydroelectric production

$$J_{tot}^{hyd} = J_{G_I}^{hyd} + J_{G_{II}}^{hyd} + J_{G_{III}}^{hyd} \tag{2.4}$$

  where

$$J_{G_i}^{hyd} = \frac{1}{H} \times \sum_{i=1}^{H} q_{t+1}^{G_i} h_t^{G_i} \psi \tag{2.5}$$

  where $q_{t+1}^{G_i}$ is the turbined water by G_i reservoir with i=I,II,III; $h_t^{G_i}$ is the reservoir water level and ψ is a coefficent that includes turbine efficiency, water density, gravitational acceleration and dimensional conversion.

- **Environment**, minimize the difference between Turkana inflow and natural flow

$$J^{env} = \frac{1}{H} \times \sum_{i=1}^{H} g_{t+1}^{env} \tag{2.6}$$

  where

$$g_{t+1}^{env} = (q_{t+1}^{delta} - q_t^{nat})^2 \tag{2.7}$$

  where q_{t+1}^{delta} is the inflow at Turkana delta and q_t^{nat} is the natural flow in the Omo river, obtained through model simulation without considering the dam cascade along the river.

- **Recession agriculture**, minimize irrigation deficit in August-September (recession agriculture months)

$$J^{rec} = \frac{1}{H} \times \sum_{i=1}^{H} (g_{t+1}^{rec})^2 \tag{2.8}$$

  where

$$g_{t+1}^{rec} = (q_t^{flood} - q_{t+1}^{rec})^+ \tag{2.9}$$

where q_t^{flood} is a flood pattern which recession agriculture needs and q_{t+1}^{rec} is the flow at recession agriculture zones exploit by tribes.

- **Lake Turkana fisheries**, index that computes fish yield from average lake level and level oscillation between dry season and wet season (*Gownaris et al.*, 2017).

$$J^{fish} = \max_{y=0,\dots,N_y} \mid F^{nat} - F_{y+1} \mid \tag{2.10}$$

where

$$F_y = \alpha \cdot h_{y-1}^T + \beta \cdot ampl_y + \gamma \tag{2.11}$$

where F_y is the fish biomass in year y, h_{y-1}^T is the Turkana average level in the previous year and $ampl_y$ is the current year level oscillation.

- **Environment of Lake Turkana**, the indicators adopted over the horizon considered in this study are: mean flow at Turkana, mean annual flow at Turkana, monthly mean flow at Turkana, annual minimum and maximum flows at Turkana with 1-3-7-30-90 days means, lake Turkana water level and lake salinity:

$$S_{end} = \frac{V_{end}}{V_{ini}} \times S_{ini} \tag{2.12}$$

where S_{end} is the salinity level at the end of the simulation [dS/m] and S_{ini} is the salinity level at the beginning of the simulation [dS/m].

2.5 Data

In poorly gauged river basins characterized by a limited availability of in-situ meteorological stations, the satellite data constitute a valid resource to retrieve hydro-meteorological information. However, the accuracy of the satellite products varies from region to region, and a thorough accuracy assessment of the satellite products to be employed is warranted before delving into subsequent analysis.
To overcome this data challenge *Gebrechorkos et al.* (2018) used a combination of accessible data sources based on station data, earth observation by remote sensing, and regional climate models. He did so by relating point to pixel, point to area grid cell average, and stations average to area grid cell average over 21

regions of East Africa: 17 in Ethiopia, two in Kenya and two in Tanzania. The correlations were analyzed at daily, dekadal (10 days), and monthly resolution for rainfall and maximum and minimum temperature.

2.5.1 Precipitation data

Rainfall can be estimated remotely, either from ground-based weather radars or from satellite. With the advent of geostationary weather satellites in the 1960s and 70's, positioned above the equator at 5-6 positions around the globe to provide complete coverage, various techniques have been developed to estimate rainfall from visible and infrared (IR) radiation. The higher the cloud albedo, the more droplets it contains and the deeper it tends to be, so the more likely rainfall is on the ground.
In the study area are conducted several studies that compare the accuracy of different satellite product in terms of precipitation and employ the most reliable product to calibrate hydrological model and simulate the river inflow from Omo into Lake Turkana (*Velpuri and Senay*, 2012; *Anghileri et al.*, 2017).
In this section we describe the rainfall remote sensing datasets collected and employed in the thesis:

- **TRMM**, the *Tropical Rainfall Measuring Mission* (TRMM) *Multisatellite Precipitation Analysis* (TMPA) provides a calibration-based sequential scheme for combining precipitation estimates from multiple satellites, as well as gauge analyses where feasible, at fine scales ($0.25^\circ \times 0.25^\circ$ and 3 hourly). TMPA is available both after and in real time, based on calibration by the TRMM Combined Instrument and TRMM Microwave Imager precipitation products, respectively (*Huffman et al.*, 2007). Rainfall data from TRMM are available from 1998 to present and can be downloaded from the Goddard Earth Sciences Data and Information Services Center (https://disc.gsfc.nasa.gov/).

- **CHIRPS**, the *Climate Hazards group Infrared Precipitation with Stations* (CHIRPS) dataset builds on previous approaches (CHIRP) to smart interpolation techniques and high resolution, long period of record precipitation estimates based on infrared Cold Cloud Duration (CCD) observations. The algorithm is built around a 0.05° climatology that incorporates satellite information to represent sparsely gauged locations, incorporates 1981-present 0.05° CCD-based precipitation estimates, blends station data to produce a preliminary information product and uses a novel blending procedure incorporating the spatial correlation structure of CCD-estimates to assign

interpolation weights (*Funk et al.*, 2015). The dataset can be downloaded from the Climate Hazard Group (http://chg.geog.ucsb.edu/data/chirps/).

- **TAMSAT**, the *Tropical Applications of Meteorology using SATellite and ground based observations* rainfall dataset is based on high resolution Meteosat thermal-infrared (TIR) observations for all of Africa, available from 1983 to the present using daily calibrated cold cloud duration (CCD) observations. The TAMSAT algorithm is based on two primary data inputs: Meteosat TIR imagery provided by *The European Organisation for the Exploitation of Meteorological Satellites* (EUMETSAT) and rain gauge observations for calibration. The TAMSAT algorithm is an example of a cloud-indexing method: the duration of cloud tops exceeding a predetermined temperature threshold, known as cold cloud duration (CCD), acts as a proxy for rainfall (*Maidment et al.*, 2017). Rainfall data can be downloaded from the TAMSAT website (http://www.tamsat.org.uk).

2.5.2 Temperature data

Satellite temperature measurements are inferences of the temperature of the atmosphere at various altitudes as well as sea and land surface temperatures obtained from radiometric measurements by satellites. Satellites measure radiances in various wavelength bands, which must then be mathematically inverted to obtain indirect inferences of temperature. Satellites may also be used to retrieve surface temperatures in cloud-free conditions, generally via measurement of thermal infrared from radiometer sensors.
In this section we describe the temperature remote sensing datasets collected and employed in the thesis:

- **MERRA-2**, the *Modern-Era Retrospective analysis for Research and Applications, Version 2* (MERRA-2) has many of the same basic features as the MERRA system but includes several updates among which the forecast model, new satellite observation sources and bias correction of aircraft temperature observations (*Gelaro et al.*, 2017). MERRA-2 has a spatial resolution of $0.5^\circ \times 0.625^\circ$ in latitude and longitude and is available from 1980 to present. MERRA-2 products are accessible online through the NASA Goddard Earth Sciences Data Information Services Center (GES DISC, https://disc.gsfc.nasa.gov/).

- **ORH**, is a global and regional (Northern/West/East Africa) three-hourly, daily, and monthly meteorological data set available until 2005 with a resolution of 0.1°. The spatial downscaling of ORH is done with the inclusion

of changes in elevation and it is evaluated against ground stations (global summary of the day) available at the US National Climatic Data Center (NCDC). ORH is corrected for temporal inhomogeneity and biases, random errors are omitted through assimilation with ground observations (*Gebrechorkos et al.*, 2018). This data is freely available from the Terrestrial Hydrology Research Group, University of Princeton (http://hydrology.princeton.edu).

3

Methods and Tools

This chapter provides the methodological context for this thesis research by describing the methods and tools employed. Figure 3.1 presents a flowchart of the overall methodology divided into four main building blocks, which are discussed in the following subchapters.
The first block compares climate ground data with remote sensing data in order to determine which remote sensing product is the most suitable for the analysis of the poorly gauged river basin. Rainfall data from TRMM, CHIRPS and TAMSAT are compared with in-situ precipitation data. Temperature data from MERRA-2 and ORH are compared with temperature ground data.
Then, the results of climate analysis are combined into drought indexes to identify dry periods through two different statistical indicators, SPI and SPEI. In the following step, we firstly apply the El Niño Index Phase Analysis (*Zimmerman et al.*, 2016) to detect the effects of different climate teleconnections on the Omo river basin. Secondly, we construct teleconnection-based seasonal meteorological and drought forecasts by predicting precipitation and SPEI index.
Finally, we demostrate the operational value of the produced long-term forecasts by employing them to implement smarter reservoir filling strategies focusing on minimizing downstream impacts.

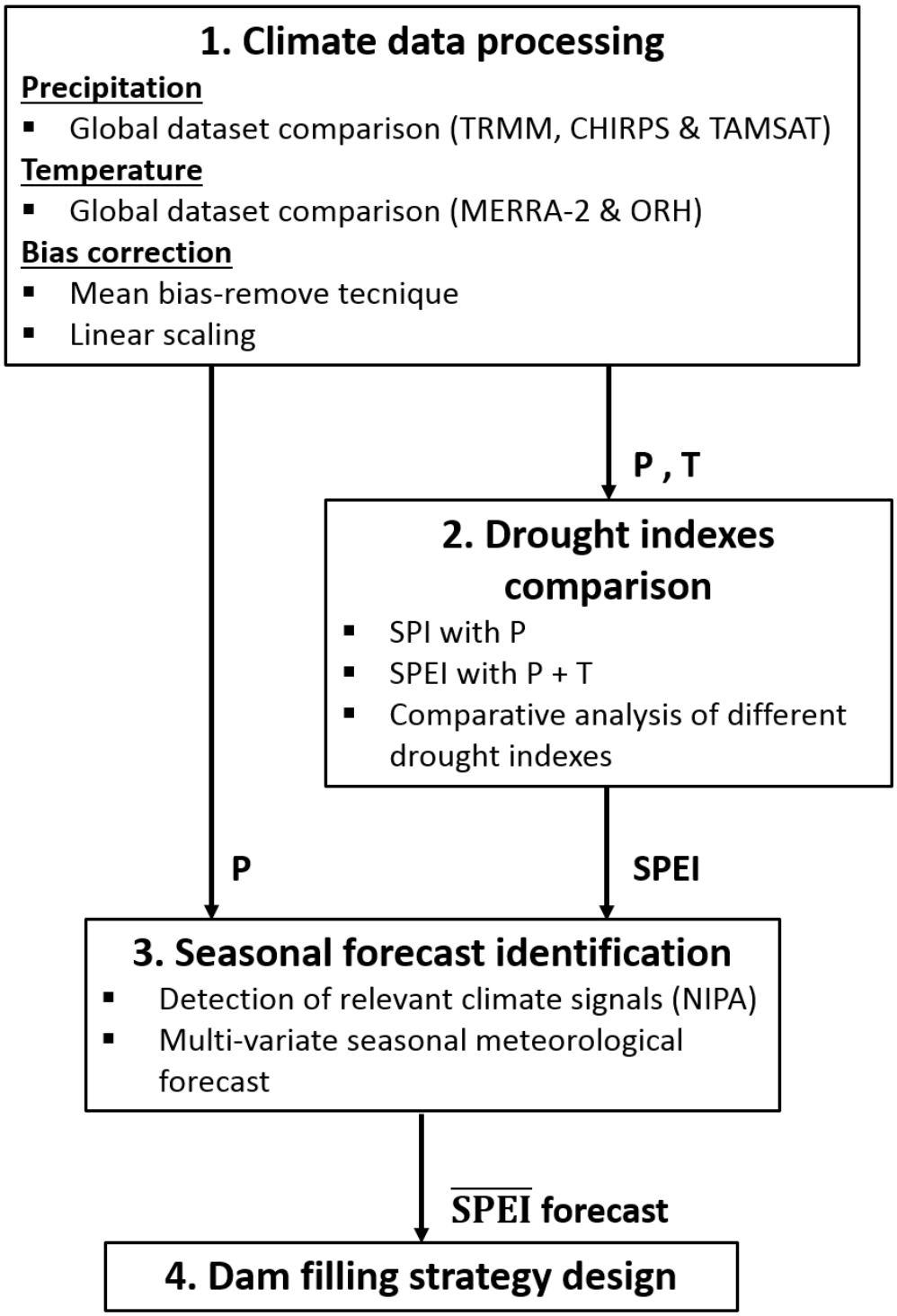

Figure 3.1: Thesis flowchart. The sections number reported refer to the sections in this Chapter that present the framework steps: 1. Climate data processing, 2. Drought indexes comparison, 3. Seasonal forecast identification, 4. Dam filling strategy design

3.1 Climate data processing

3.1.1 Global dataset comparison

This analysis indicates which global satellite-derived dataset of precipitation and temperature is the most accurate for the Omo river basin. As described in section 2.5, this thesis evaluates the performances of three precipitation remote sensing dataset (TRMM, CHIRPS and TAMSAT) and two temperature remote sensing datasets (MERRA-2 and ORH) by comparing the satellite datasets with in-situ measures. Based on the availability of in-situ climate data (Figure 2.6), the comparison of precipitation is done from Januray 1998 to December 2008, whereas the comparison for temperature is done from Januray 1998 to September 2008.
All satellite products were rescaled at the same resolution choosing the finer resolution among the available products to make the results consistent: TRMM and TAMSAT were adapted to CHIRPS resolution ($\Delta = 0.05^\circ \times 0.05^\circ$) and MERRA-2 to ORH resolution ($\Delta = 0.1^\circ \times 0.1^\circ$).
The entire Omo basin is divided into Thiessen polygons where at each cell belonging to the Omo basin the values of the nearest ground station are assigned and the ground data are compared with the data from the corresponding grid cell of satellite dataset. For this comparison, the correlation coefficient (cor) and root mean square error (RMSE) between in-situ data and satellite products are calculated on a daily, decadal, monthly and seasonal timescale (*Gebrechorkos et al.*, 2018).
With this procedure, the different remote sensing products are compared and after that the raw satellite datasets are corrected through ground station informations applying bias correction methods. This analysis indicates which global satellite-derived dataset of precipitation and temperature is the most accurate for the Omo basin.

3.1.2 Bias correction

Global satellite products can be affected by systematic errors (namely, bias) at the local scale that need to be corrected before the rainfall and temperature estimates can be used for any hydrological application. These biases are due to the inaccurate estimation of climate variables, errors transferred from GCMs to RCMs or the incorrect remote detection of rainfall events, and can depend significantly on elevation, latitude and climate (*M'Po et al.*, 2016). In this study, two different correction methods are employed: mean bias−remove technique (*Ajaaj et al.*, 2016) and linear scaling (*Adams*, 2017).

1. *Mean bias-remove technique (MBR)*: the mean bias b_t is calculated each day of the time series for each basin cell by calculating the difference between the ground data cyclostationary mean and satellite data cyclostationary mean.

$$b_t = \overline{G_t} - \overline{S_t} \tag{3.1}$$

$$S_{corr} = S_t + b_t \tag{3.2}$$

   where $\overline{G_t}$ and $\overline{S_t}$ are the ground data cyclostationary mean and satellite data cyclostationary mean, respectively. The cyclostationary mean is smoothed with a 15-days semiwidth window. The mean bias b_t is added to the daily raw satellite data time series to obtain the corrected dataset S_{corr}.

2. *Linear scaling (LS)*: this method aims to match the monthly mean of the precipitation/temperature values to be corrected with the observed means

   - The total monthly precipitation/temperature is cumulated from the observed data and the satellite product per pixel
   - The mean precipitation/temperature is determined for each month in each cell
   - The bias factor is calculated and multiplicated by the satellite value

$$\tau_{mon} = \frac{\overline{G_{mon}}}{\overline{S_{mon}}} \tag{3.3}$$

$$S_{corr} = S_t * \tau_{mon} \tag{3.4}$$

where τ_{mon} is the monthly bias factor, $\overline{G_{mon}}$ is the observed mean monthly precipitation (or temperature) and $\overline{S_{mon}}$ is the satellite mean monthly precipitation (or temperature). The corrected datasets are calculated multiplying the satellite time series by the corresponding monthly bias factor.

3.2 Drought indexes comparison

The second step of the framework in Figure 3.1 employs the corrected precipitation and temperature data obtained from step 1 to compute two widely used statistical drought indicators, namely, the Standardized Precipitation Index (SPI), and the Standardized Precipitation and Evapotranspiration Index (SPEI), (*Zargar et al.*, 2011). Statistical drought indicators rely on the analysis

of time series of the input variables to detect the anomalies that may lead to drought conditions identifying drought periods when the observed values are persistently and significantly below the normal condition.
The SPI indicator receives as input only the precipitation time series, which is then cumulated over a desired time span, fitted to an appropriate probability distribution (generally, the Gamma distribution), and, finally, transformed into a standardized normal distribution (*McKee et al.*, 1993). The indicator values represent the number of standard deviations the observed precipitation deviates from the normalized average: positive values indicate an excess of precipitation with respect to the average, while negative values represent below average conditions (*Zaniolo*, 2017). SPEI index has the same computational procedure of SPI, but corrects the precipitation data subtracting the estimated evaporation, and it has the advantage of combining precipitation and temperature. In hot climates the high temperature results in high evaporation rates which is an important driver in determining a drought (*Vicente-Serrano et al.*, 2010).
According to *Spinoni et al.* (2016), a drought event starts when the indicator value falls below -1 for two consecutive months and ends when it turns positive. This assumption is valid for the two drought indicators considered in this study that are part of the SPI family.
There is no single definition of drought, and meteorological, hydrological, and agricultural droughts are often distinguished (*Palmer*, 1965; *Spinoni et al.*, 2016; *Mishra and Singh*, 2010; *Zaniolo*, 2017; *Hao et al.*, 2018)). Meteorological drought is defined as a lack of precipitation over a region for a period of time. The time scale for meteorological drought is the short-term.
Agricultural drought, usually, refers to a period with declining soil moisture and consequent crop failure. A decline of soil moisture depends on several hydro-meteorological factors, primarily evapotranspiration, and refers to medium term.
Hydrological drought is related to a period with inadequate surface and subsurface water resources for established water uses of a given water resources management system. The key variable is therefore the streamflow, employed to describe the abundance of water in the water cycle. This drought concerns the long term and takes place after a prolonged time of low precipitation and deficient soil moisture. The reduction in the streamflow, and the consequent low input to water bodies, affects the wellness of wetlands and wildlife making this drought the most dangerous and difficult to deal with.

3.3 Seasonal forecast identification

The third step of the framework (see Figure 3.1) analyses the influence of climate teleconnections on the study area using the Niño Index Phase Analysis (NIPA) through the different climate indices as a physical influence of the average state of the atmosphere-ocean system (*Zimmerman et al.*, 2016). Relevant detected teleconnections are then used to construct a data-driven multivariate seasonal forecast.

3.3.1 Detection of relevant climate signals (NIPA)

A preliminary analysis is performed in order to select the hydrometeorological variable or index of interest for the seasonal forecast, and, at the same time, at the global scale defining the main climate signals that influenced the study region on the basis of previous analysis and geographical location.
The large-scale climate signals identified as relevant on the global scale are North Atlantic Oscillation (NAO, *Hurrell et al.*, 2003), El Niño Southern Oscillation (ENSO, *Hanley et al.*, 2003), Pacific Decadal Oscillation (PDO, *Mantua and Hare*, 2002), Indian Ocean Dipole (IOD, *Saji and Yamagata*, 2003) and Atlantic Multidecadal Oscillation (AMO, *Enfield et al.*, 2001), as measured by Hurrel NAO Index, MEI Index, Mantua PDO Index, DMI and AMO index, respectively.
The Niño Index Phase Analysis is a statistical framework for seasonal forecast developed by *Zimmerman et al.* (2016), the main steps are the following (Figure 3.2):

1. *Phases identification*: use of the climate signal index for binning years into positive and negative phases;
2. *SST predictor fields selection*: SST predictor regions are identified via correlation analysis;
3. *Principal Component Analysis (PCA)*: the analysis is performed in order to select the predictors for a linear regression model;
4. *Cross-validated predictions*: a cross-validated model hindcast is conducted for evaluating model performance;
5. *Validation via Monte Carlo analysis*: test the significance of the results via Monte Carlo simulation.

In the first step, the climate index is used for binning the years in different phases, the occurrance of large-scale climate events is connected with hydro-

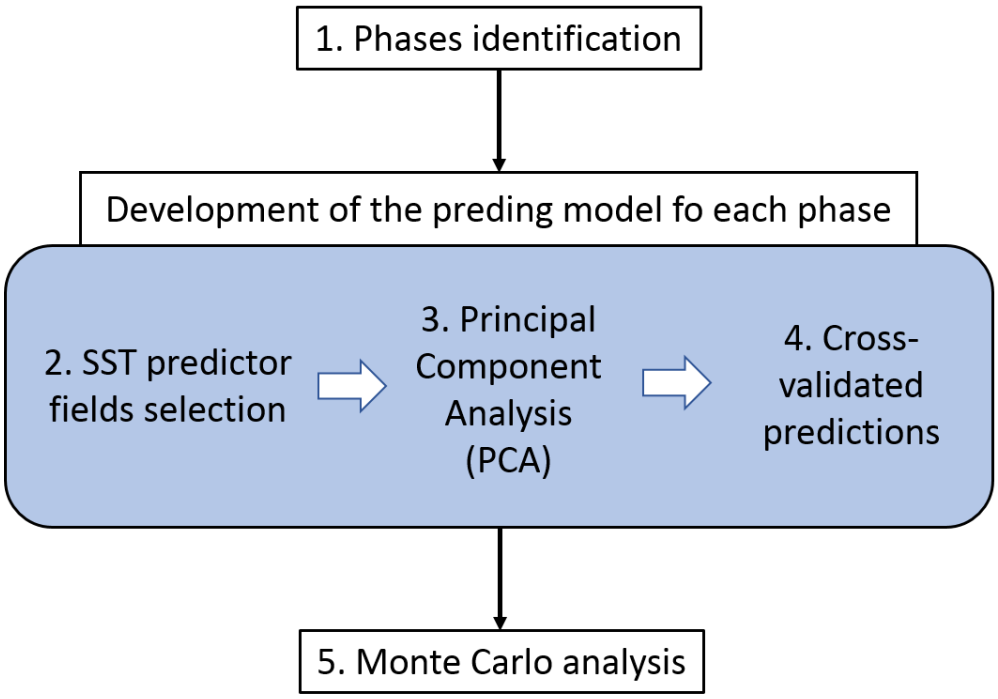

Figure 3.2: Schematic representation of the NIPA procedure.

climatic anomalies that alter the mean state of the atmospheric-oceanic system. These variations can be detected by means of suitable indexes that capture the features of the seasons under study to classify them into climatic phases. The classification is done by fixing a percentile thresholds defined according to the number of phases the years are divided in. For example the 50^{th} percentile is set as threshold to bin the years into two different phases (positive and negative).

For each phase, NIPA identifies Sea Surface Temperature (SST) regions which correlate at 95 % significance level with the lagged local hydroclimatic variable. The SST cells identified as relevant are spatially aggregated with a Principal Component Analysis (PCA) and the first m resulting Principal Components (PCs) are retained as predictors in a forecast model.

In this work, we considered only the first Principal Component, i.e. $m = 1$, for each phase (PC_1):

$$\hat{y}_1 = \beta * PC_1 + \alpha \tag{3.5}$$

Equation 3.5 describes a linear forecast model where $\hat{y}_1$ is the estimated hydroclimatic variable, β are the regression coefficients and α the intercept.

A cross-validation procedure is applied to the models obtained through the

PCA, in order to compare different climate signal while avoiding artificial predictability, for example the bias associated to hindcast skill estimates in statistical forecasting models (*Samale et al.*, 2017). In particular, a leave-one-out cross-validation is employed to avoid model overfitting and improving the statistical significance of the results. This procedure is repeated as many times as the number of data that are in the dataset changing every round the deleted observation for the validation. The predicted values and the observations are contrasted by using as evaluation metric the standard Pearson correlation coefficient r:

$$r = \frac{\sum_{i=1}((x_i - E[x_i])(y_i - E[y_i])}{\sqrt{\sum_{i=1}(x_i - E[x_i])^2(y_i - E[y_i])^2}} \tag{3.6}$$

Lastly, a Monte Carlo test is performed to verify that the obtained results are statistically significant at a high level of confidence.
This analysis is useful for our purpose to select the climate signals that demonstrate higher accuracy and level of confidence and only the selected climate teleconnections are used in the following step to build a seasonal meteorological forecast model.

3.3.2 Multi-variate seasonal meteorological forecast

The second step in the third block of the flowchart (Figure 3.1) combines the results obtained in NIPA procedure into a non-linear forecast model. Thus, NIPA detects the most relevant climate signals to predict the local variable of interest, in terms of accuracy and confidence, as well as the relative PCs of SST predictors for each phase of the signal. In this block, the defined PCs are used as input in a non-linear forecast model. For instance, we will assume that the NIPA procedure detects as relevent two indices, namely A and B. The meta-phases associated to A and B are obtained by combining the original two phases identified for the two indexes when considered independently. The result is therefore a partition in 4 meta-phases: positive A-positive B, positive A-negative B, negative A-positive B, and negative A-negative B. An example of meta-phase creation can be seen in Table 3.1 In this study we used Extreme Learning Machine (ELM, *Huang et al.*, 2006) as model class, highy non-linear model in the family of neural networks that was proven effective for this application from a previous benchmark study (*Gentile*, 2018). ELM models are a learning algorithm which randomly choose hidden nodes and analytically determines the output weights (Figure 3.3) and are demonstrated to produce good generalization performance in most cases while learning thousands of times faster than

Table 3.1: Metaphases vector building.

Index A	Index B	Meta phase (Mph)
1	1	1
1	2	2
2	1	3
2	2	4

conventional feedforward neural networks (*Huang et al.*, 2006). The ELMs are formulated as follows:

$$Y = ELM(PC_i, PC_j, Mph) \tag{3.7}$$

where Y is the predicted variable, PC_i and PC_j are the Principal Components with $i, j = (NAO, MEI, PDO, IOD, AMO)$, and Mph indicates the metaphase of the considered season, as reported in Table 3.1. To estimate the parame-

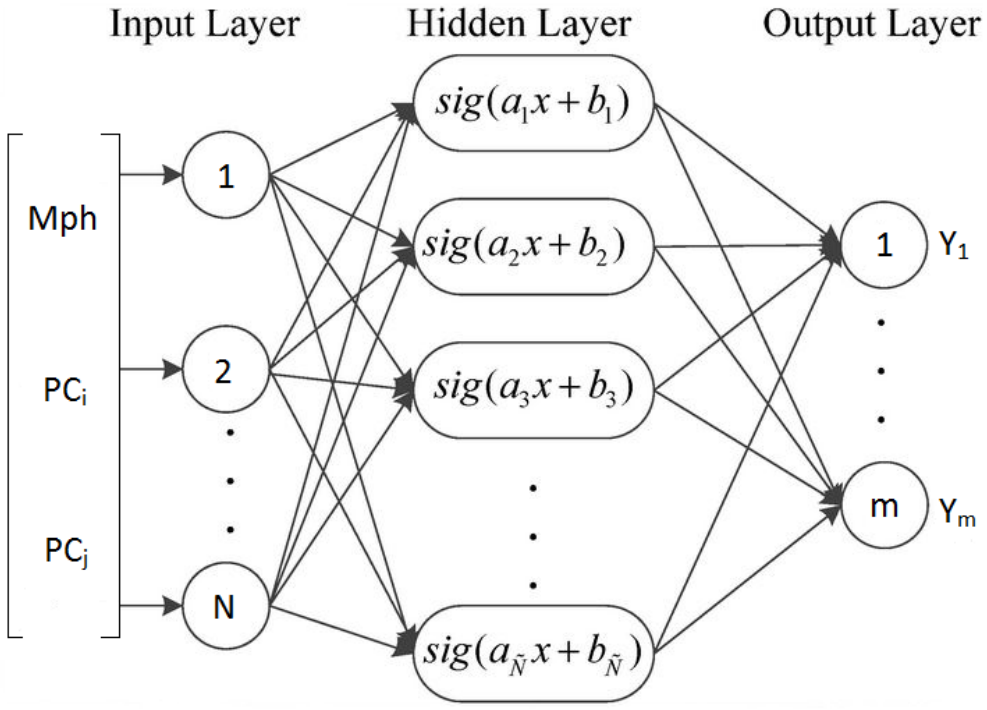

Figure 3.3: Structure of the single hidden layer feed forward neural network using Extreme Learning Machine (ELM).

ters a leave-one-out cross-validation is used, where only one value at a time is excluded from the calibration set and is used for validation, and the model training is reiterated as many times as the number of data. The value of the performance is calculated as the maximum value of R^2 and Pearson's coefficient

obtained in each cross-validation iteration.

3.4 Dam filling strategy design

A novel and promising application of long term meteorological forecast is to use them to inform the filling strategies of large new dam with the aim of minimizing downstream damages due to filling transient. Previous studies have recognized that effects on downstream users depend on the hydrology during the filling period, the initial impoundement of existing dam and the filling policy implemented (see Section 1.1). Three types of filling strategies are considered in literature, including threshold, fractional and absolute(*Zhang et al.*, 2016). The threshold filling strategy permits to impound in the reservoir any streamflow volume in excess of the long-term historical monthly average. Thus, in months with anomalously high flow, the entire above average volume of water can be impounded; however, in months with flow below the average, no impounding is permitted. Threshold strategies generally protect downstream stakeholders from water shortages due to filling transient, but it may significantly slow down dam filling.
Fractional filling strategies consent impounding a specific percentage of total monthly streamflow into the reservoir, this strategy guarantees that some quantity of water can be continuously seized, although this quantity varies month to month and year to year. Fractional strategies generally favour a sharing by upstream and downstream countries of the risk associated with streamflow variability. Absolute filling strategies allow for a guaranteed volume of water to be impounded in the reservoir annually. To fill the reservoir in 4 years, for example, one-fourth of the total reservoir volume may be impounded each year, irrespective of the streamflow. This strategy secures upstream stakeholders, while the downstream counterpart has to bear the risks of the occurrence of droughts (*Zhang et al.*, 2016).
Among the three strategies, we decided to explore the fractional filling given its more equitable sharing risks related to hydrological variability. We will design and evaluate different fractional filling strategies of Gibe III dam in the Omo-Turkana basin (see chapter 2 for details on the case study).
The filling strategies that were implemented and tested are designed to reproduce natural seasonal inflow variability while accounting for the forecasted state of water resources and drought condition in the basin. These strategies will be compared with the actual strategy employed for the filling of Gibe III. The release decision from the dam are defined as a fraction of the inflow and it does not depend on the reservoir level. Such fraction is defined through a

coefficient that depends on the forecasted state of water resources (FSWR) in the basin allowing more release in case of upcoming droughts, and conversely impounding a larger inflow fraction in case of wetter than average conditions. The release strategy is thus defined as follows:

$$u_t = k_s(FSWR) * n_{t+1} \tag{3.8}$$

Several strategies can be defined by varying the set of coefficients k_s. Such strategies and the historical filling strategy are simulated via a conceptual model of the systems described in section 2.4 and their impacts on downstream stakeholders and Gibe III hydropower production are evaluated via a number of key indicators defined in section 2.3. The values of SPEI forecast index are obtained through NIPA procedure combined with ELM model (as described in section 3.3) using two different forecasting seasons: a wet season from June to September and a dry season from December to March.

4

Results

This chapter presents the results obtained regarding the comparison and correction of climate data, the computation of drought indexes, the production of teleconnection-based seasonal forecast, and the definition of alternative reservoir filling strategies.

4.1 Climate data processing

4.1.1 Precipitation

This section presents the results of the daily, decadal, monthly and seasonal comparison of precipitation extracted from TRMM, CHIRPS, and TAMSAT satellite products. As ground truth, we use the observed available data from fourteen rainfall stations located in the Omo basin during the time horizon from January 1998 to December 2008. The technique adopted for the analysis of satellite products consists in a pixel to pixel comparison between ground station grid and remote sensing dataset grid at the resolution of the finest scale satellite product (CHIRPS resolution with $\Delta = 0.05^\circ \times 0.05^\circ$). Ground observations are upscaled to grid resolution by determining their area of influence via Thiessen polygons.
Figure 4.1 shows the mean annual rainfall for the available ground stations and the three different satellite datasets over the period 1998-2008. The wettest region of the basin is in the middle of the basin with TAMSAT dataset reporting the highest amount of precipitation with respect to CHIRPS and TRMM. The driest region is in the south of the basin and along the entire eastern border.

The ground data map reports the observed precipitation values in the ground stations replicated for each cell belonging to the relative Thiessen polygon of influence. In-situ measures and satellites data display similar behavior in terms of precipitation distribution over the basin, but the magnitude of rainfall is generally underestimated by satellite products all over the basin except for the southern part where it is overestimated instead.

Figure 4.2 shows the daily, dekadal and monthly RMSE for the three differ-

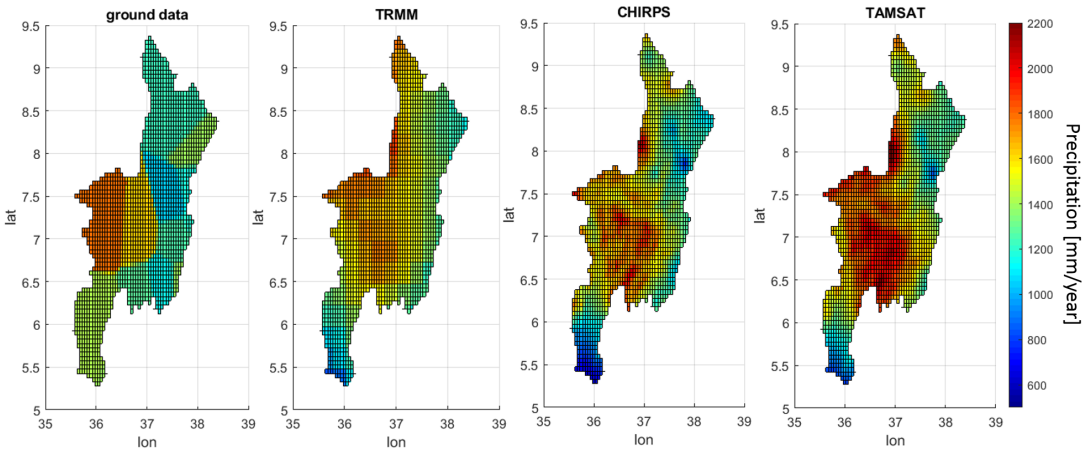

Figure 4.1: Mean annual precipitation over 1998-2008 in the Omo basin for the three different satellite datasets and the available ground stations.

ent satellite datasets with a spatial representation where each pixel is colored with a color scale of blue, with dark blue for high errors and light blue for small errors. On a daily timescale, TAMSAT has the best performances over the basin with lower RMSE values, while extending the temporal aggregation with decadal and monthly datasets the error decreases consistently, and the differences between the three products become less noticeable. Furthermore, the greatest RMSE is generally registered in the middle part of the basin where the rainfall is most abundant. However, the spatial distribution of errors tends to flatten for longer time aggregations, with the monthly scale presenting an almost even error distribution across the whole basin.

Figure 4.3 shows the correlation coefficients. Similarly to the results obtained for RMSE, the first block reports a relatively low correlation between in-situ and satellite datasets at daily time scale, which increases when the aggregation time is extended to decadal or monthly. The most critical area is again the middle Omo basin, and the highest correlation coefficients are in the northern part of the basin. Figure 4.4 summarizes the comparison results reporting the average performance over the entire Omo basin for the different satellite products.

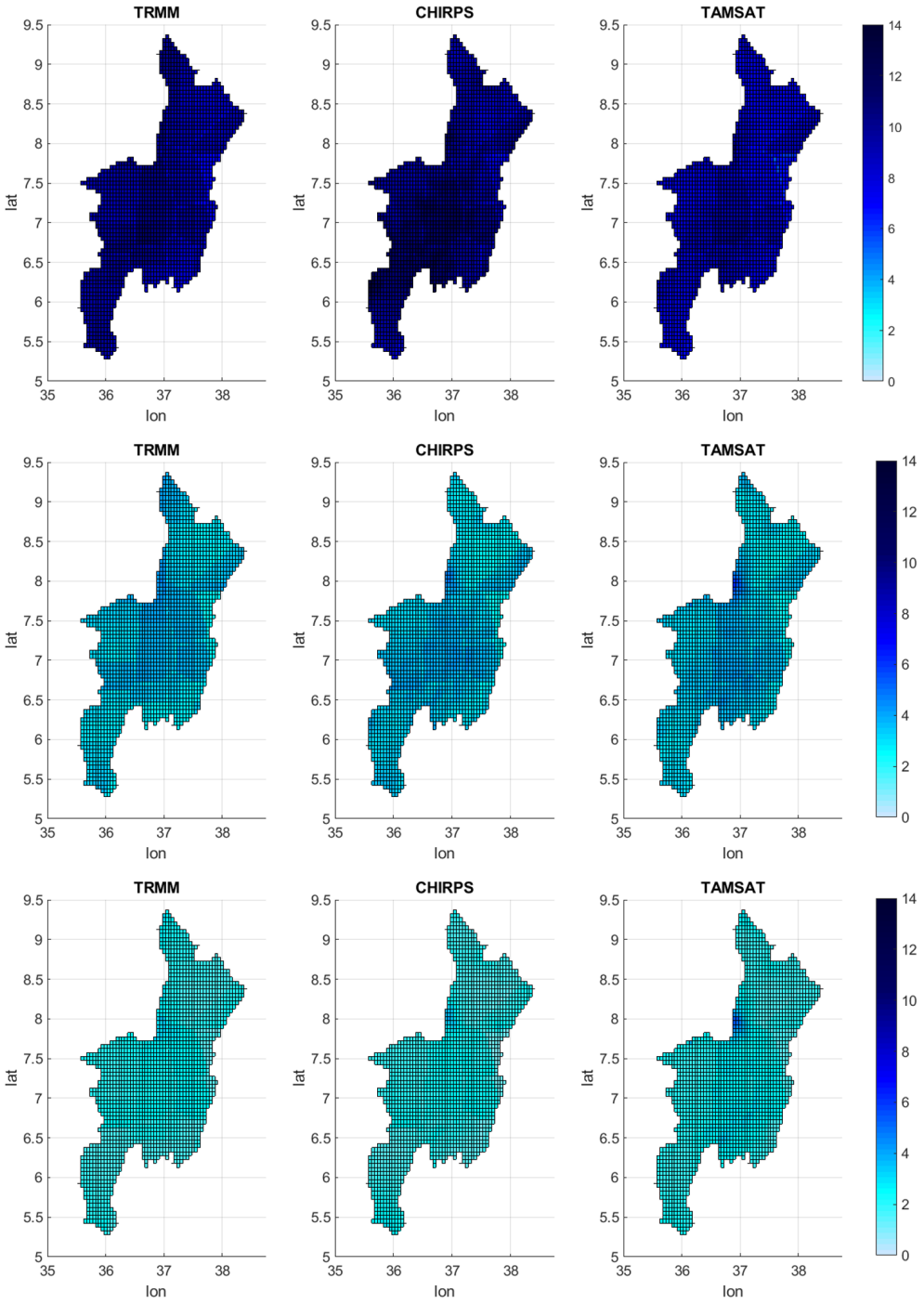

Figure 4.2: RMSE maps for three satellite datasets at different time scale: daily (top), dekadal (center), monthly (bottom)

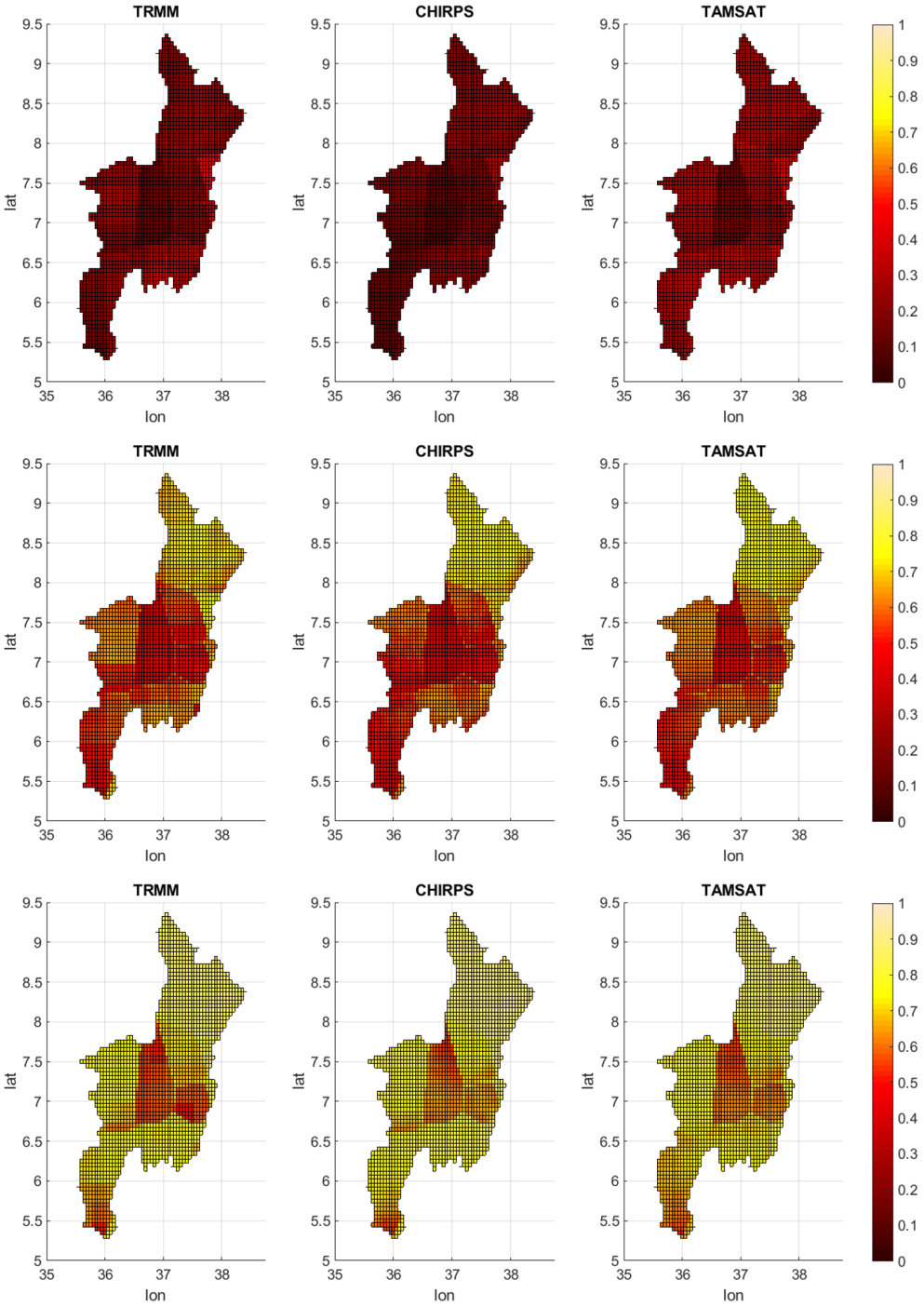

Figure 4.3: Correlation maps for three satellite datasets at different time scale: daily (top), dekadal (center), monthly (bottom)

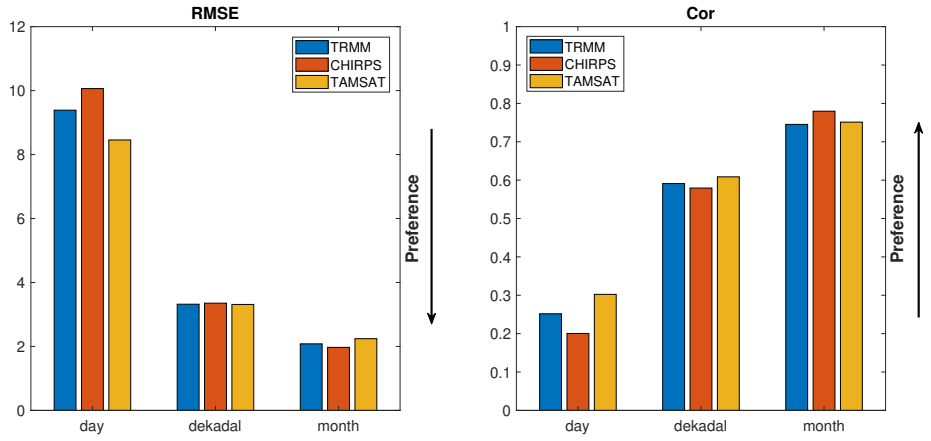

Figure 4.4: Mean RMSE and correlation coefficients over the entire Omo basin

TAMSAT data are the best on a daily time scale but increasing the aggregation span, the performances of the three satellite products are similar.

In addition to the analysis on the spatial distribution of the error, we are also

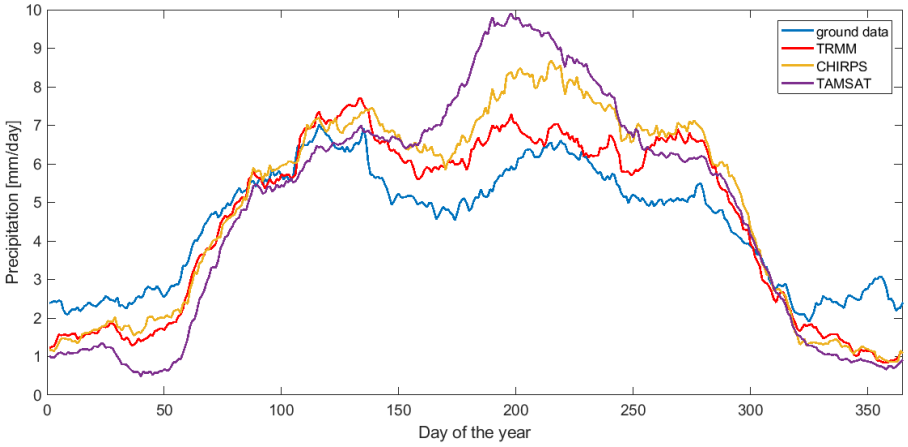

Figure 4.5: Seasonal rainfall at Chida station comparing in-situ data with remote sensing measurments.

interested in how the error is distributed in time, across the different seasons of the year. For this purpose, we compared the annual cyclostationary mean of precipitation recorded in the ground station with the corresponding satellite pixel. Plots are only shown for Chida station (Figure 4.5), situated in the middle of the basin, where we recorded the worst performances and the largest precipitation amount. We can observe that the remote sensing data underestimate precipitation in the dry periods of the year and overestimate precipitation in the wet periods. Dry season underestimation is probably due to technical

restrictions in satellite machinery, as it is impossible to detect very low precipitation (under 5 millimeters) with satellite images. This discrepancies will be eliminated with the bias correction methods.

4.1.2 Temperature

This section presents the results of the daily, dekadal, monthly and seasonal comparison of temperature from MERRA-2 and ORH with data from six available weather stations located in the Omo basin. The comparison is possible from January 1998 to December 2005, due to the ORH dataset available only until 2005. The technique utilized for temperature analysis is the same of rainfall analysis and consists in a pixel to pixel comparison between ground station grid, defined through Thiessen polygons, and remote sensing dataset grid downscaled at the resolution of ORH resolution ($\Delta = 0.1° \times 0.1°$).
Figure 4.6 represents the mean temperature for the available ground stations and the three different satellite datasets over the period from 1998 to 2005. The spatial distribution of temperature reported by the remote sensing dataset differs from the ground stations. In the remote sensing datasets the hottest part of the basin is the southern part and going north the temperature decreases, instead the map representing the in-situ stations shows that the hottest region is the middle-east station.

Figure 4.7 shows the daily, dekadal and monthly RMSE for the two differ-

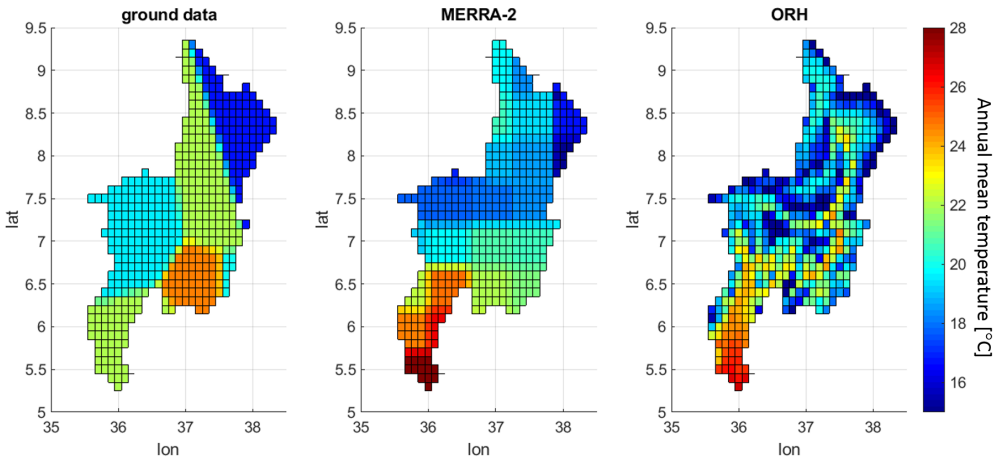

Figure 4.6: Mean annual temperature over 1998-2005 in the Omo basin for the two different satellite datasets and the available ground stations.

ent satellite datasets with a spatial representation where each pixel is colored depending on comparison performances. MERRA-2 has the higher error in the

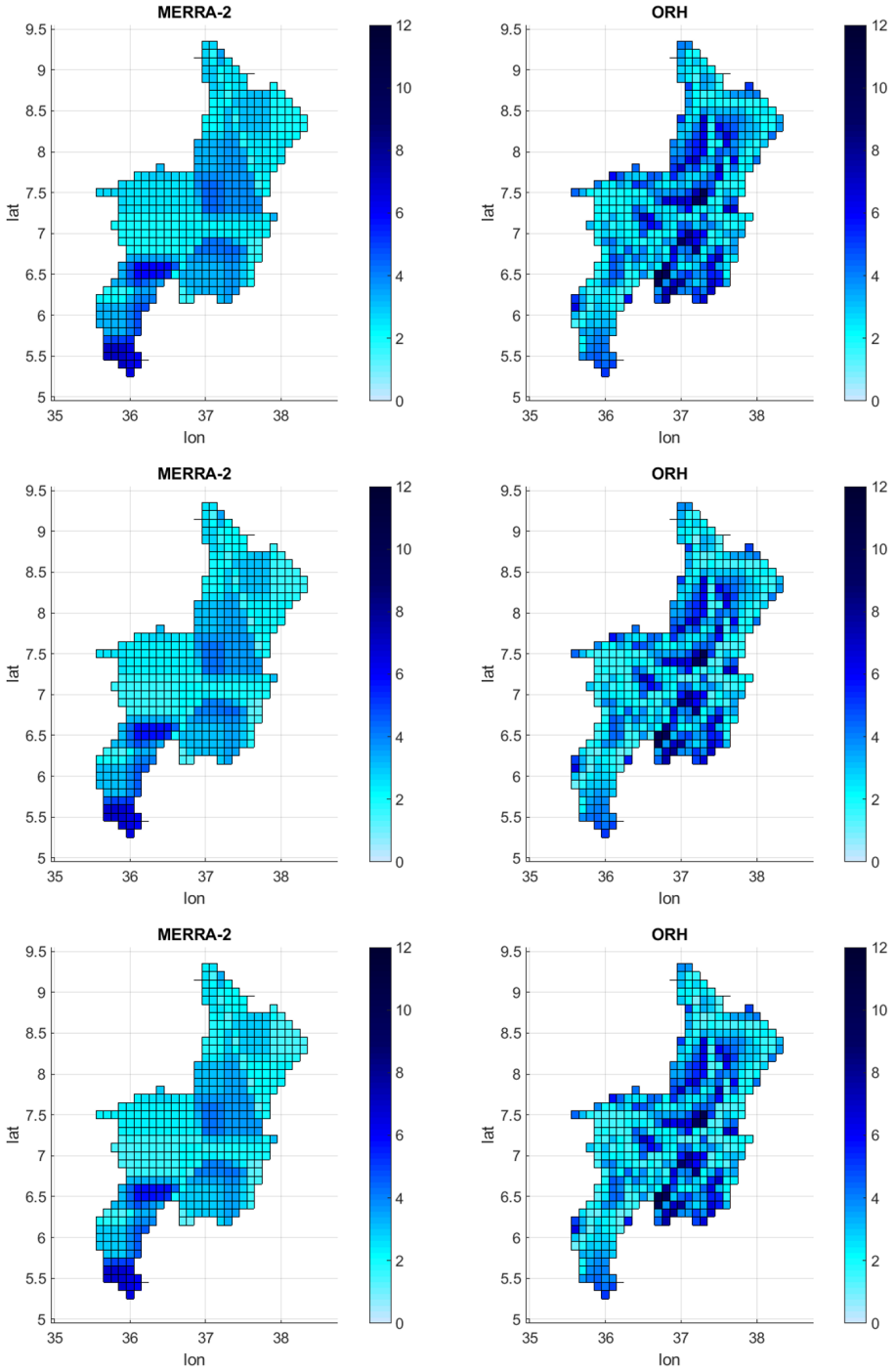

Figure 4.7: RMSE maps for two satellite datasets at different time scale: daily (top), dekadal (center), monthly (bottom)

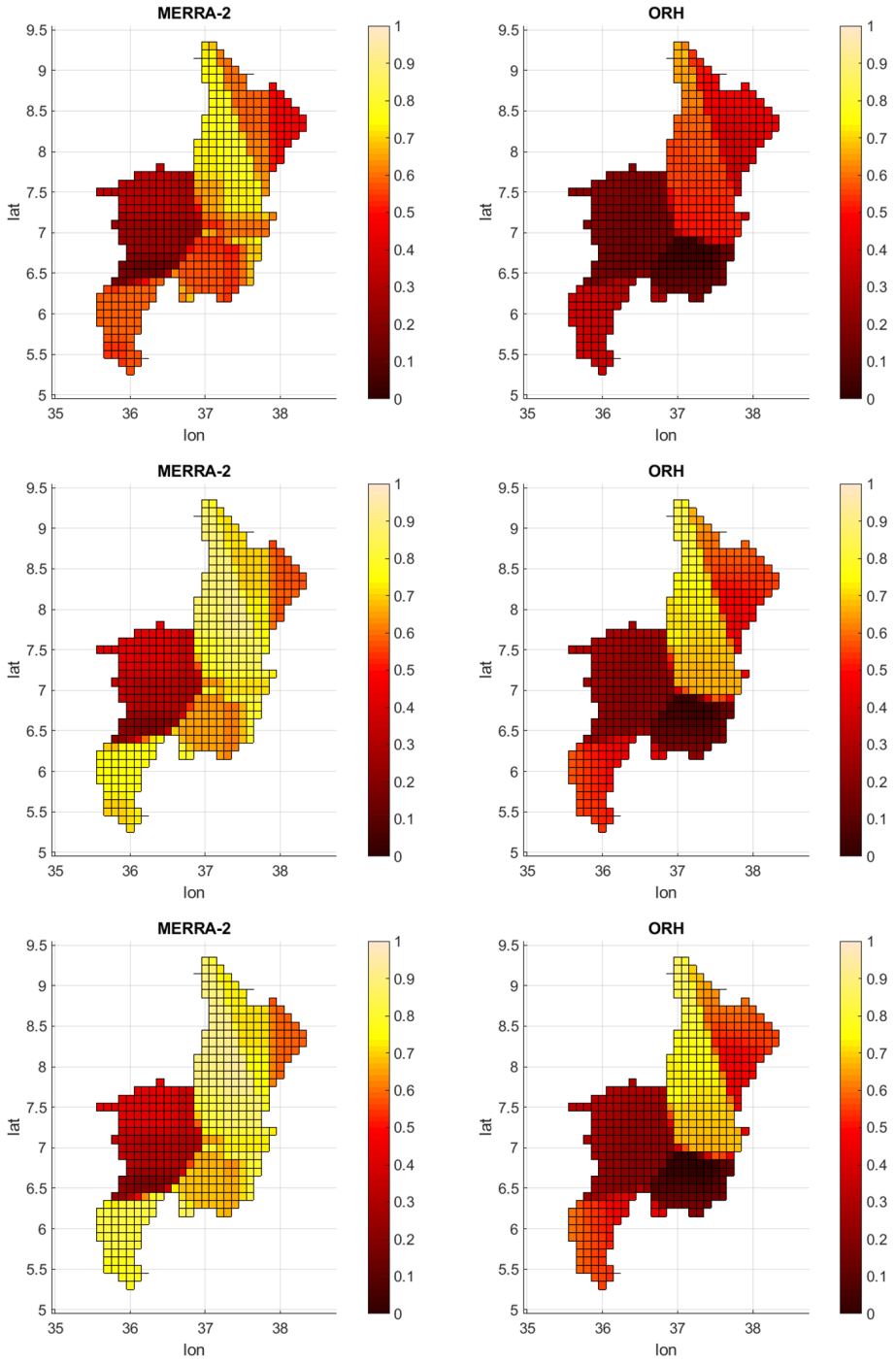

Figure 4.8: Correlation maps for two satellite datasets at different time scale: daily (top), dekadal (center), monthly (bottom)

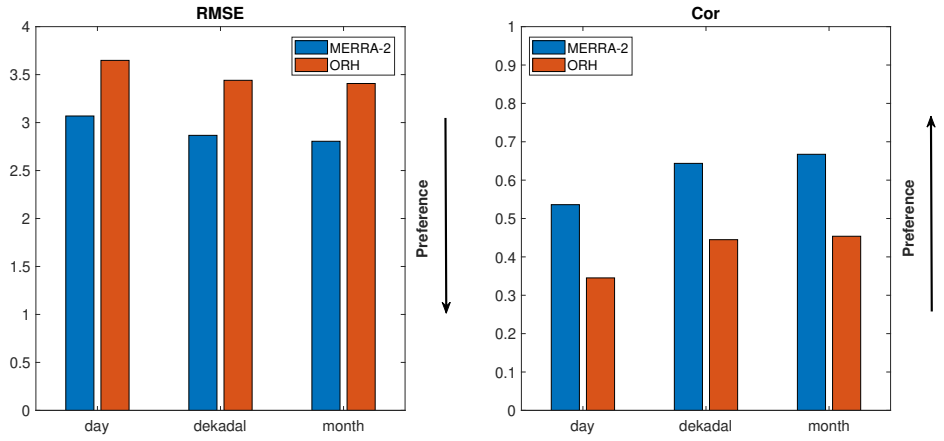

Figure 4.9: Mean RMSE and correlation coefficients over the entire Omo basin

southern part of the basin, instead ORH dataset has worse performances in the south-east part of the basin. In contrast to the behavior observed with precipitation, extending the time aggregation does not significantly improve RMSE values.

Figure 4.8 shows the correlation coefficients for the two different satellite datasets at different time scale and illustrates the correlation between in-situ and satellite datasets. We observe that correlation on a daily scale is higher for MERRA-2 with respect to ORH, increases for both satellite products when the aggregation time is dekadal or monthly, and the worst performances are recorded in the middle-west Omo basin. Figure 4.9 summarizes the comparison results through the mean performances over the entire Omo basin for the different satellite products. It is evident how MERRA-2 has better performances with respect to ORH in terms of RMSE and correlation coefficient.

Moreover, for each ground station we carried out a comparison between the annual cyclostationary mean of ground station measures and the corresponding satellite cells to analyze how the error is distributed in time across different seasons. Plots are shown for Yaya Otena and Jinka weather stations. The top block of Figure 4.10 shows seasonal temperature at Yaya Otena station and highlights that both satellite products underestimate the temperature registered in the weather station, unlike what happens at the Jinka station (bottom block) where the remote sensing datasets overestimate the ground measurements.

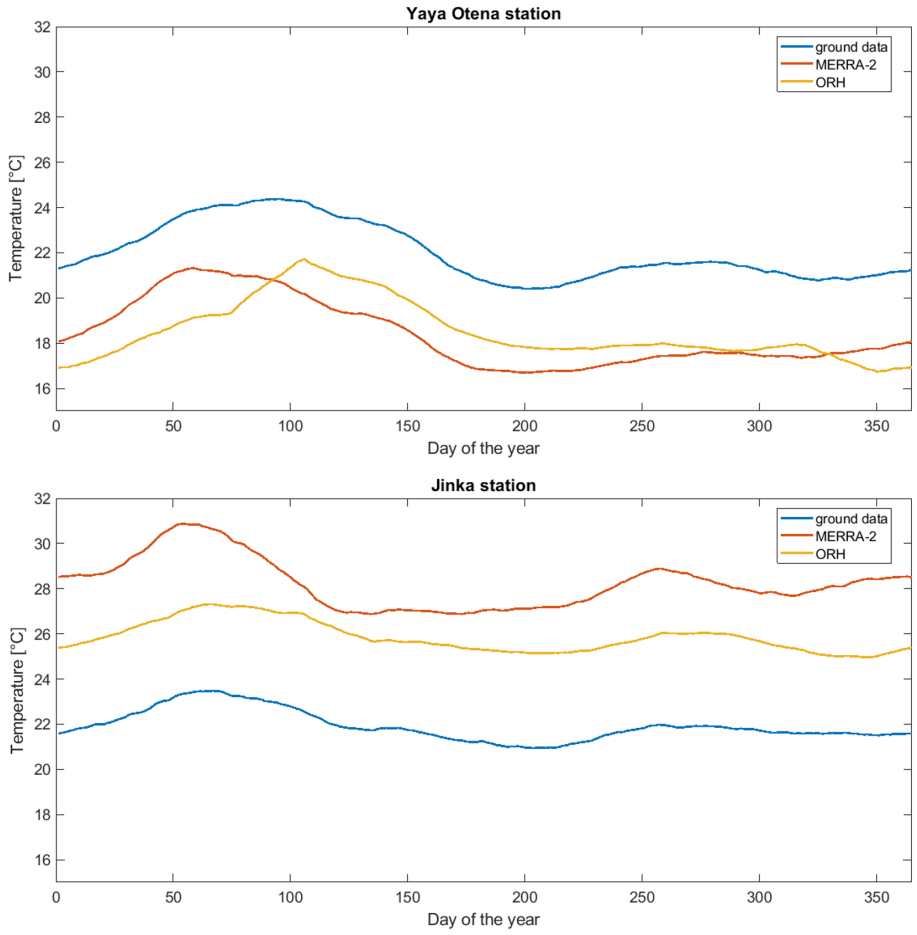

Figure 4.10: Seasonal temperature at Yaya Otena and Jinka from MERRA2 and ORH.

4.1.3 Bias correction

The analysis carried out in the previous section highlighted the presence of systematic errors (namely, bias) in satellite datasets presenting uneven distributions in time and space. In order to reduce the error and improve the quality of satellite data, two bias correction methods are applied and their results compared: mean bias-remove technique and linear scaling (section 3.1.2).
Figure 4.11 shows the mean performance of the rainfall datasets compared with the performance of the same satellite products corrected through mean bias-remove technique (MBR, (*Ajaaj et al.*, 2016)) or linear scaling (LS, (*Fang et al.*, 2015)). The first row represents RMSE, and the second row reports correlation coefficients. Performance improves significantly with the application of bias-remove techniques, but the differences between the two different bias correction techniques is very small and varies depending on satellite product and on time interval considered. Figure 4.12 shows the bias-corrected annual cy-

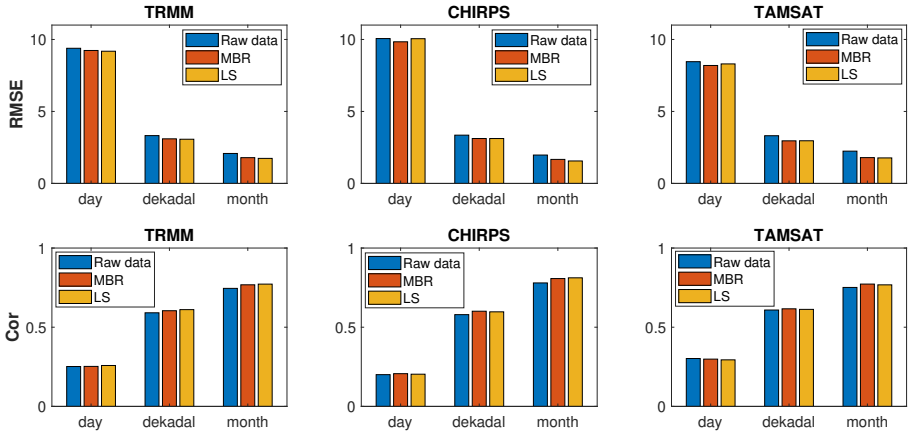

Figure 4.11: Mean RMSE and correlation coefficients over the entire Omo basin for the three rainfall satellite products with different bias-remove techniques.

clostationary mean at Chida station and we notice how in the dry periods the satellite trajectories overlap the ground stations line, while in wet periods the remote sensing lines are lowered and closer to in-situ data. This improvement is more tangible for the linear scaling method where the satellite trajectories are very close to the ground station line also in the wet periods. The others bias correction method applied to different rainfall stations are reported in Appendix A.1.1. Figure 4.13 shows the mean performance of the temperature datasets compared with the performances of the same satellite products corrected through bias correction methods. RMSE is halved removing the bias and correlation coefficient increases more in ORH dataset with respect to MERRA-2.

Figure 4.14 shows the seasonality at Yaya Otena station where a significant improvement in the reproduction of the cyslostationary mean can be recognized with both correction techniques. The others bias correction method applied to different temperature stations are reported in Appendix A.1.2.

In conclusion, in this section we compared the accuracy of different satellite products for precipitation and temperature with different metrics and bias correction algorithms and it is impossible to identify a product that excels over the others in all categories. However, the choice of the most suitable satellite product for precipitation has fallen on TAMSAT dataset, which better describes the rainfall on a daily timescale, and for temperature on MERRA-2 dataset, which better describes the temperature in Omo basin with respect to ORH. Linear scaling turned out to be a generally better bias-remove technique to remove systematic bias present on satellite measurements.

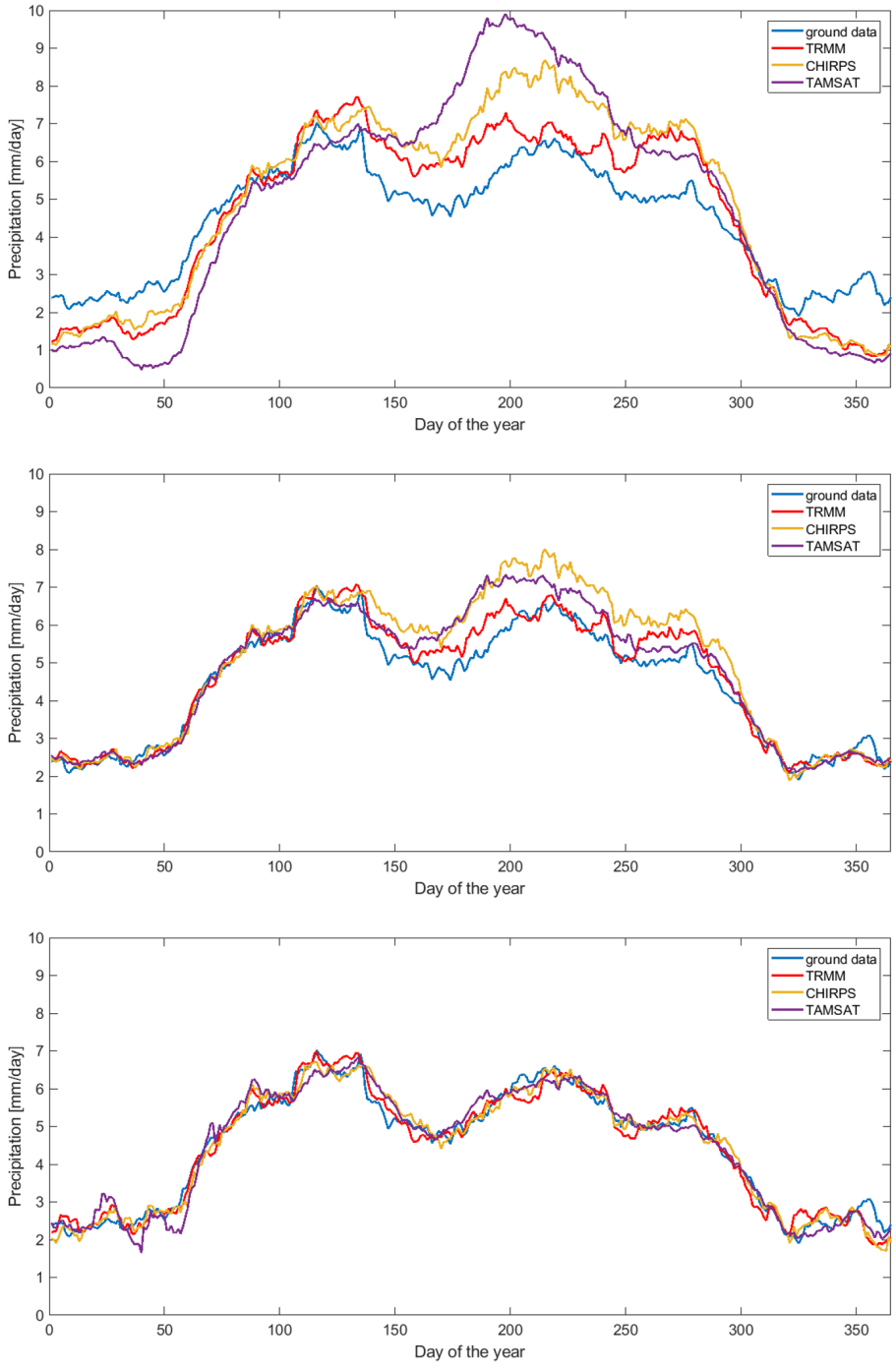

Figure 4.12: Seasonal rainfall at Chida station comparing in-situ data with remote sensing measurments: raw data (top), corrected with mean bias-remove technique (center), corrected with linear scaling technique (bottom).

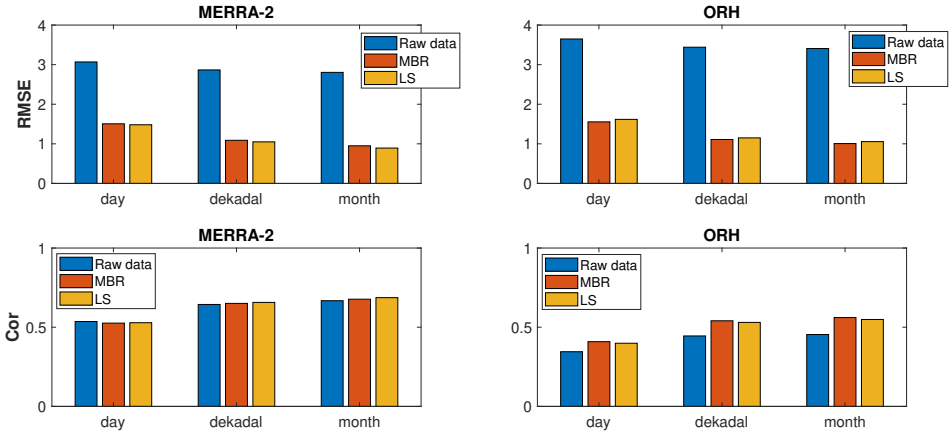

Figure 4.13: Mean RMSE and correlation coefficients over the entire Omo basin for the two temperature satellite products with different bias-remove techniques.

4.2 Drought indexes comparison

This section employs the satellite derived precipitation and temperature datasets produced in the previous section to compute two statistical drought indexes: SPI and SPEI. By using satellite products we were able to extend the time horizon to 32 years from 1986 to 2017 in order to better characterize the hydrological processes of the region.
The SPI and SPEI values are computed for six basin cells, shown in Figure 4.15, which are selected with the aim to detect all the different conditions in terms of precipitation and temperature present inside the basin. The indicators were computed from 1986 to 2017 for different cumulation periods: 1 month (related to meteorological drought), 3 months and 6 months (related to agricultural drought), 9 and 12 months (related to hydrological drought). A drought event is registered when the indicators falls below -1 for two consecutive months and ends when it turns positive.

4.2.1 SPI

In Figure 4.16 the SPI indicator is represented and computed using precipitation, with accumulation period of 9 months for the entire Omo basin. It is possible to identify five main drought events, colored in red: the first three events have an extended duration of at least three years and the subsequent

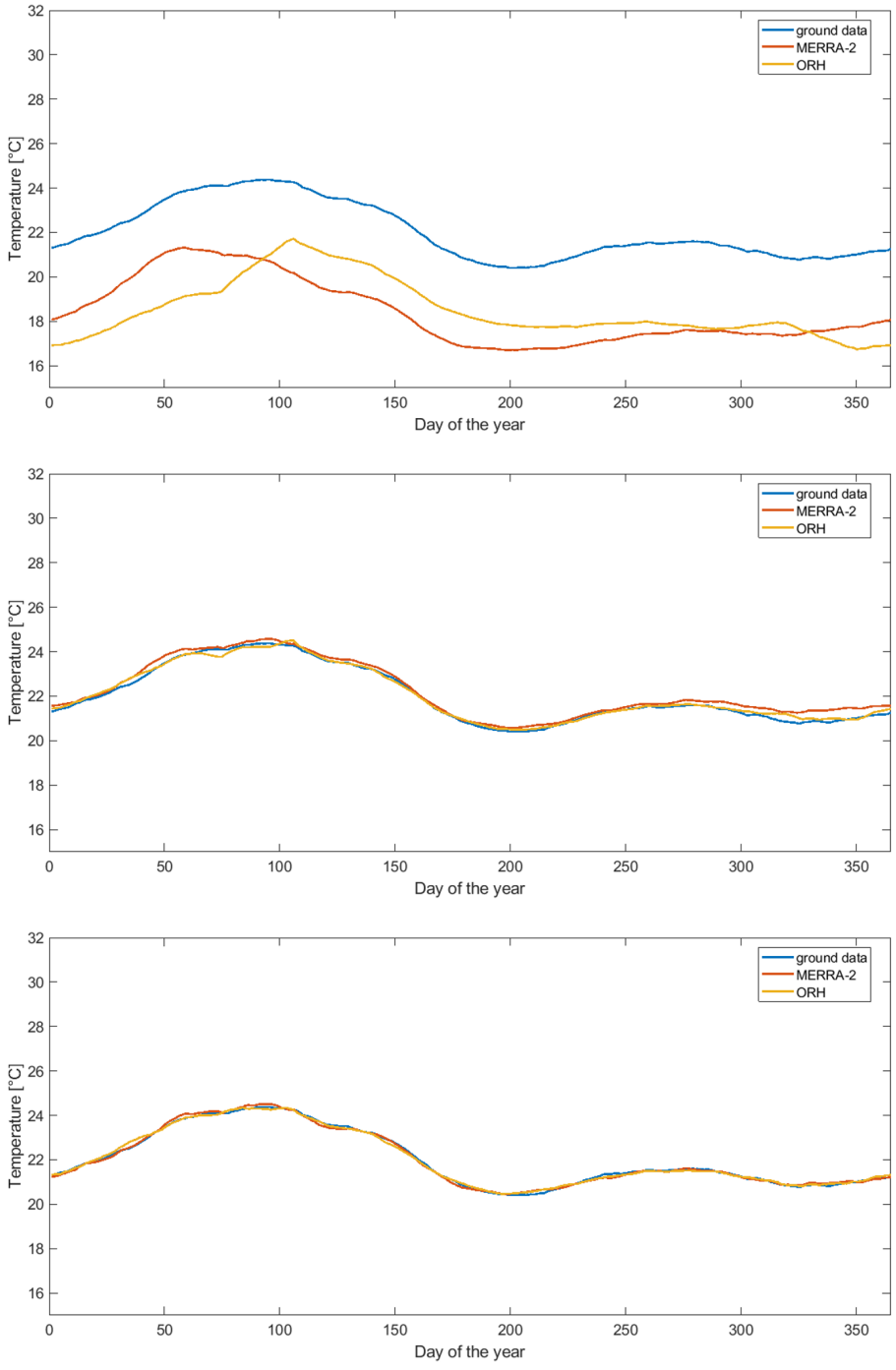

Figure 4.14: Seasonal temperature at Yaya Otena station comparing in-situ data with remote sensing measurments: raw data (top), corrected with mean bias-remove technique (center), corrected with linear scaling technique (bottom).

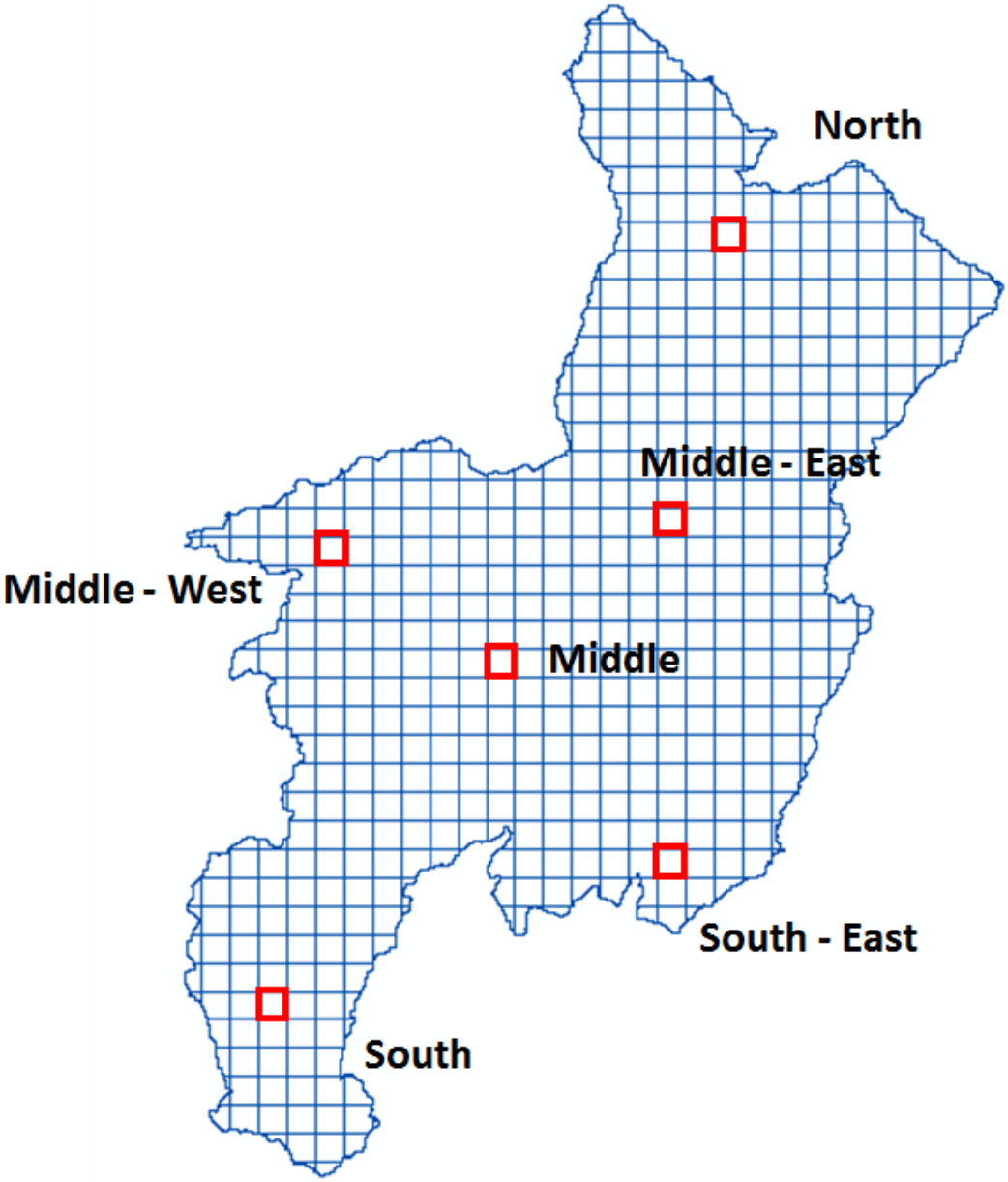

Figure 4.15: Drought zones in the Omo basin.

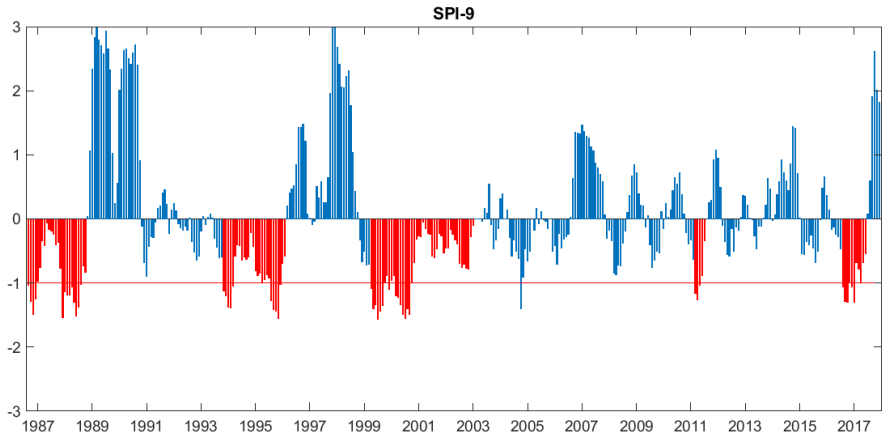

Figure 4.16: SPI index with accumulation period of 9 months in the Omo basin.

two events have a shorter duration. The droughts are interspersed by wet periods, in particular in the first half of the temporal horizon and at the end of 2017.

Figure 4.17 shows the SPI indicator with accumulation period of 9 months for each zone detected in the Omo basin. Droughts in each zone become more frequent and their duration decreases with respect to the index value computed for the entire basin using an average value of precipitation. The five events identified in the previous figure are still recognizable, despite being interrupted by short wet periods or accompanied by further dry events in the second half of the time horizon. The middle-west zone has a different behavior with respect to the other and does not identify drought events in the second half of the horizon.

Moving the focus on a single zone of the basin, in Figure 4.18 we can see what happens in the middle-east zone, the area with the lowest amount of rainfall, varying the accumulation period. With long accumulation periods the drought events are less in number and more lasting, typical of hydrological droughts, decreasing the temporal aggregation they become more intermittent with short durations, as frequently happens in meteorological droughts.

4.2.2 SPEI

Figure 4.19 represents the SPEI indicator, that involves precipitation and temperature variables, with cumulation period of 9 months for all the Omo basin. It is possible to identify six main drought events: similar to SPI case described

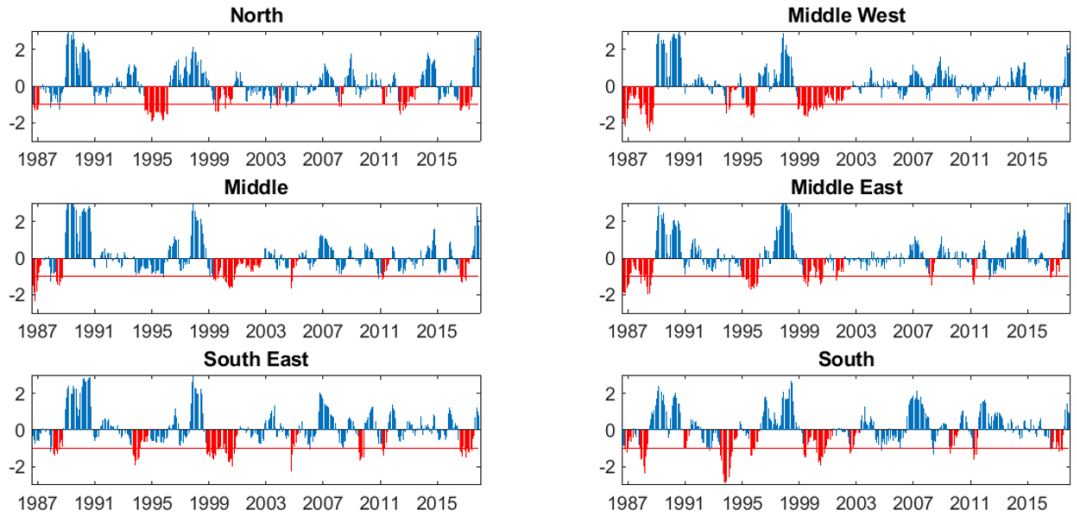

Figure 4.17: SPI index with accumulation period of 9 months in the Omo basin for the six drought zones.

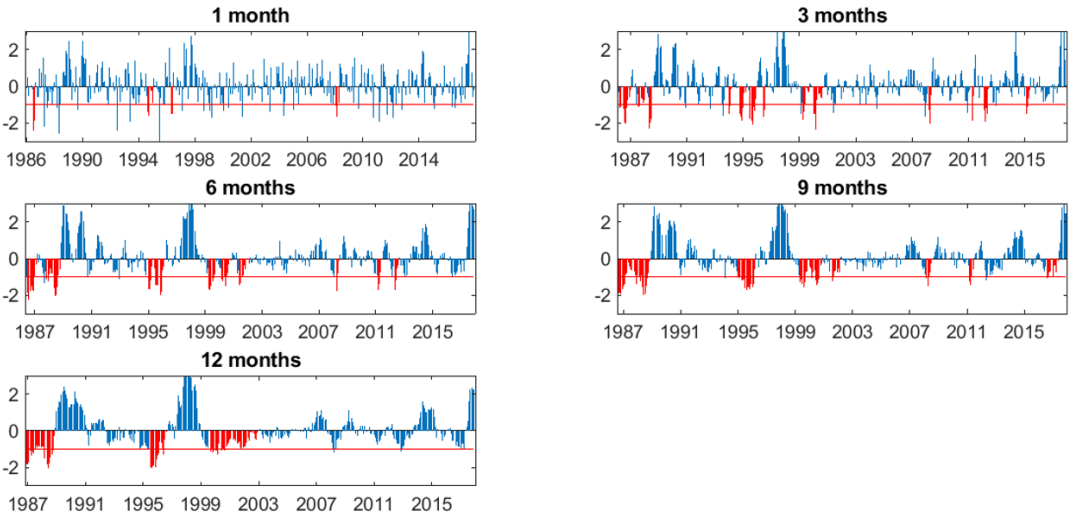

Figure 4.18: SPI index in the middle-east zone with different accumulation periods.

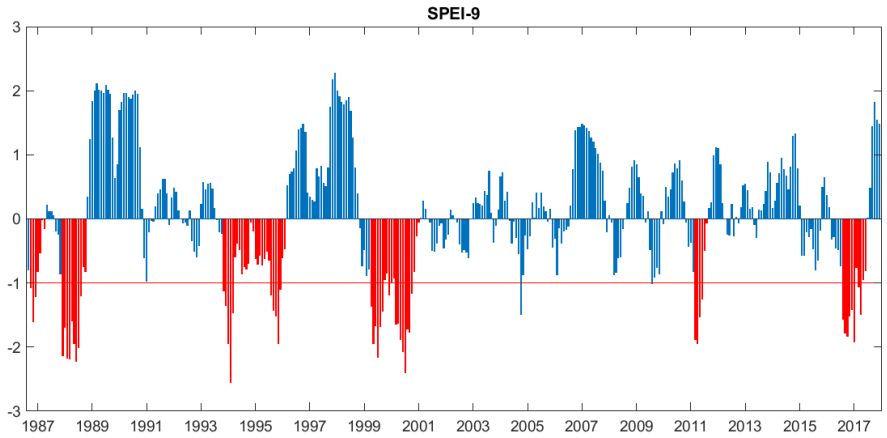

Figure 4.19: SPEI index with accumulation period of 9 months in the Omo basin.

above (Figure 4.16), except for the drought event lasting from 1987 to the end of 1988 which is splitted into two different events.

Figure 4.20 shows the SPEI indicator with cumulation period of 9 months for each zone detected in the Omo basin using an average value of precipitation and temperature. Increasing the spatial scale the drought events become more frequent and shorter with respect to the index computed for the entire basin. The drought magnitude and frequency are more significant in the zones that combine low precipitation and high temperature like middle-east, south-east and south.

Focusing on a single zone of the basin, in Figure 4.21 we can see the drought events in the middle-east zone, area with lowest amount of rainfall and a warm temperature, at various cumulation period. Considering a cumulation period of 1-3 months the drought events are frequent and have a short duration, instead increasing cumulation period dry periods become longer and less in number during the horizon.

4.2.3 Comparative analysis of different drought indexes

Figure 4.22 compares the drought conditions in the Omo basin with 9 months cumulation period (hydrological drought) for SPI and SPEI indexes averaging precipitation and temperature all over the basin. We can detect five main events that have the same duration but different intensity, when assessed with different drought indexes. SPEI generally reports more intense droughts, due to the presence of the temperature variable in the computation that sharpens the drought magnitude. The main differences between the two indexes are in

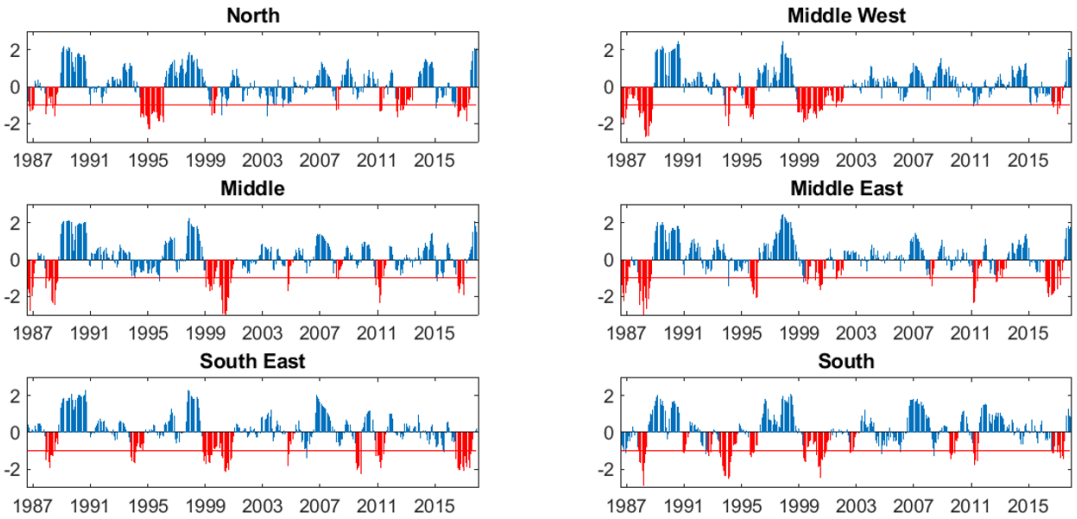

Figure 4.20: SPEI index with accumulation period of 9 months in the Omo basin for the six drought zones.

the first years of the horizon, where SPEI splits into two different events the single dry period detected by SPI from 1986 to the end of 1988, and in the middle years where the third drought event has shorter duration in SPEI index.

In this climate regime the role of temperature is of key importance in identifying dry periods and their intensity, therefore in our following analysis we decided to consider the SPEI indicator to assess drougths in the Omo basin where rainfall and evapotranspiration are strictly connected.

4.3 Seasonal forecast identification

In the previous sections, we have selected the most suitable satellite products for precipitation (TAMSAT) and temperature (MERRA-2), corrected them with linear scaling bias correction technique, and used them to derive drought indexes. In this section, we apply the NIPA procedure to forecast rainfall and drought events through SPEI index in the Omo river basin.

4.3.1 Detection of relevant climate signals (NIPA)

As argued in section 1.2, water management can greatly benefit from the indication provided by middle- to long-term prediction of future water availabil-

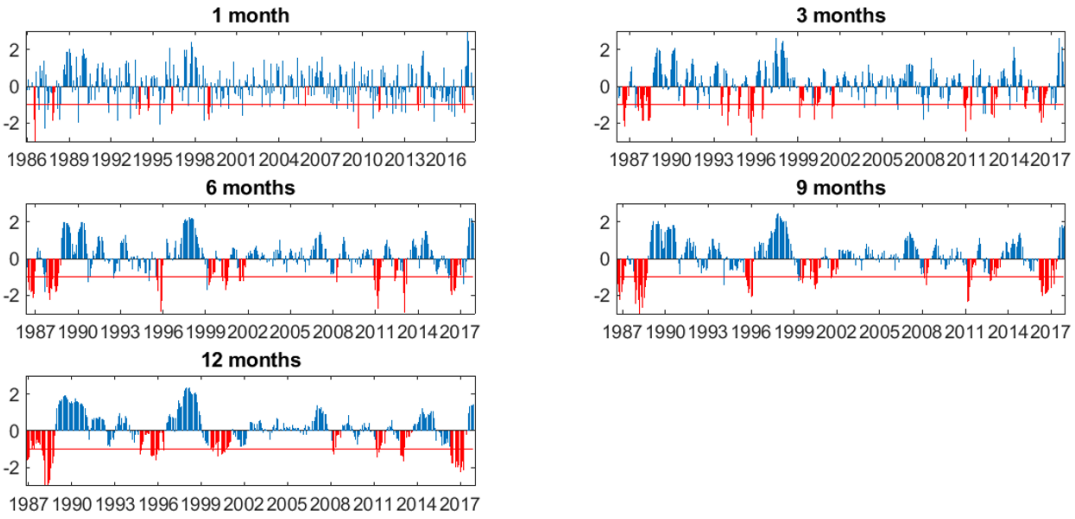

Figure 4.21: SPEI index in the middle-east zone with different accumulation periods.

ity. Given the outcome of the analysis documented in the previous sections of this chapter, we consider that the key variables related to the state of water resources in the basin are precipitation and SPEI index. In particular, the focus is on the Keremt season lasting from June to September (JJAS) which is the main rainy season in the region and the management of this large volume of water critical in drought management.

Given the well documented influence of teleconnections in determining climate oscillation in the region (see section 1.2), we employ the NIPA procedure (described in section 3.3) to detect the relevant teleconnections in the area that will constitute the basis for our data driven middle and long term forecast. The large-scale climate signals selected for detection are North Atlantic Oscillation (NAO), El Niño Southern Oscillation (ENSO), Pacific Decadal Oscillation (PDO), Indian Ocean Dipole (IOD) and Atlantic Multidecadal Oscillation (AMO), as measured by Hurrel NAO Index, MEI Index, Mantua PDO Index, DMI and AMO index, respectively. ENSO (*Zimmerman et al.*, 2016) was selected because of its influence on climate worldwide. NAO (*Penso*, 2018), PDO (*Wang et al.*, 2014), IOD (*Williams and Hanan*, 2011) and AMO (*O,ÄôReilly et al.*, 2017) were selected because of their geographical proximity to the study site and their recognized impact on Africa.

After defining the local variable to predict and the teleconnection patterns to investigate, NIPA is run individually for each climate index, variable and for several lag times (4-5-6-9-12 months) in order to detect the portions of SST that are significantly correlated (significance level >= 95%) with local meteorology

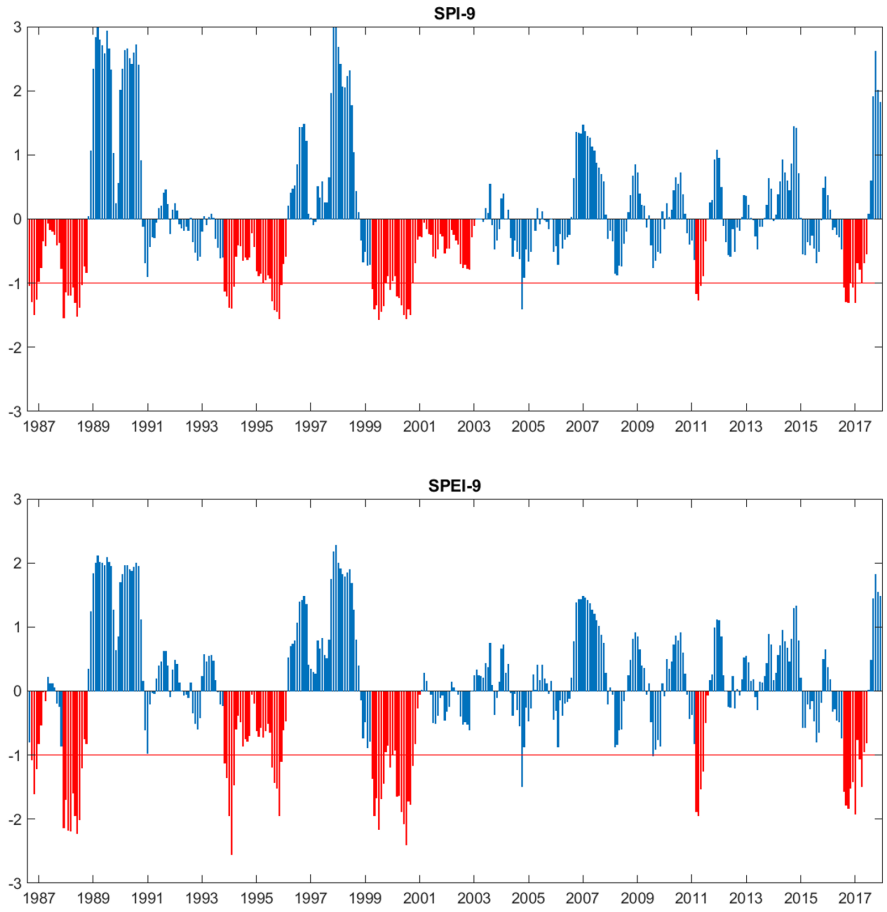

Figure 4.22: SPI and SPEI indexes in the Omo basin with accumulation period of 9 months.

for each phase of climate signals at different delays. When predicting the SPEI index, the considered cumulation period is equal to the lag time. The map in Figure 4.23 reports one examplificative result of correlation maps between precipitation in the Keremt season and selected SST 4 months ahead for the MEI index, indicative of the ENSO phenomenon. In MEI positive years, a higher number of significant cells are detected with positive correlations in western Pacific, in the Atlantic and in the Indian coasts of central Africa and negative correleted cells in central Pacific Ocean. In MEI negative years the gridpoints located in central Pacific Ocean and in the Atlantic Ocean are positevely correlated and in a small area of Mexican coast of Pacific Ocean are negatevely correlated. The others correlation maps for the NAO, PDO, DMI and AMO indexes are reported in Appendix A.2.1.

In order to determine the confidence level of the detected correlations and limiting the risk of the emergence of spurious correlations, we ran a Monte Carlo analysis (see section 3.3.1 for details). Table 4.1 reports the results of the detection analysis in term of phase dependent correlation and confidence level. We can observe how increasing the lag time the correlation coefficients rise and the same happens for the confidence level.

Predictions for precipitation in JJAS (P_{JJAS}) are made also running the 'all-years' (or 'onephase') model, where data are not split into phases. This allows to compare NIPA results with the outcomes of a traditional forecasting approach, which utilizes the same model for all the phases of a certain large-scale climate pattern. With a lag time of 4-5-6 months the correlation coefficient is constant, but when lag time increases (9-12 months) correlation grows.

After showing the NIPA results for the precipitation, we focus on the SPEI index showing the correlation maps with a 9 months lag time (and 9 months time aggregation) that involved $SPEI_{JJAS}$ and the SST anomalies from September-October-November-December (SOND).

Figure 4.24 shows the numerous gridpoints selected using MEI index whith negative ENSO years which detect an area positively correlated in the Pacific Ocean and negatively correlated in the Asiatic coasts of Pacific Ocean, in the Atalntic Ocean, in the eastern part of Mediterranean Sea and in the eastern part of Indian Ocean. Instead in the positive years of MEI index are found significant cells positively correlated in the North Atlantic Ocean and few cells negatively correlated in the south of Atlantic Ocean. The others correlation maps for the NAO, PDO, DMI and AMO indexes are reported in Appendix A.2.1.

Then, deterministic hindcasts are generated and the Monte Carlo analysis is performed computing for each index and for each lag time the confidence level

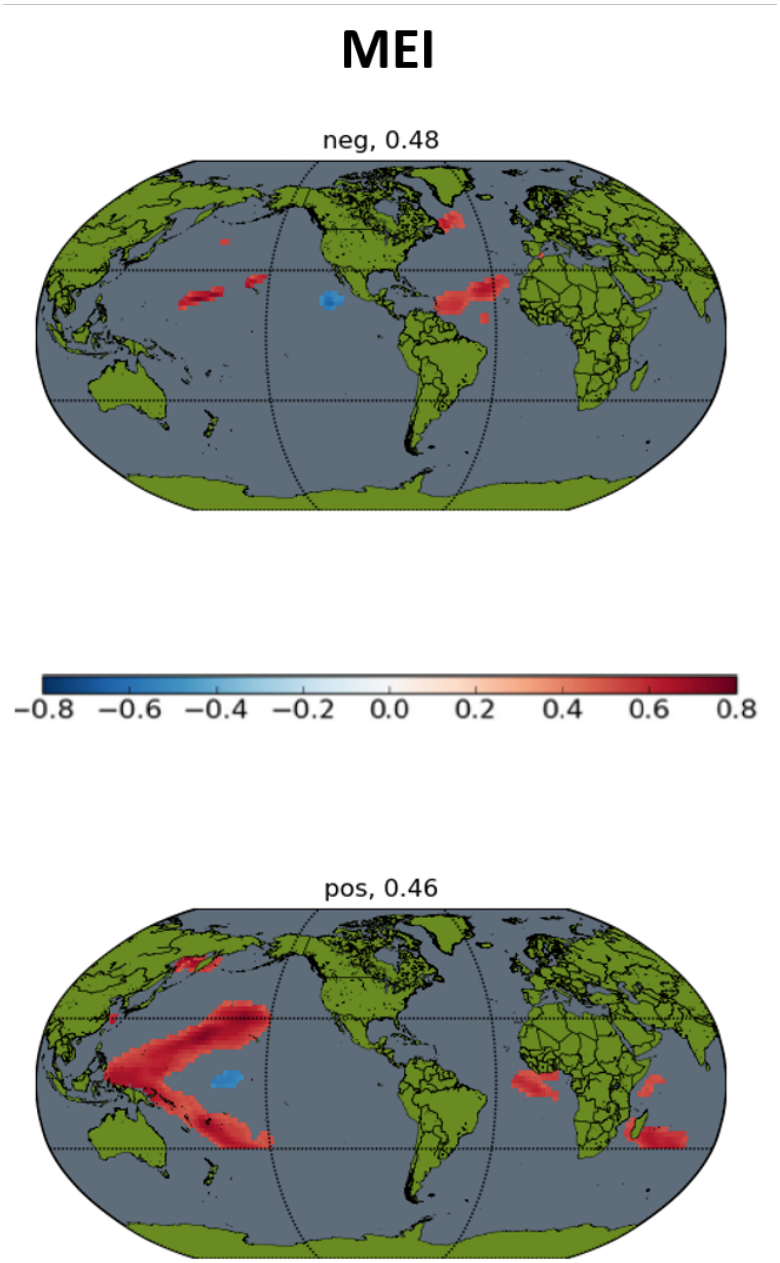

Figure 4.23: Correlation maps between FMAM SST gridded anomalies and JJAS observed precipitation, generated by binning the years through MEI index.

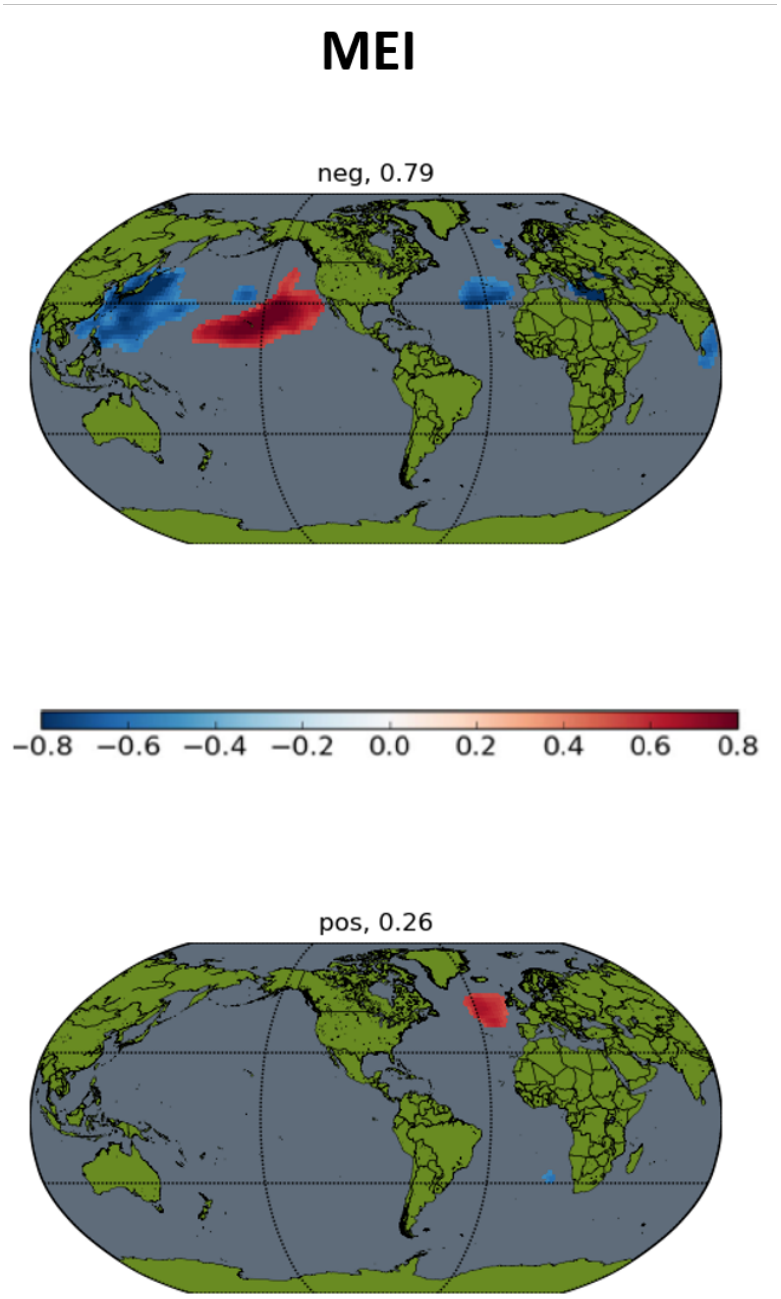

Figure 4.24: Correlation maps between SOND SST gridded anomalies and JJAS observed SPEI at 9 months cumulation period, generated by binning the years through MEI index.

Table 4.1: For each phase of each climate index and for each lag time the following are reported: 1) correlation coefficients in cross-validation between predicted P_{JJAS} and observations and 2) level of confidence of the predictions.

	phases	**Lag 4**		**Lag 5**		**Lag 6**		**Lag 9**		**Lag 12**	
		cor	conf	cor	conf	cor	conf	cor	conf	cor	conf
NAO	pos	0.45	46.2	0.51	95.2	0.42	82.9	0.46	93.0	0.59	99.6
	neg	0.58	95.7	0.37	49.8	0.70	68.3	0.63	87.0	0.69	71.4
MEI	pos	0.46	95.2	0.48	91.9	0.50	95.3	0.50	95.5	0.68	99.7
	neg	0.48	54.5	0.52	81.6	0.57	79.2	0.59	94.1	0.60	92.3
PDO	pos	0.54	96.2	0.61	95.2	0.48	80.9	0.51	97.5	0.55	97.7
	neg	0.46	43.1	0.39	85.1	0.43	77.8	0.55	71.9	0.72	97.9
DMI	pos	0.57	79.2	0.37	41.8	0.31	42.4	0.35	25.8	0.63	88.8
	neg	0.58	94.2	0.60	92.8	0.60	97.8	0.68	99.0	0.51	98.9
AMO	pos	0.54	83.2	0.55	67.6	0.45	36.5	0.39	47.4	0.43	48.0
	neg	0.55	92.6	0.45	89.9	0.58	97.2	0.73	99.7	0.88	100.0
all years		0.48	-	0.48	-	0.48	-	0.51	-	0.53	-

that are shown in Table 4.2 coupled with the correlation coefficients between SST anomalies and $SPEI_{JJAS}$ obtained from correlation maps. Predictions for $SPEI_{JJAS}$ are made also running the 'all-years' (or 'onephase') model. With an increasing lag time the correlation coefficient grows, but when lag time reaches 12 months correlation diminishes.

Looking at the performances in Tables 4.1 - 4.2 we can identify the best signals to forecast precipitation and SPEI index by balancing correlations and confidence. In the case of rainfall we select NAO, MEI, and AMO indexes all with a lag time of 12 months, instead for SPEI we select MEI, PDO and AMO signals with a lag time of 9 months.

Table 4.2: For each phase of each climate index and for each lag time the following are reported: 1) correlation coefficients in cross-validation between predicted $SPEI_{JJAS}$ and observations and 2) level of confidence of the predictions.

	phases	Lag 4		Lag 5		Lag 6		Lag 9		Lag 12	
		cor	conf	cor	conf	cor	conf	cor	conf	cor	conf
NAO	pos	0.58	70.9	0.66	72.5	0.68	56.6	0.44	42.7	0.60	86.3
	neg	0.62	95.2	0.64	83.1	0.68	81.7	0.49	6.2	0.41	13.0
MEI	pos	0.71	47.2	0.60	37.3	0.59	38.5	0.26	98.7	0.69	94.5
	neg	0.71	99.1	0.63	98.7	0.64	99.0	0.79	40.4	0.64	95.1
PDO	pos	0.68	91.7	0.50	90.5	0.54	85.7	0.51	66.9	0.41	98.7
	neg	0.55	88.4	0.68	75.8	0.72	79.8	0.80	90.0	0.84	92.9
DMI	pos	0.55	84.4	0.76	66.0	0.64	52.9	0.34	55.6	0.41	27.5
	neg	0.55	88.6	0.56	98.0	0.62	84.8	0.70	79.5	0.63	82.1
AMO	pos	0.47	64.6	0.45	65.2	0.58	60.7	0.66	94.2	0.47	62.4
	neg	0.69	88.1	0.56	97.2	0.57	96.7	0.46	62.8	0.71	97.9
all years		0.42	-	0.46	-	0.51	-	0.53	-	0.34	-

4.3.2 Multi-variate seasonal meteorological forecast

In this step, the previously obtained PCs are used as input to a multivariate prediction model that is calibrated and validated to reproduce the observed rainfall and SPEI index. As specified in Section 3.3.2, a leave one out cross-validation is performed for each signal, to limit the risk of over-fitting. A non-linear ELM model is calibrated for each selected signal, and for each bivariate combination of such signals. Inputs of the models are the signal phase (or bi-variate combination of phases) and the PC of the relevant SST.
Figure 4.25 shows the results obtained for rainfall prediction cross-validating an ELM model using as inputs the phase and the PC of the ENSO signal. In the first years the model struggles to reproduce the observed values of the index, while in the last decade the trajectory of forecasted precipitation is very close to the observed one ensuring excellent performance in terms of correlation coefficient equal to 0.87 and R^2 equal to 0.76. Complete results for the seasonal

precipitation forecast can be seen in Appendix A.2.2.
Models accuracies in crossvalidation are summarized in Table 4.3 where is evident how the univariate model with MEI index provided the best forecasts, while for the bivariate model the best correlation is obtained coupling NAO and AMO indexes.

Figure 4.26 shows the forecasts obtained with SPEI index from ELM model

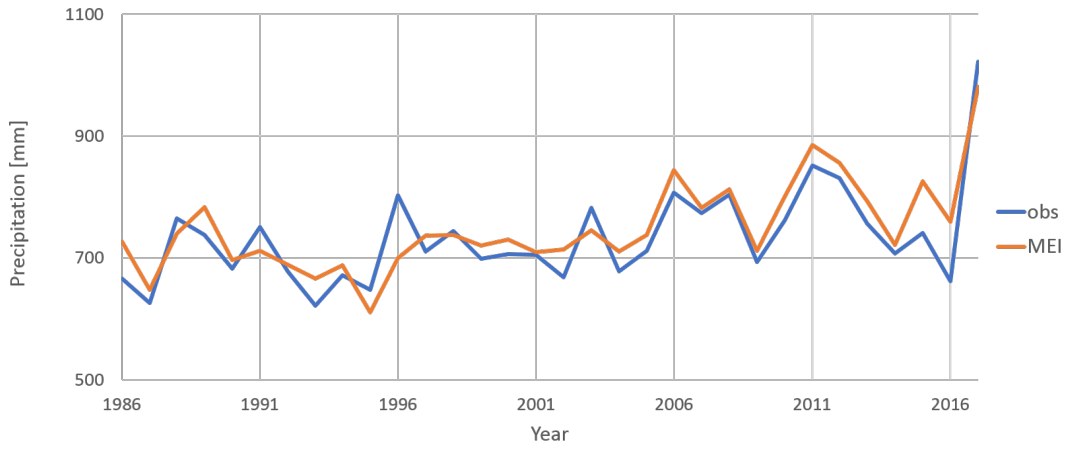

Figure 4.25: Observed and predicted precipitation for univariate JJAS season with MEI index.

Table 4.3: Performance of ELM model in cross-validation using different climate signals and 12 months lag time: precipitation forecasts.

Signals	Cor	R^2
NAO-12	0.77	0.60
MEI-12	0.87	0.76
AMO-12	0.85	0.72
MEI12-NAO12	0.77	0.59
MEI12-AMO12	0.79	0.62
NAO12-AMO12	0.86	0.73

with univariate signals by MEI index. In the first half of the time horizon the model struggles to replicate the peaks and in the last decade the trajectory of

forecasted SPEI index is very close to the observed one providing excellent results in terms of correlation coefficient equal to 0.92 and R^2 equal to 0.82. Complete results for the seasonal SPEI forecast can be seen in Appendix A.2.2.
Table 4.4 provides a summary of the performance of each method, where the univariate model with MEI index provided the best forecasts and coupling the signal indexes with bivariate model the correlations are low respect to univariate models.
Finally, it is useful to underline that the predictions of SPEI index with ENSO signal are more accurate with respect to rainfall forecasts, for this reason in the following section (Section 4.4) are utilized the drought predictions to implement Gibe III filling strategies.

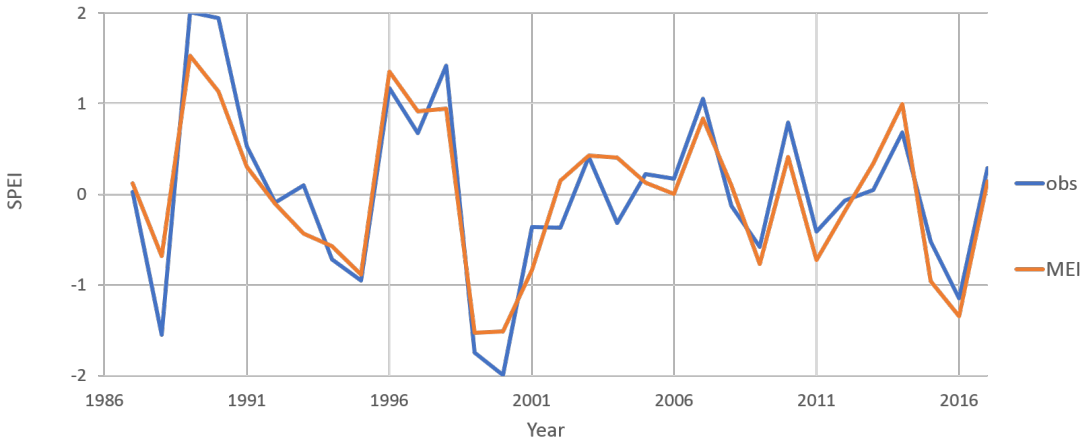

Figure 4.26: Observed and predicted SPEI index for univariate JJAS season with MEI index.

4.4 Dam filling strategy design

In this section, we employ the 9 months ahead SPEI forecasts to define alternative filling strategies for Gibe III reservoir that consider the predicted state of water resources in the Omo basin in order to reduce the impacts of the filling period for downstream water users. The filling strategy is defined as in equation 3.8, where the forecasted state of water resources is represented by the forecasted SPEI.

$$u_t = k_s(SPEI) * n_{t+1} \tag{4.1}$$

SPEI prediction is updated twice a year for a wet season (April to November) and a dry season (November to April). We designed seven filling strategies which differ for the values of the coefficients k_s, reported in Table 4.5. In each

Table 4.4: Performance of ELM model in cross-validation using different climate signals and 9 months lag time: SPEI forecasts.

Scenarios	Cor	R^2
MEI-9	0.92	0.84
PDO-9	0.86	0.74
AMO-9	0.84	0.70
MEI9-PDO9	0.84	0.71
MEI9-AMO9	0.78	0.61
PDO9-AMO9	0.76	0.57

strategy, however, lower values of k_s are assigned in case of wet conditions (positive SPEI), corresponding to more water impounded and less released. The rationale behind this decision is that when a wet season is forecasted, the water needs of downstream stakeholders will be sustained by abundant rain and lateral inflows. On the contrary, with a predicted upcoming drought, the water released downstream becomes a larger fraction of the inflow (larger k_s), in order to contain the combined impacts of drought and dam filling to downstream users. The horizon considered lasts from 2015 to 2017. Scenario 0 considers the historical filling release computed with Topkapi model developed by ETH university. The output of the simulation model are the Gibe III release, Gibe III water level and the lake Turkana water level. Figure 4.27 represents the different Gibe III release from 1 January 2015 to 30 October 2017. Scenario 0 starts with no release for the first year and in the following years the release is constant until it reaches of regime release conditions towards the end of the time horizon. The trajectories of the other scenarios follow the inflow pattern with a vertical variability due to the factor k_s. Figure 4.28 shows the Gibe III water level trajectories during the filling operations for the different scenarios, considering that the operation level is fixed to 201 m (*Velpuri and Senay*, 2012). It is evident how scenario 0 is designed for a fast filling reaching operations already in the first year given the initial null release, instead the other scenarios have a more gradual water level increment due to the significantly higher amount of water released during the filling process. Two of these scenarios do

Table 4.5: Gibe III filling strategies with different fraction k_s depending on SPEI index values.

Scenarios	k_1	k_2	k_3	k_4	k_5	k_6	k_7
SPEI $>$ 0	0.3	0.3	0.15	0.4	0.45	0.33	0.5
-0.5 $<$ SPEI $<$ 0	0.4	0.5	0.33	0.6	0.75	0.66	0.75
-1 $<$ SPEI $<$ -0.5	0.6	0.7	0.66	0.8	0.9	1	1
SPEI $<$ -1	0.8	0.9	1	1	1	1	1

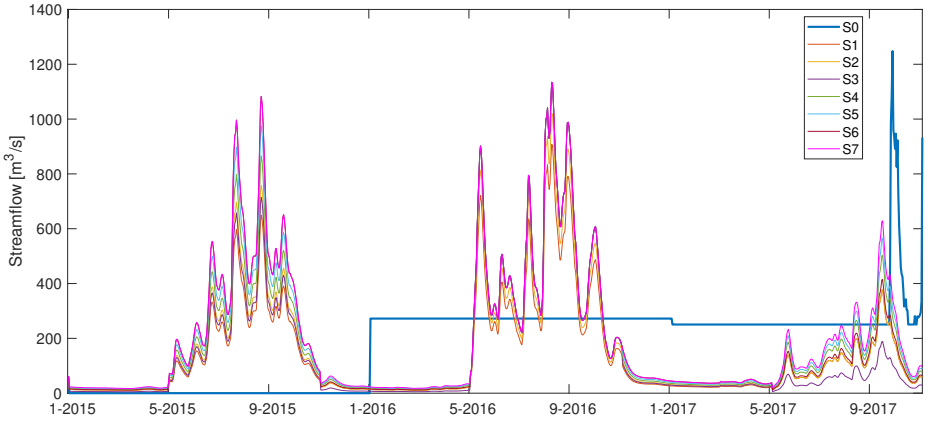

Figure 4.27: Gibe III releases for the different scenarios implemented from 1 Jan 2015 to 30 Oct 2017.

not reach the operation level by the end of the considered time horizon (S5 and S7).

Figure 4.29 represents lake Turkana water level during the horizon and shows how the Turkana water level is going to decrease with respect to natural conditions (obtained via simulation in a configuration without Gibe III reservoir) due to Gibe III filling operations. However, several of the identified filling strategies allow to reduce the impact on downstream areas. In particular, four scenarios (S4, S5, S6 and S7) have higher final water level respect to S0 because the dam releases are more abundant along the horizon period.

Based on the output obtained with the simulation model, four objectives and different indicators of hydrological alterations are calculated, as described in section 2.4. In Figure 4.30 the four objectives coupled with three important indicators of hydrological alteration are summerized in a parallel-axes plot where

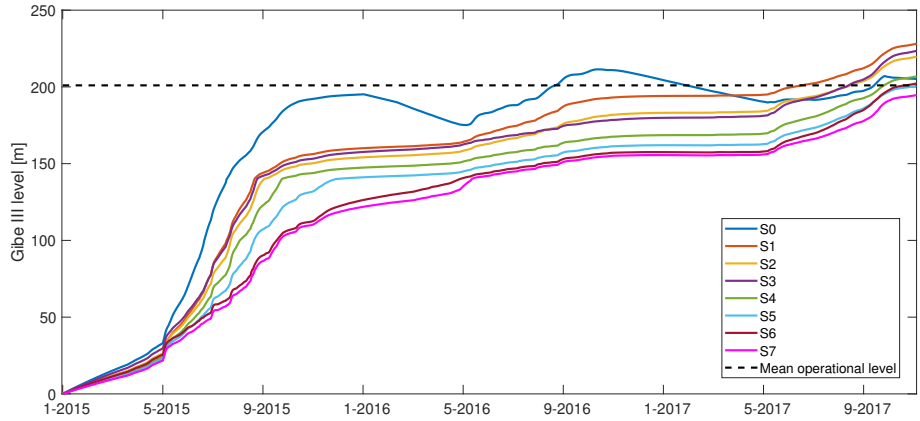

Figure 4.28: Gibe III water level for the different scenarios implemented from 1 Jan 2015 to 30 Oct 2017.

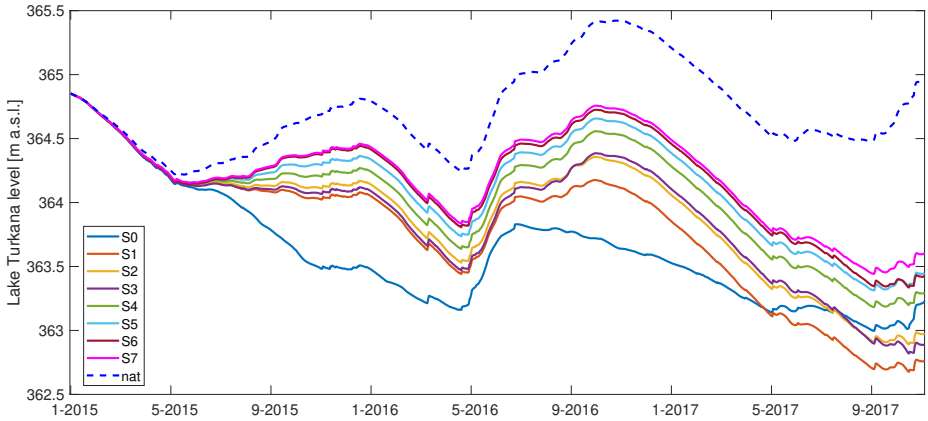

Figure 4.29: Lake Turkana water level for the different scenarios implemented from 1 Jan 2015 to 30 Oct 2017.

the indicators are normalized between their minimum and maximum values and 0 corresponds to the best indicator value.

The best solution focusing on lake Turkana is S7, that provides the minimum

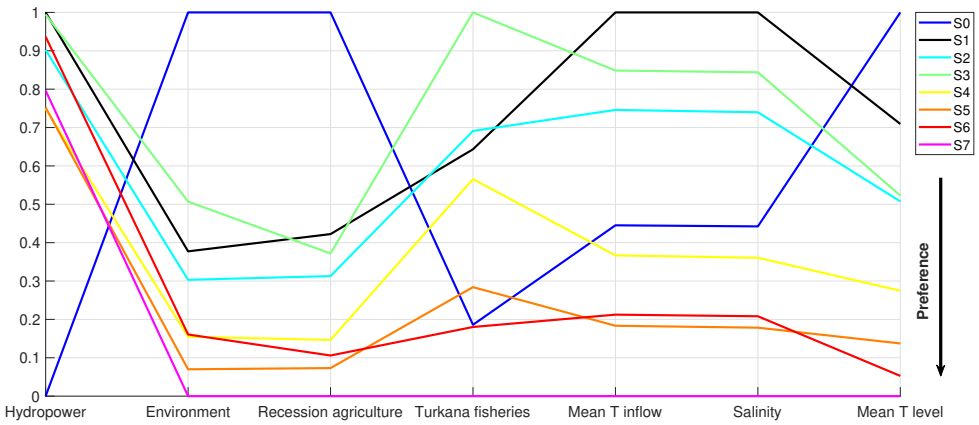

Figure 4.30: Parallel-axes plot representing the values of the 8 filling alternatives with respect to 7 performance indicators.

impacts on lake Turkana and on the downstream environment at the expence of hydropower. However, with this scenario the Gibe III operation level is not reached at the end of the horizon. If we consider as a constraint the reach of Gibe III operating level by October 2017, S5 seems a good compromise between downstream preservation and hydropower production.

5

Conclusions and future research

This study investigated the possibility of using drought forecast, based on the state of global teleconnections, to implement different reservoir filling strategies that take into account the state of water resources and the impacts of filling operations for the environment and economic activities downstream the dam. Reservoir filling strategies are a key planning aspect that did not receive much attention in the literature but hides a great potential to reduce dam impacts downstream. In our case study, the state of global teleconnections stongly influences the climate in terms of rainfall and streamflow, thus introducing a long-term predictability on hydrological fluctuations that can be exploited to design efficient filling operations taking into account the state of climate signals.

The Omo-Turkana basin is located in southern Ethiopia and northern Kenya, the basin is drained by Lake Turkana, with the Omo River on the Ethiopian side supplying 90% of the input to the lake. In the last decade, a massive hydroelectric power production project has been implemented with the costruction of several dams along the Omo river to exploit river hydropower potential. This man-made changes will cause transformations in river's regime and its input to Lake Turkana. While a wise operation of the new water infrastructures, which considers environmental and tribal needs, can be possible in regime conditions, the transient period related to dam filling is likely to provoke serious stakeholder conflicts and damages downstream providing the rational behind this thesis work.

In poorly gauged river basins characterized by a limited availability of in-situ

meteorological stations, satellite data constitute a valid resource to retrieve hydro-meteorological information. This thesis evaluates the performance of three precipitation remote sensing dataset (TRMM, CHIRPS and TAMSAT) and two temperature remote sensing datasets (MERRA-2 and ORH) in the Omo river basin corrected with mean bias-remove technique and linear scaling.
The selected and corrected precipitation dataset (TAMSAT) and temperature (MERRA-2) data are employed to compute two drought indexes: SPI and SPEI. The SPI and SPEI values are computed for six sub-basin areas which are selected with the objective to detect all the different conditions in terms of precipitation and temperature present inside the basin. The indicators were computed over 32 years for different cumulation periods: 1 month (related to meteorological drought), 3 months and 6 months (related to agricultural drought), 9 and 12 months (related to hydrological drought).
After defining the main local variables for the case study (precipitation and SPEI index), we employ the NIPA procedure to detect the relevant teleconnections in the area that will constitute the basis for our data driven middle and long term forecast (ELM model). The results show that the correlation between teleconnections and local varibles in the area is relevant, and that ELM models are able to use it for reliable forecasts. In particular the comparison between observations and resulting hindcast provides a Pearson coefficient Cor = 0.87 and the determination coefficient R^2 = 0.76 for precipitation, and for SPEI index we obtain Cor = 0.92 and R^2 = 0.84, both using Principal components of SST identified through from MEI index.
The conclusion we can draw from this analysis is that a clear correlation between teleconnections and local hydrological variables exist in the region and can inform water systems filling operations on upcoming dry or wet periods. The filling strategies that were implemented and tested are designed to respect natural seasonal inflow variability while accounting for the forecasted state of water resources and drought condition in the basin. The release decision from the dam are defined as a fraction of the inflow dependent on the forecasted SPEI index. These strategies are compared with the actual strategy employed for the filling of Gibe III in terms of hydropower production and several downstream interests. The results during the filling horizon highlight that several proposed strategies has the potential to significantly decrease downstream impacts during filling transient. In particular, we notice a huge improvement of lake Turkana condition in terms of water level, which during the considered horizon is maintained up to one meter higher for several strategies with respect to reference filling strategy.
We advocate that the analyis proposed is general, and case independent, and

can thus be applied to other reservoirs. For example, along the Omo river downstream Gibe III, another large reservoir, Koysha dam, is under construction since 2016, and according to the previsions will be completed and start to fill in 2021. The Koysha filling operations will cause a further drop of Turkana water level and it will be essential to reduce impacts on the lake Turkana.
In light of these results, further research could be conducted. Firstly, the current filling strategies are based on a fractional method and the fraction coefficients are fixed a priori trying to explore different scenarios. We can improve the filling performance including the optimization of fractional coefficients employing for example a multi objective evolutionary algorithm.
Finally, by extending the forecast lead time even further, it could be possible to define a favorable time to begin the filling operations, by shifting filling starting point from 2015 to a different years thus avoiding to exacerbate the impacts of the 2015-2016 drought with a filling transient.

Bibliography

Adams, E. (2017), Introduction on bias correction methods.

Ajaaj, A. A., A. K. Mishra, and A. A. Khan (2016), Comparison of bias correction techniques for gpcc rainfall data in semi-arid climate, *Stochastic environmental research and risk assessment*, *30*(6), 1659–1675.

Anghileri, D., A. Kaelin, N. Peleg, S. Fatichi, P. Molnar, C. Roques, L. Longuevergne, and P. Burlando (2017), Modeling the hydrological regime of turkana lake (kenya, ethiopia) by combining spatially distributed hydrological modeling and remote sensing datasets, in *AGU Fall Meeting Abstracts*.

Araghinejad, S., and E. Meidani (2013), A review of climate signals as predictors of long-term hydroclimatic variability, in *Climate Variability-Regional and Thematic Patterns*, InTech.

Araghinejad, S., D. H. Burn, and M. Karamouz (2006), Long-lead probabilistic forecasting of streamflow using ocean-atmospheric and hydrological predictors, *Water Resources Research*, *42*(3).

Avery, S. (2012), Lake turkana & the lower omo: hydrological impacts of major dam and irrigation developments, *African Studies Centre, the University of Oxford*.

Avery, S. (2013), What future for lake turkana? the impact of hydropower and irrigation development on the world,Äôs large desert lake, *African Studies Centre, University of Oxford*.

Awchi, I., and T. Abdul-Majeed (2004), Optimal planning and operation of a reservoir.

Becue, J.-P., G. Degoutte, and D. Lautrin (2002), Choice of site and type of dam, *Small Dams-Guidelines for Design, Construction and Monitoring*, pp. 17–22.

Belete, M. D., B. Diekkrüger, and J. Roehrig (2015), Characterization of water level variability of the main ethiopian rift valley lakes, *Hydrology*, *3*(1), 1.

Bizzi, S., F. Pianosi, and R. Soncini-Sessa (2012), Valuing hydrological alteration in multi-objective water resources management, *Journal of hydrology*, *472*, 277–286.

Block, P. (2011), Tailoring seasonal climate forecasts for hydropower operations, *Hydrology and Earth System Sciences*, *15*(4), 1355–1368.

Block, P., and L. Goddard (2011), Statistical and dynamical climate predictions to guide water resources in ethiopia, *Journal of Water Resources Planning and Management*, *138*(3), 287–298.

Block, P., and B. Rajagopalan (2007), Interannual variability and ensemble forecast of upper blue nile basin kiremt season precipitation, *Journal of Hydrometeorology*, *8*(3), 327–343.

Bloszies, C., and S. L. Forman (2015), Potential relation between equatorial sea surface temperatures and historic water level variability for lake turkana, kenya, *Journal of Hydrology*, *520*, 489–501.

Boulos, M. (2017), Social, economic and environmental impact of alternative scenarios of development in the omo river catchment.

Carr, C. J. (2017), *River Basin Development and Human Rights in Eastern Africa: A Policy Crossroads*, Springer.

Castelletti, A., F. Pianosi, and R. Soncini-Sessa (2008), Water reservoir control under economic, social and environmental constraints, *Automatica*, *44*(6), 1595–1607.

Castelletti, A., F. Pianosi, X. Quach, and R. Soncini-Sessa (2012), Assessing water reservoirs management and development in northern vietnam, *Hydrology and Earth System Sciences*, *16*(1), 189–199.

Castelletti, A., S. Bizzi, R. J. Schmitt, and G. Kondolf (2018), Improved trade-offs of hydropower and sand connectivity by strategic dam planning in the mekong, *Nature Sustainability*, *1*(2), 96.

Chang, N.-B., C. Wen, Y. Chen, and Y. Yong (1996), A grey fuzzy multiobjective programming approach for the optimal planning of a reservoir watershed. part a: Theoretical development, *Water Research*, *30*(10), 2329–2334.

Commission, N. P. (2015), The second growth and transformation plan (gtp ii)(2015/16-2019/20)(draft), *Addis Ababa: The Federal Democratic Republic of Ethiopia*.

Degefu, M. A., and W. Bewket (2017), Variability, trends, and teleconnections of stream flows with large-scale climate signals in the omo-ghibe river basin, ethiopia, *Environmental monitoring and assessment*, *189*(4), 142.

Degefu, M. A., D. P. Rowell, and W. Bewket (2017), Teleconnections between ethiopian rainfall variability and global ssts: observations and methods for model evaluation, *Meteorology and Atmospheric Physics*, *129*(2), 173–186.

Deltares (2010), Reservoir planning, design and operation.

Diro, G., D. I. F. Grimes, and E. Black (2011), Teleconnections between ethiopian summer rainfall and sea surface temperature: part i,Äîobservation and modelling, *Climate Dynamics*, *37*(1-2), 103–119.

Enfield, D. B., A. M. Mestas-Nuñez, and P. J. Trimble (2001), The atlantic multidecadal oscillation and its relation to rainfall and river flows in the continental us, *Geophysical Research Letters*, *28*(10), 2077–2080.

Fang, G., J. Yang, Y. Chen, and C. Zammit (2015), Comparing bias correction methods in downscaling meteorological variables for a hydrologic impact study in an arid area in china, *Hydrology and Earth System Sciences*, *19*(6), 2547–2559.

Funk, C., et al. (2015), The climate hazards infrared precipitation with stations,Äîa new environmental record for monitoring extremes, *Scientific data*, *2*, 150,066.

Gebrechorkos, S. H., S. Hülsmann, and C. Bernhofer (2018), Evaluation of multiple climate data sources for managing environmental resources in east africa, *Hydrology and Earth System Sciences*, *22*(8), 4547–4564.

Gelaro, R., et al. (2017), The modern-era retrospective analysis for research and applications, version 2 (merra-2), *Journal of Climate*, *30*(14), 5419–5454.

Gentile, A. (2018), Informing water reservoir operations with climate teleconnections.

Gownaris, N. J., et al. (2017), Fisheries and water level fluctuations in the world's largest desert lake, *Ecohydrology*, *10*(1), e1769.

Grantz, K., B. Rajagopalan, M. Clark, and E. Zagona (2005), A technique for incorporating large-scale climate information in basin-scale ensemble streamflow forecasts, *Water Resources Research*, *41*(10).

Hanley, D. E., M. A. Bourassa, J. J. O'Brien, S. R. Smith, and E. R. Spade (2003), A quantitative evaluation of ENSO indices, *Journal of Climate*, *16*(8), 1249–1258.

Hao, Z., V. P. Singh, and Y. Xia (2018), Seasonal drought prediction: advances, challenges, and future prospects, *Reviews of Geophysics*, *56*(1), 108–141.

Huang, G.-B., Q.-Y. Zhu, and C.-K. Siew (2006), Extreme learning machine: theory and applications, *Neurocomputing*, *70*(1-3), 489–501.

Huffman, G. J., D. T. Bolvin, E. J. Nelkin, D. B. Wolff, R. F. Adler, G. Gu, Y. Hong, K. P. Bowman, and E. F. Stocker (2007), The TRMM multisatellite precipitation analysis (tmpa): Quasi-global, multiyear, combined-sensor precipitation estimates at fine scales, *Journal of hydrometeorology*, *8*(1), 38–55.

Hurrell, J. W., Y. Kushnir, G. Ottersen, and M. Visbeck (2003), An overview of the north atlantic oscillation, *The North Atlantic Oscillation: climatic significance and environmental impact*, *134*, 1–35.

InternationalRivers (2013), The downstream impacts of ethiopia's gibe III dam. east africa's 'aral sea' in the making?

King, A., and P. Block (2014), An assessment of reservoir filling policies for the grand ethiopian renaissance dam, *Journal of Water and Climate Change*, *5*(2), 233–243.

Labadie, J. W. (2004), Optimal operation of multireservoir systems: state-of-the-art review, *Journal of water resources planning and management*, *130*(2), 93–111.

Lavers, D., C. Prudhomme, and D. M. Hannah (2013), European precipitation connections with large-scale mean sea-level pressure (mslp) fields, *Hydrological sciences journal*, *58*(2), 310–327.

Ledec, G., and J. D. Quintero (2003), Good dams and bad dams: Environmental criteria for site selection of hydroelectric projects.

Liersch, S., H. Koch, and F. F. Hattermann (2017), Management scenarios of the grand ethiopian renaissance dam and their impacts under recent and future climates, *Water*, *9*(10), 728.

Maidment, R. I., et al. (2017), A new, long-term daily satellite-based rainfall dataset for operational monitoring in africa, *Scientific data*, *4*, 170,063.

Mantua, N. J., and S. R. Hare (2002), The pacific decadal oscillation, *Journal of oceanography*, *58*(1), 35–44.

McCartney, M. P., and J. King (2011), Use of decision support systems to improve dam planning and dam operation in africa.

McKee, T. B., N. J. Doesken, J. Kleist, et al. (1993), The relationship of drought frequency and duration to time scales, in *Proceedings of the 8th Conference on Applied Climatology*, vol. 17, pp. 179–183, American Meteorological Society Boston, MA.

Mishra, A. K., and V. P. Singh (2010), A review of drought concepts, *Journal of hydrology*, *391*(1-2), 202–216.

M'Po, Y., A. E. Lawin, G. T. Oyerinde, B. K. Yao, and A. A. Afouda (2016), Comparison of daily precipitation bias correction methods based on four regional climate model outputs in ouémé basin, benin, *Hydrology*, *4*(6), 58–71.

NOAA (2018), Teleconnections introduction, http://www.cpc.ncep.noaa.gov/data/teledoc/teleintro.shtml.

O,ÄôReilly, C. H., T. Woollings, and L. Zanna (2017), The dynamical influence of the atlantic multidecadal oscillation on continental climate, *Journal of Climate*, *30*(18), 7213–7230.

Palmer, W. C. (1965), Meteorological drought, *US Weather Bureau research paper*, (45).

Penso, V. (2018), Discovering large-scale climate signals for seasonal meteorological forecasts in africa.

Poveda, G., and O. J. Mesa (1997), Feedbacks between hydrological processes in tropical south america and large-scale ocean–atmospheric phenomena, *Journal of climate*, *10*(10), 2690–2702.

Richter, B. D., J. V. Baumgartner, J. Powell, and D. P. Braun (1996), A method for assessing hydrologic alteration within ecosystems, *Conservation biology*, *10*(4), 1163–1174.

Saji, N., and T. Yamagata (2003), Possible impacts of indian ocean dipole mode events on global climate, *Climate Research*, *25*(2), 151–169.

Samale, C., B. Zimmerman, M. Giuliani, A. Castelletti, and P. Block (2017), Improving seasonal forecast through the state of large-scale climate signals, in *EGU General Assembly Conference Abstracts*, vol. 19, p. 12779.

SOGREAH (2010), Gibe III hydropower project. independent review and studies regarding the environmental & social impact assessments for the gibe III hydropower project.

Spinoni, J., G. Naumann, J. V. Vogt, and P. M. F. Barbosa (2016), Meteorological droughts in europe: events and impacts - past trends and future projections.

Velpuri, N. M., and G. Senay (2012), Assessing the potential hydrological impact of the gibe III dam on lake turkana water level using multi-source satellite data, *Hydrology and Earth System Sciences*, *16*(10), 3561–3578.

Vicente-Serrano, S. M., S. Beguería, and J. I. López-Moreno (2010), A multiscalar drought index sensitive to global warming: the standardized precipitation evapotranspiration index, *Journal of climate*, *23*(7), 1696–1718.

Wang, S., J. Huang, Y. He, and Y. Guan (2014), Combined effects of the pacific decadal oscillation and el nino-southern oscillation on global land dry–wet changes, *Scientific reports*, *4*, srep06,651.

Ward, P. J., B. Jongman, M. Kummu, M. D. Dettinger, F. C. S. Weiland, and H. C. Winsemius (2014), Strong influence of el niño southern oscillation on flood risk around the world, *Proceedings of the National Academy of Sciences*, *111*(44), 15,659–15,664.

Wheeler, K. G., M. Basheer, Z. T. Mekonnen, S. O. Eltoum, A. Mersha, G. M. Abdo, E. A. Zagona, J. W. Hall, and S. J. Dadson (2016), Cooperative filling approaches for the grand ethiopian renaissance dam, *Water international*, *41*(4), 611–634.

Williams, C., and N. Hanan (2011), Enso and iod teleconnections for african ecosystems: evidence of destructive interference between climate oscillations, *Biogeosciences*, *8*(1), 27–40.

Wolde-Georgis, T. (1997), El nino and drought early warning in ethiopia.

Zaniolo, M. (2017), Design and application of drought indexes in highly regulated mediterranean water systems.

Zargar, A., R. Sadiq, B. Naser, and F. I. Khan (2011), A review of drought indices, *Environmental Reviews*, *19*(NA), 333–349.

Zhang, Y., S. T. Erkyihum, and P. Block (2016), Filling the GERD: evaluating hydroclimatic variability and impoundment strategies for blue nile riparian countries, *Water international*, *41*(4), 593–610.

Zimmerman, B. G., D. J. Vimont, and P. J. Block (2016), Utilizing the state of ENSO as a means for season-ahead predictor selection, *Water resources research*, *52*(5), 3761–3774.

A

Additional material

A.1 Climate data processing

A.1.1 Bias correction - Precipitation

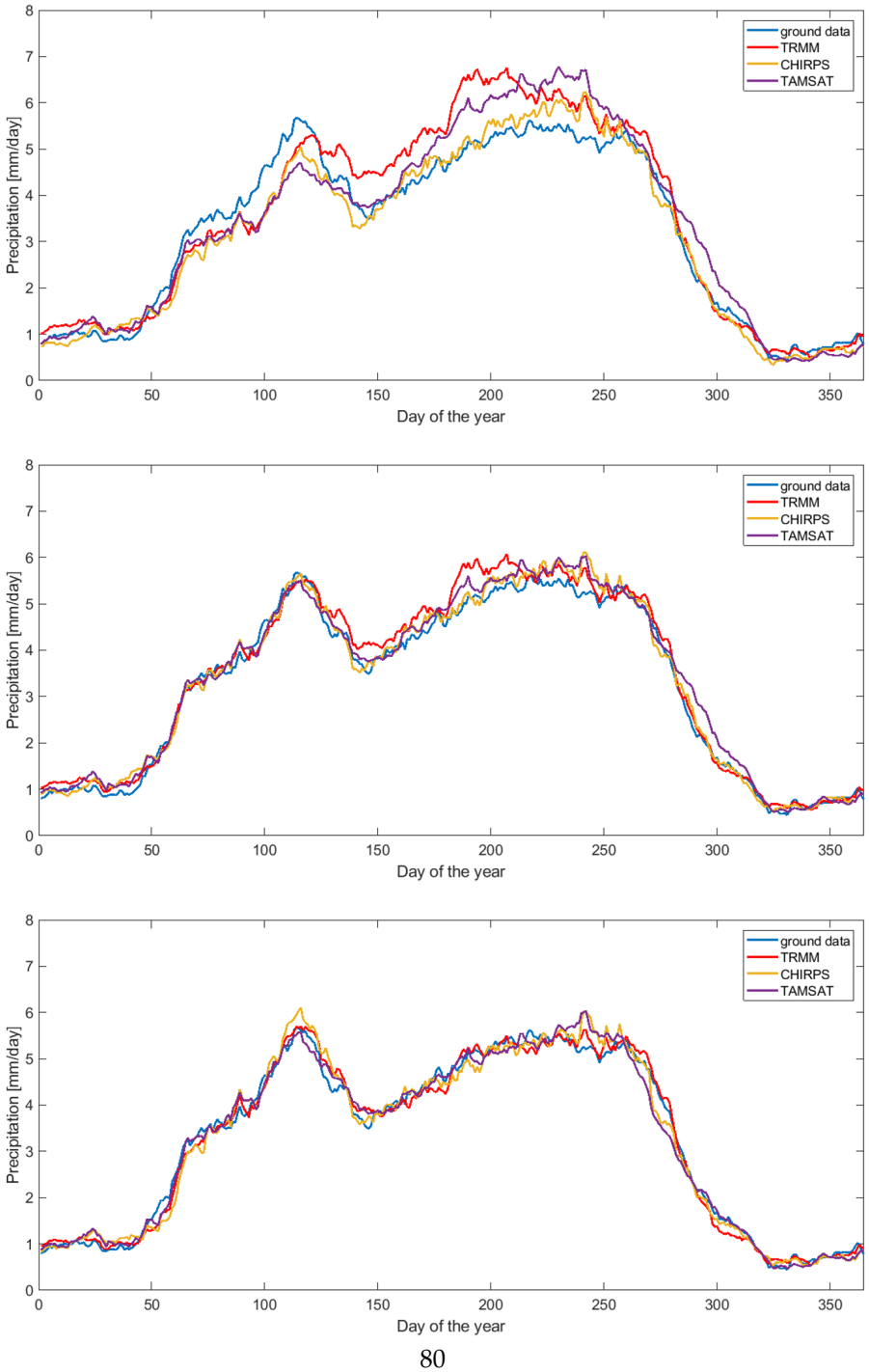

Figure A.1: Seasonal rainfall at Hosana station comparing in-situ data with remote sensing measurments: raw data (top), corrected with mean bias-remove technique (center), corrected with linear scaling technique (bottom).

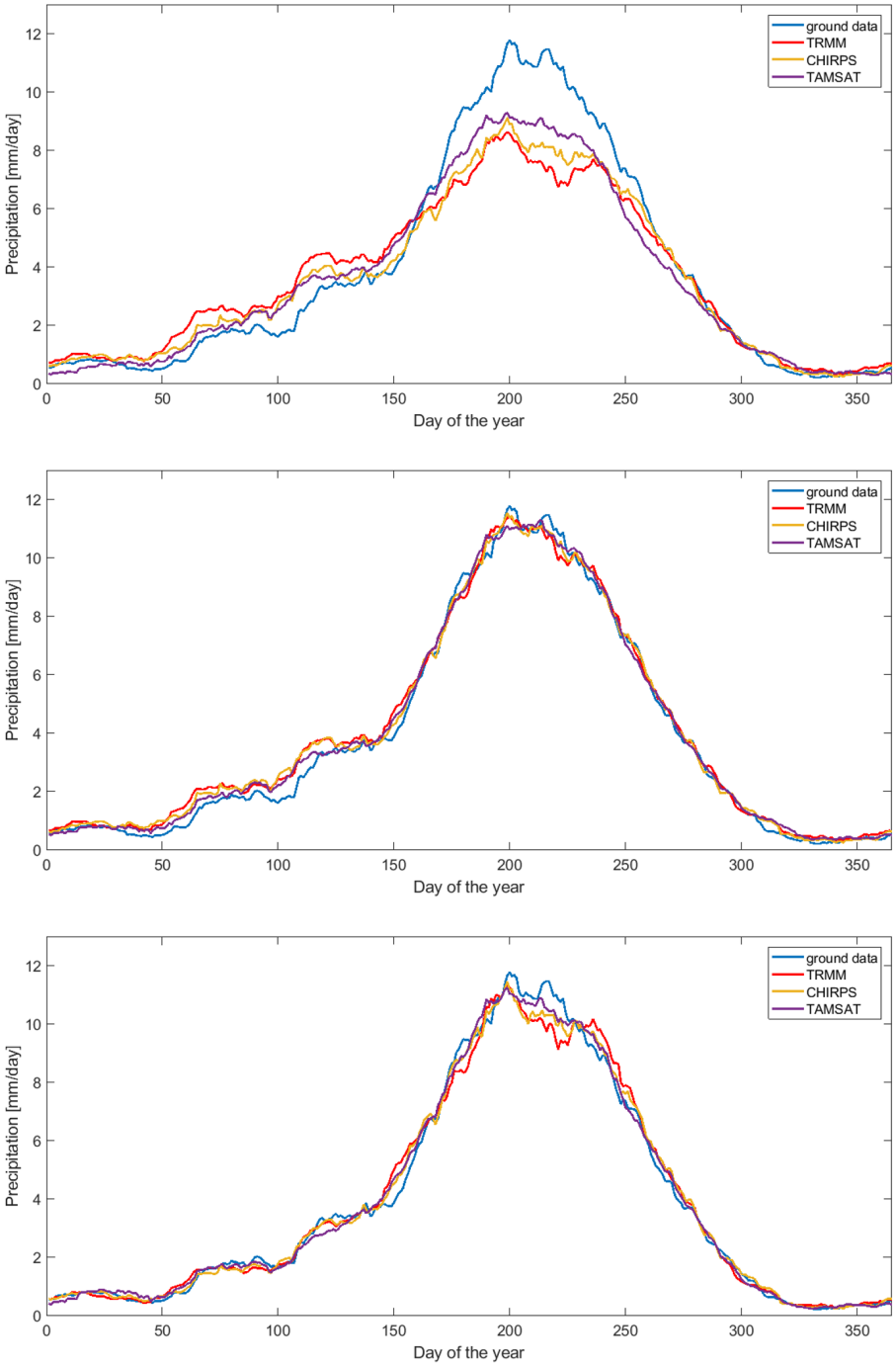

Figure A.2: Seasonal rainfall at Gubre station comparing in-situ data with remote sensing measurments: raw data (top), corrected with mean bias-remove technique (center), corrected with linear scaling technique (bottom).

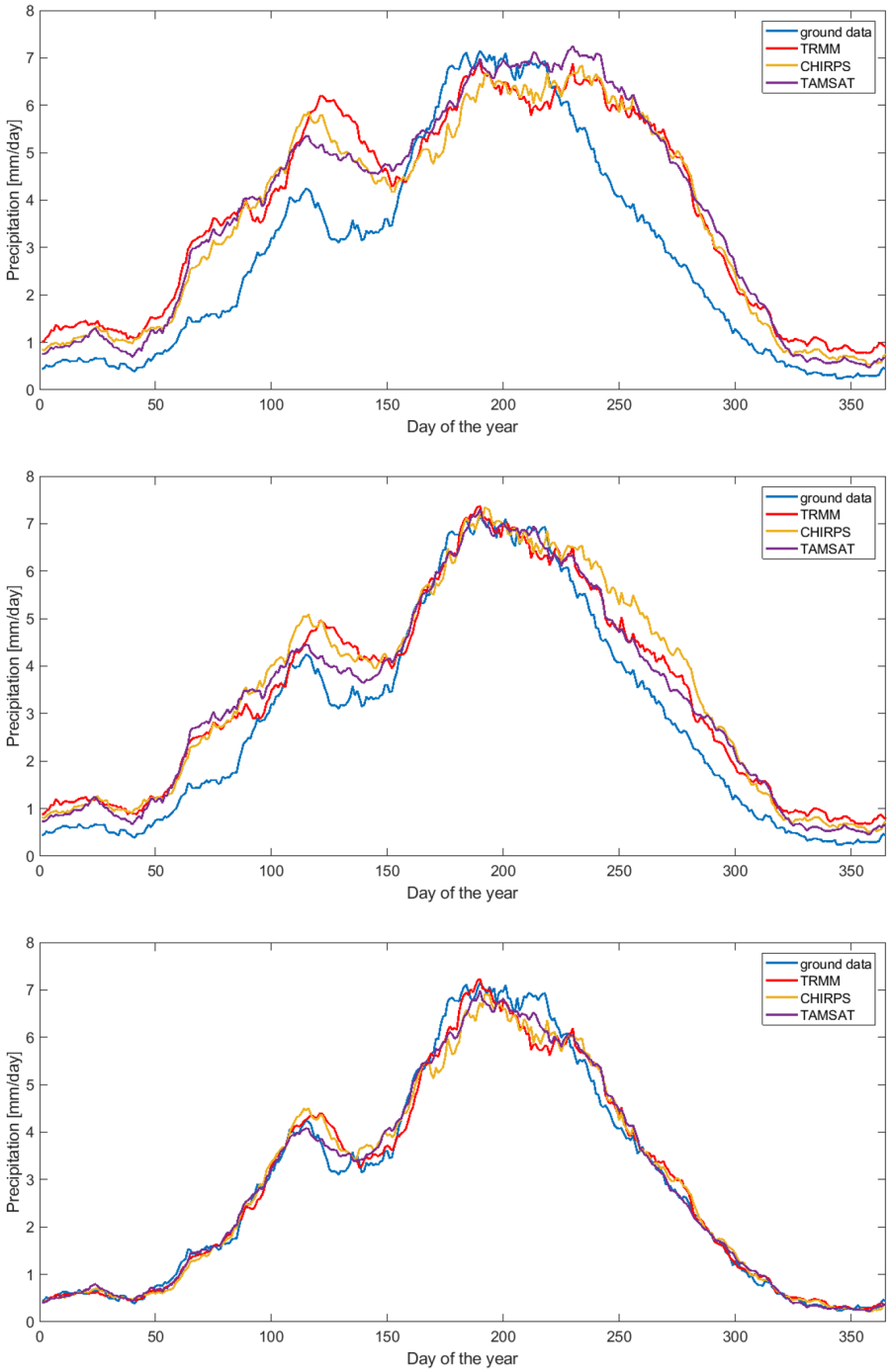

Figure A.3: Seasonal rainfall at Yaya Otena station comparing in-situ data with remote sensing measurments: raw data (top), corrected with mean bias-remove technique (center), corrected with linear scaling technique (bottom).

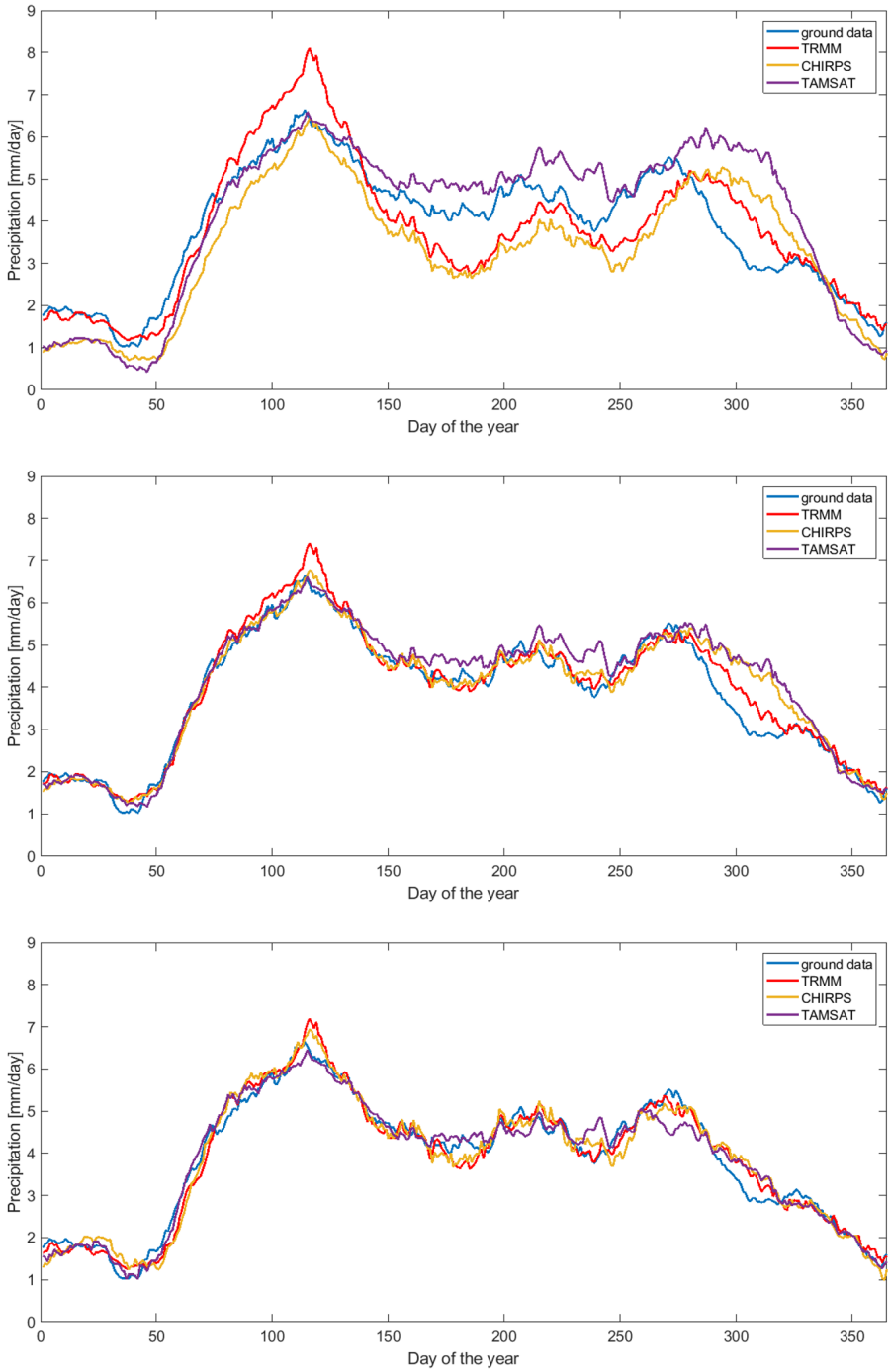

Figure A.4: Seasonal rainfall at Laske station comparing in-situ data with remote sensing measurments: raw data (top), corrected with mean bias-remove technique (center), corrected with linear scaling technique (bottom).

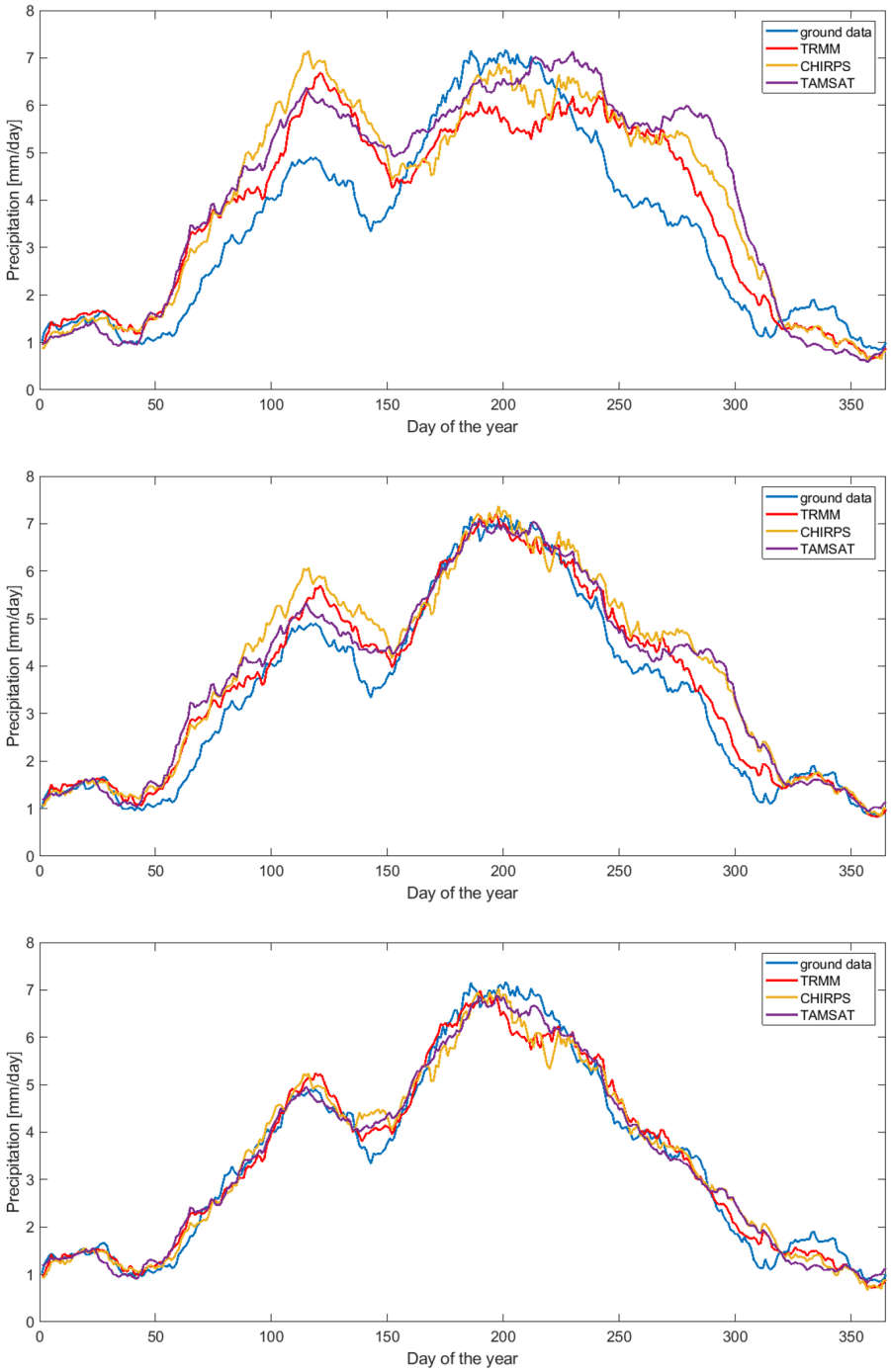

Figure A.5: Seasonal rainfall at Bele station comparing in-situ data with remote sensing measurments: raw data (top), corrected with mean bias-remove technique (center), corrected with linear scaling technique (bottom).

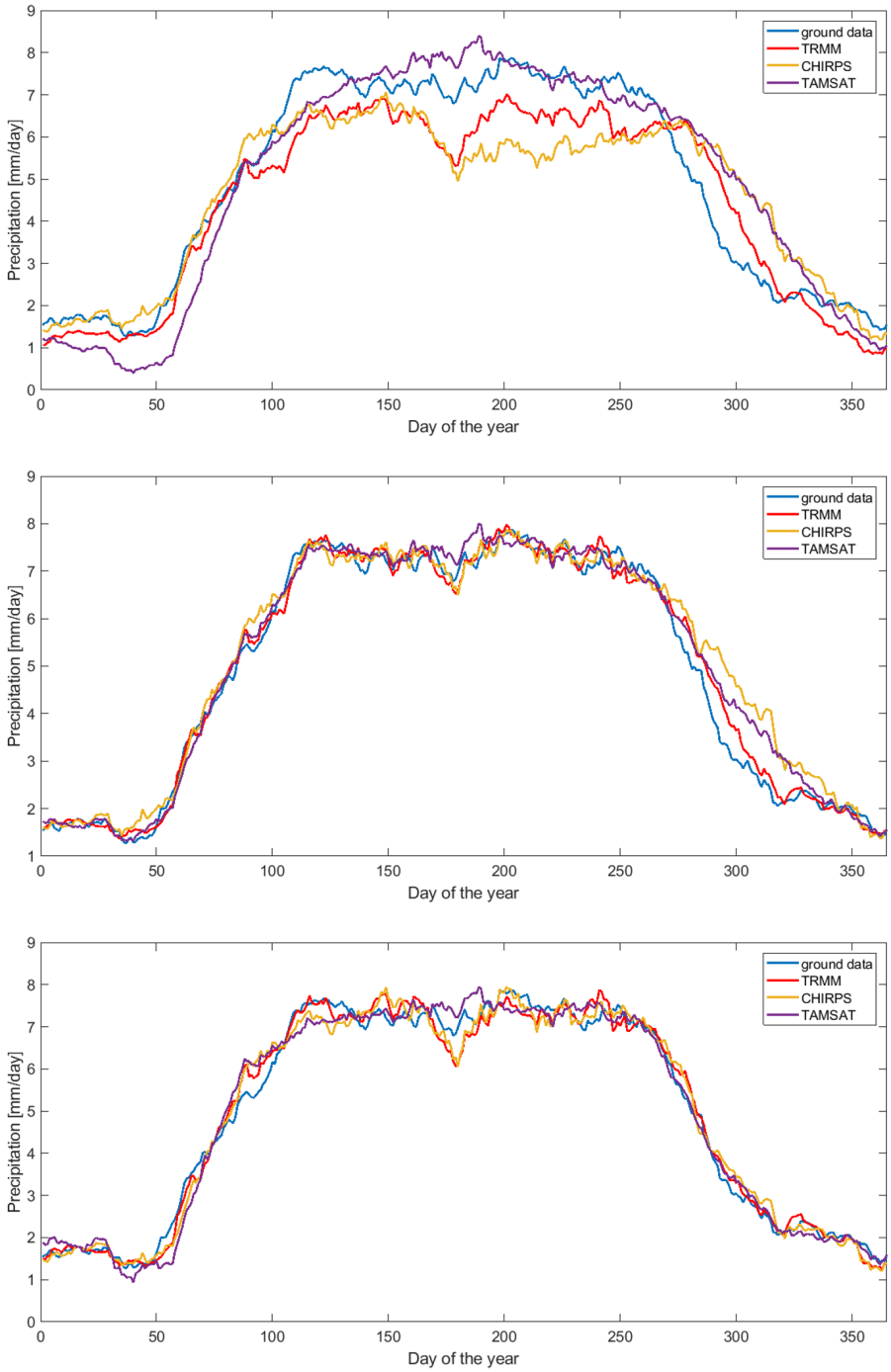

Figure A.6: Seasonal rainfall at Bonga station comparing in-situ data with remote sensing measurments: raw data (top), corrected with mean bias-remove technique (center), corrected with linear scaling technique (bottom).

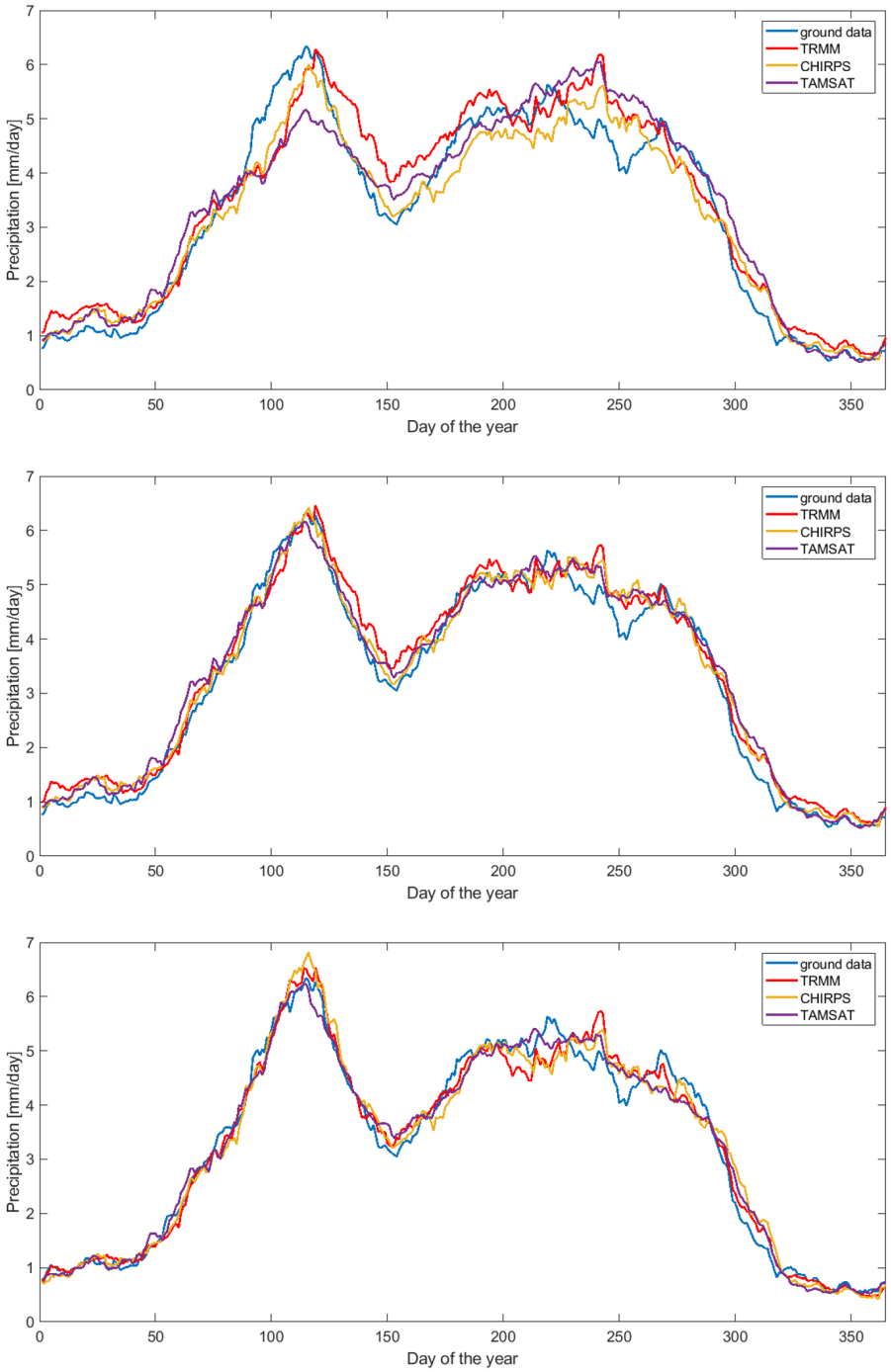

Figure A.7: Seasonal rainfall at Durame station comparing in-situ data with remote sensing measurments: raw data (top), corrected with mean bias-remove technique (center), corrected with linear scaling technique (bottom).

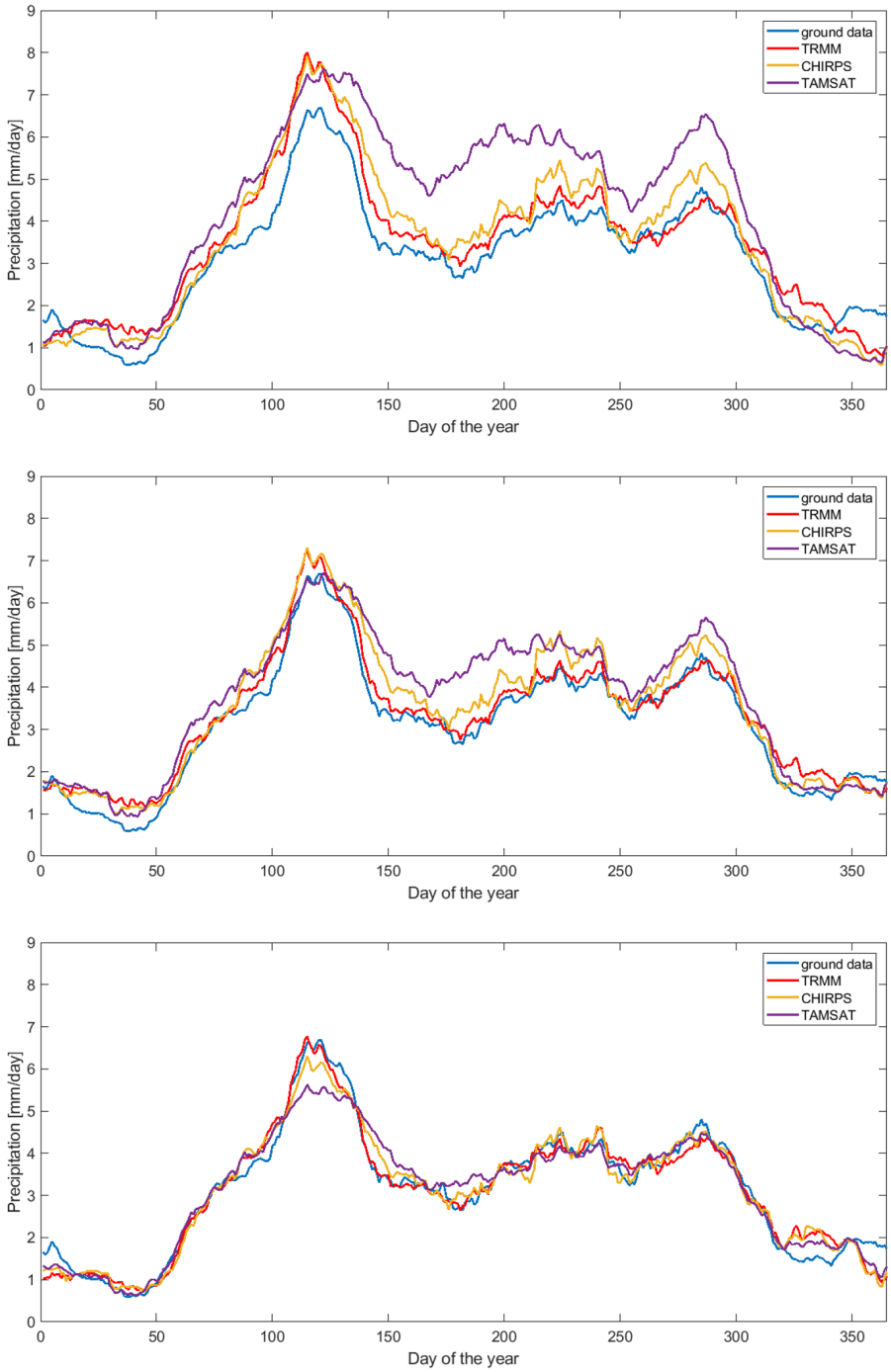

Figure A.8: Seasonal rainfall at Morka station comparing in-situ data with remote sensing measurments: raw data (top), corrected with mean bias-remove technique (center), corrected with linear scaling technique (bottom).

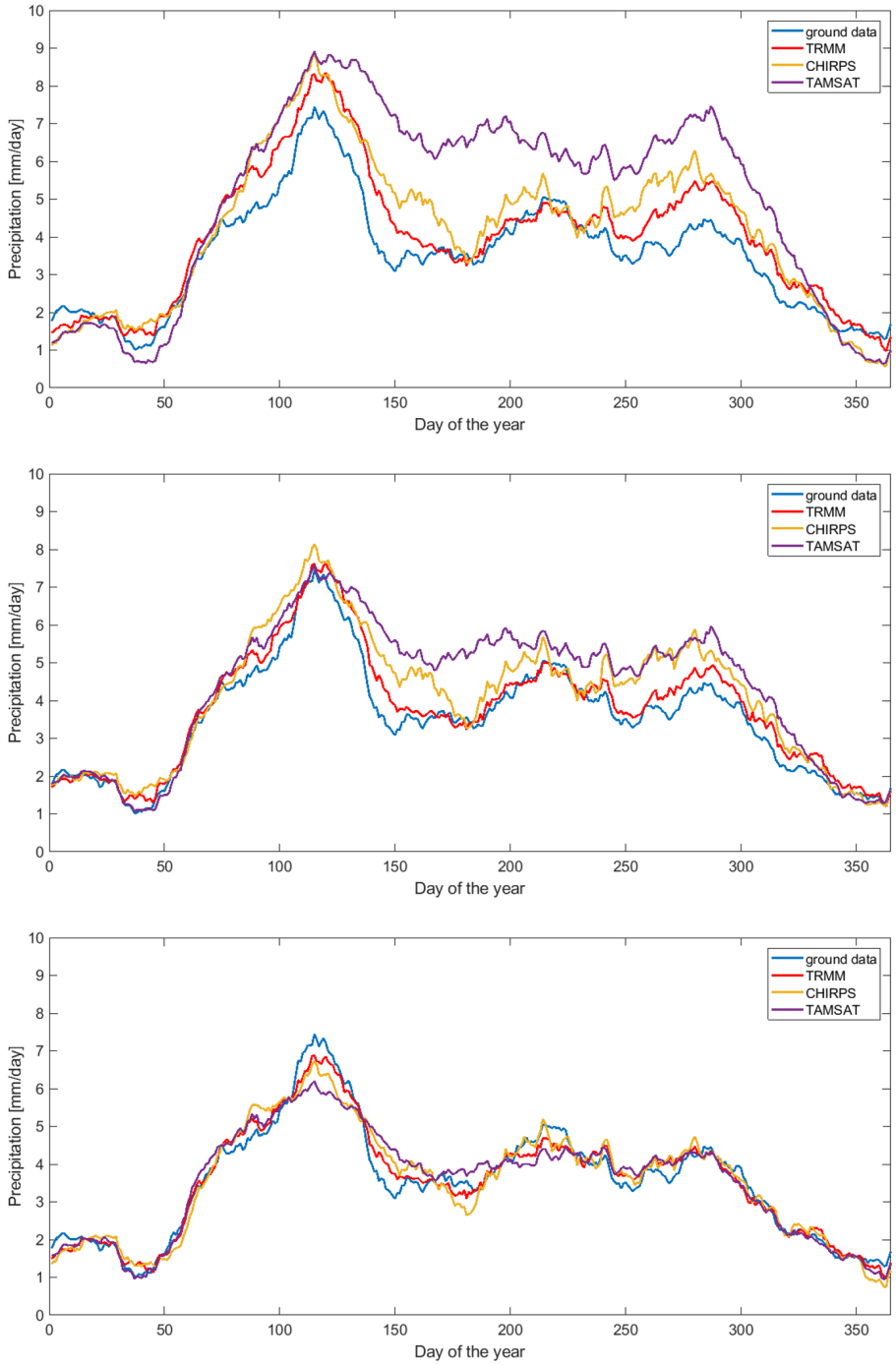

Figure A.9: Seasonal rainfall at Sawla station comparing in-situ data with remote sensing measurments: raw data (top), corrected with mean bias-remove technique (center), corrected with linear scaling technique (bottom).

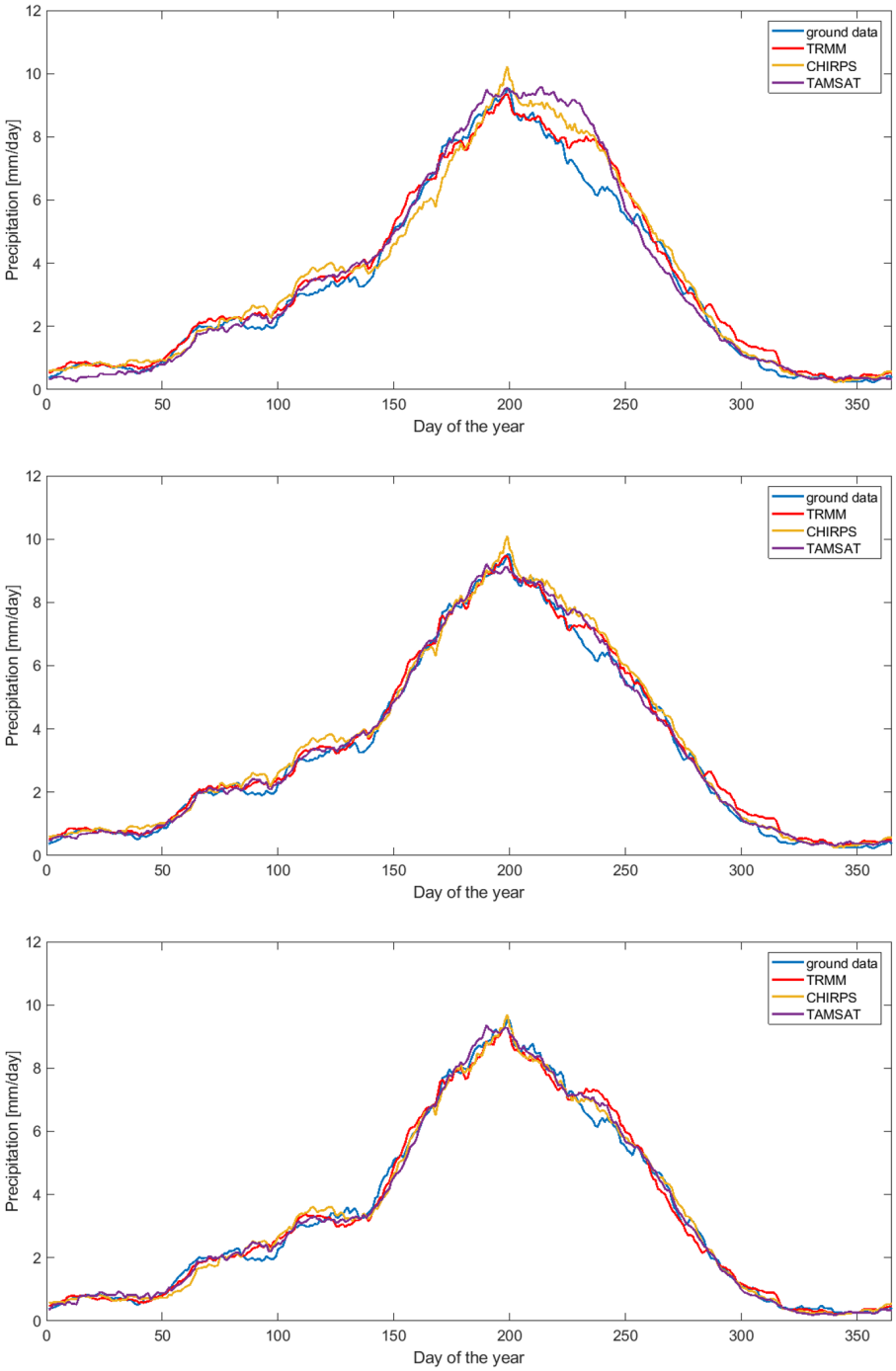

Figure A.10: Seasonal rainfall at Wolkite station comparing in-situ data with remote sensing measurments: raw data (top), corrected with mean bias-remove technique (center), corrected with linear scaling technique (bottom).

A.1.2 Bias correction - Temperature

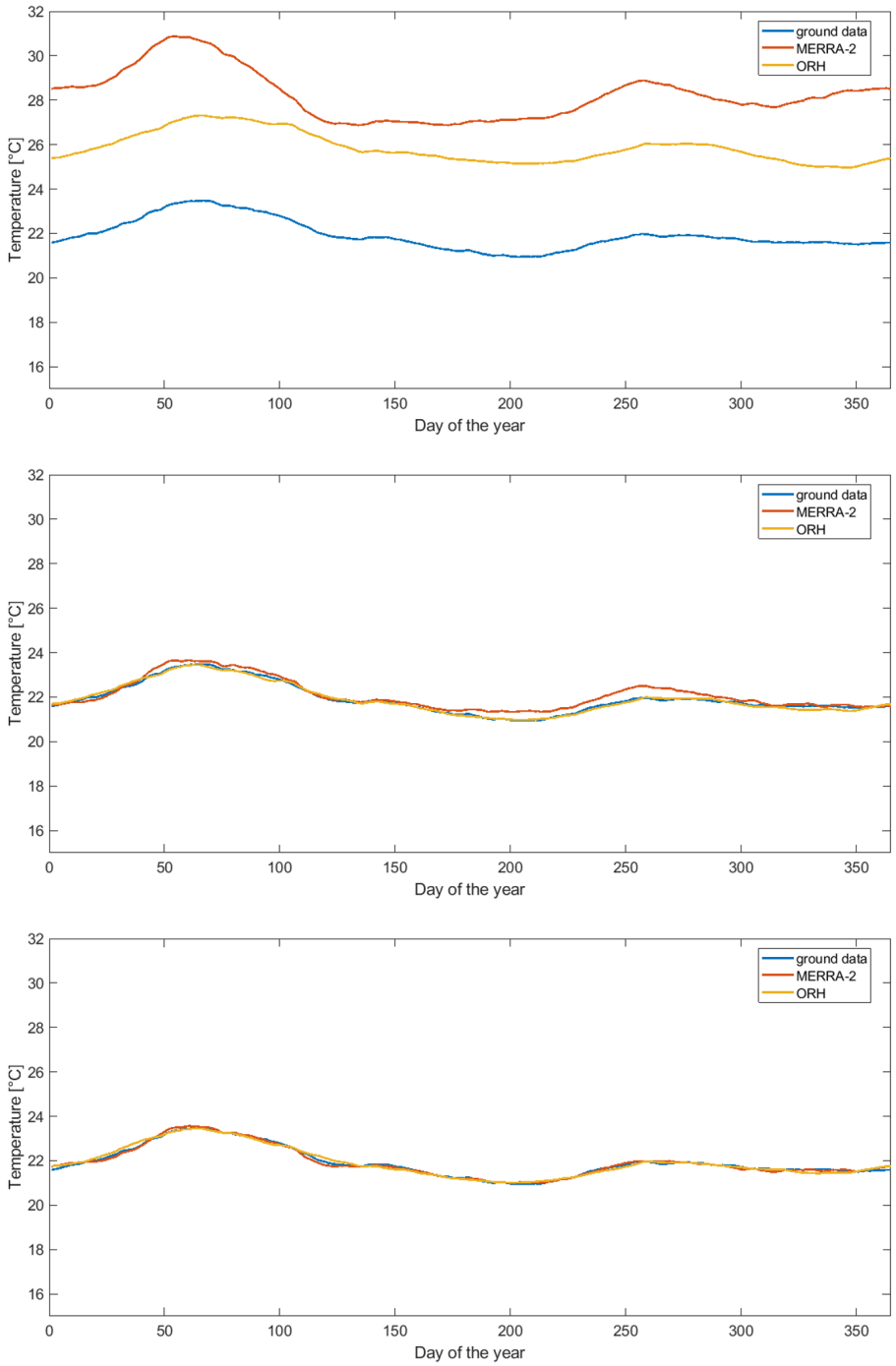

Figure A.11: Seasonal temperature at Jinka station comparing in-situ data with remote sensing measurments: raw data (top), corrected with mean bias-remove technique (center), corrected with linear scaling technique (bottom).

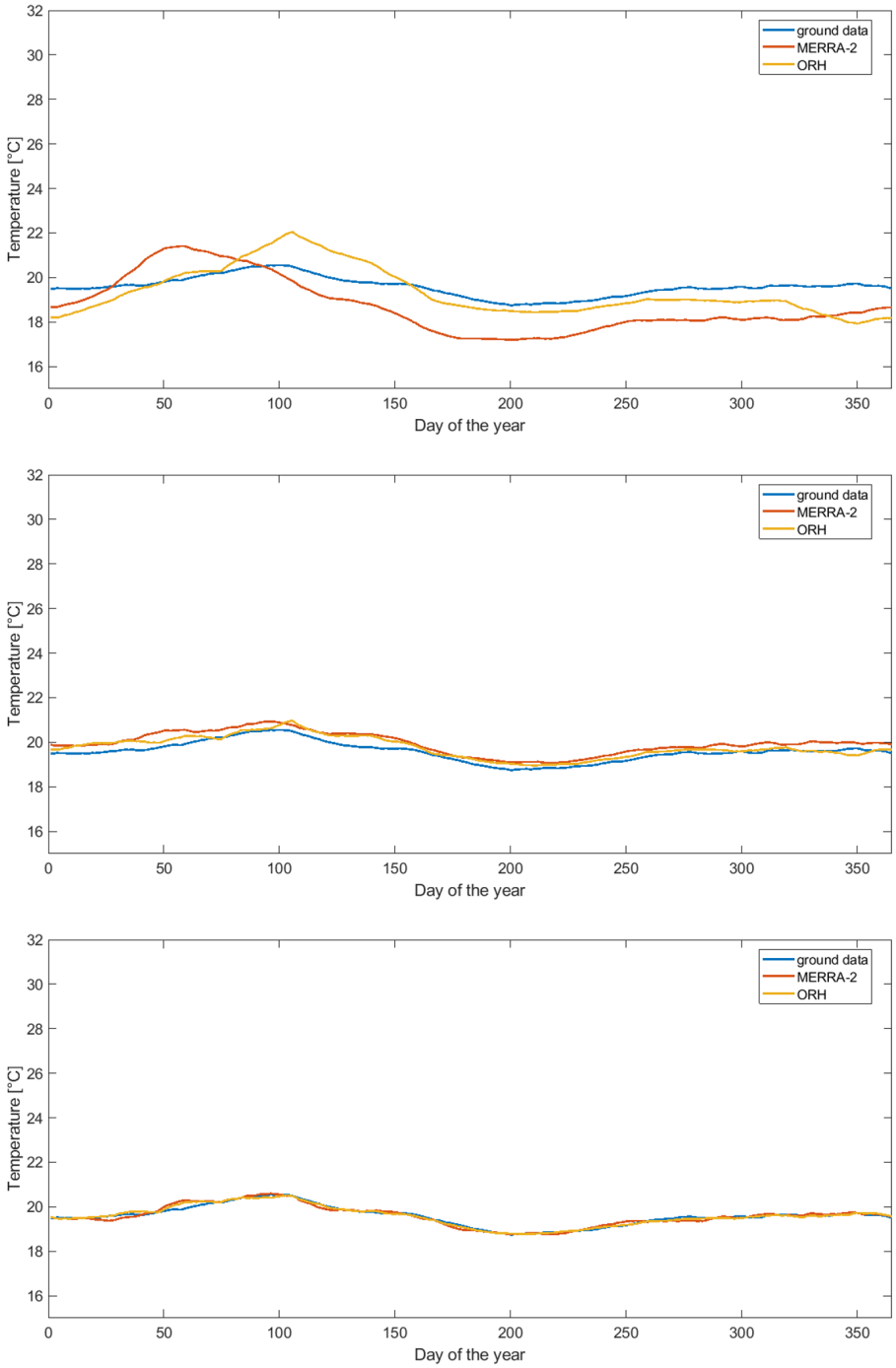

Figure A.12: Seasonal temperature at Bonga station comparing in-situ data with remote sensing measurments: raw data (top), corrected with mean bias-remove technique (center), corrected with linear scaling technique (bottom).

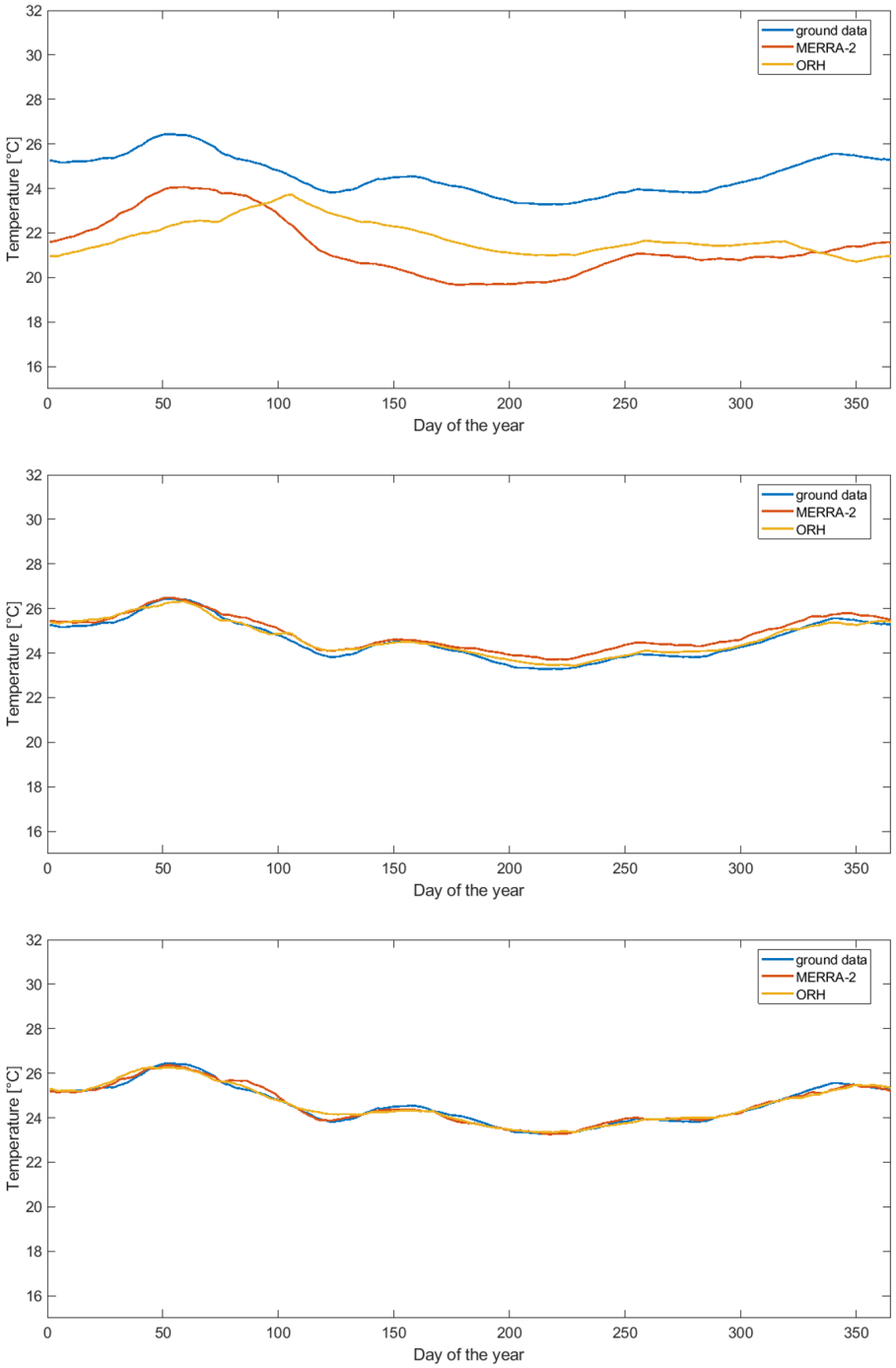

Figure A.13: Seasonal temperature at Morka station comparing in-situ data with remote sensing measurments: raw data (top), corrected with mean bias-remove technique (center), corrected with linear scaling technique (bottom).

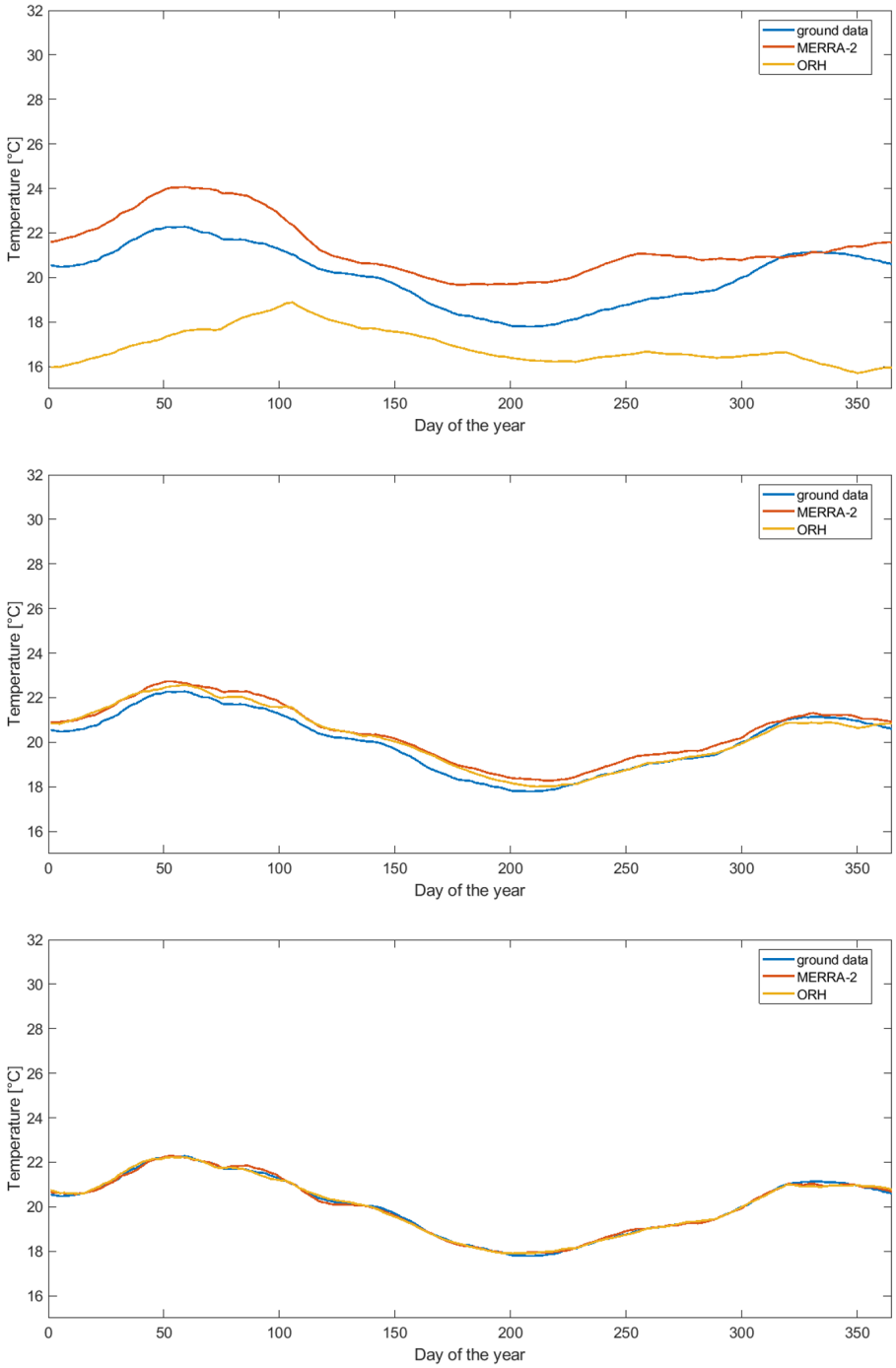

Figure A.14: Seasonal temperature at Wolaita Sodo station comparing in-situ data with remote sensing measurments: raw data (top), corrected with mean bias-remove technique (center), corrected with linear scaling technique (bottom).

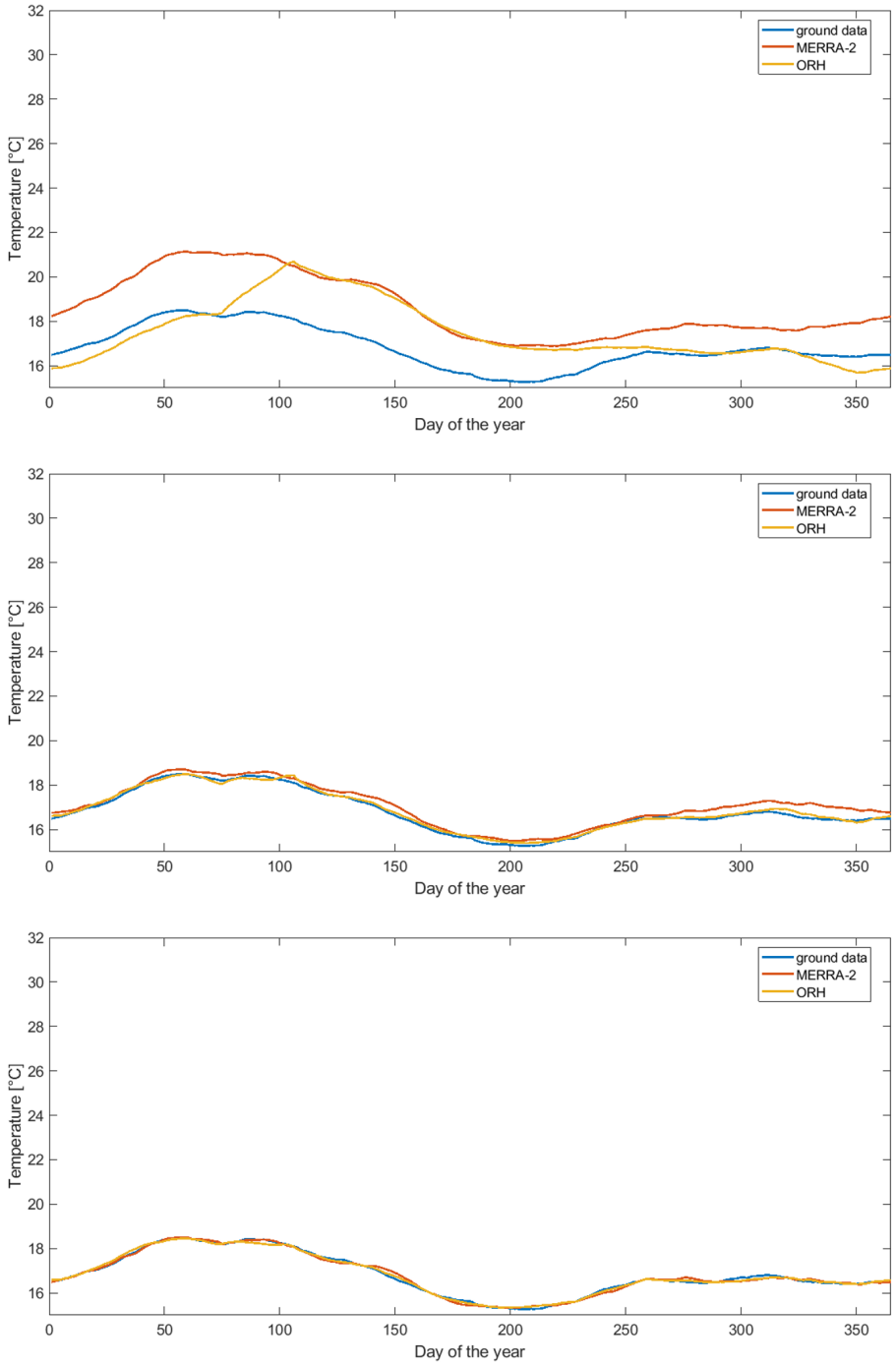

Figure A.15: Seasonal temperature at Hosana station comparing in-situ data with remote sensing measurments: raw data (top), corrected with mean bias-remove technique (center), corrected with linear scaling technique (bottom).

A.2 Seasonal forecast identification

A.2.1 Detection of relevant climate signals (NIPA)

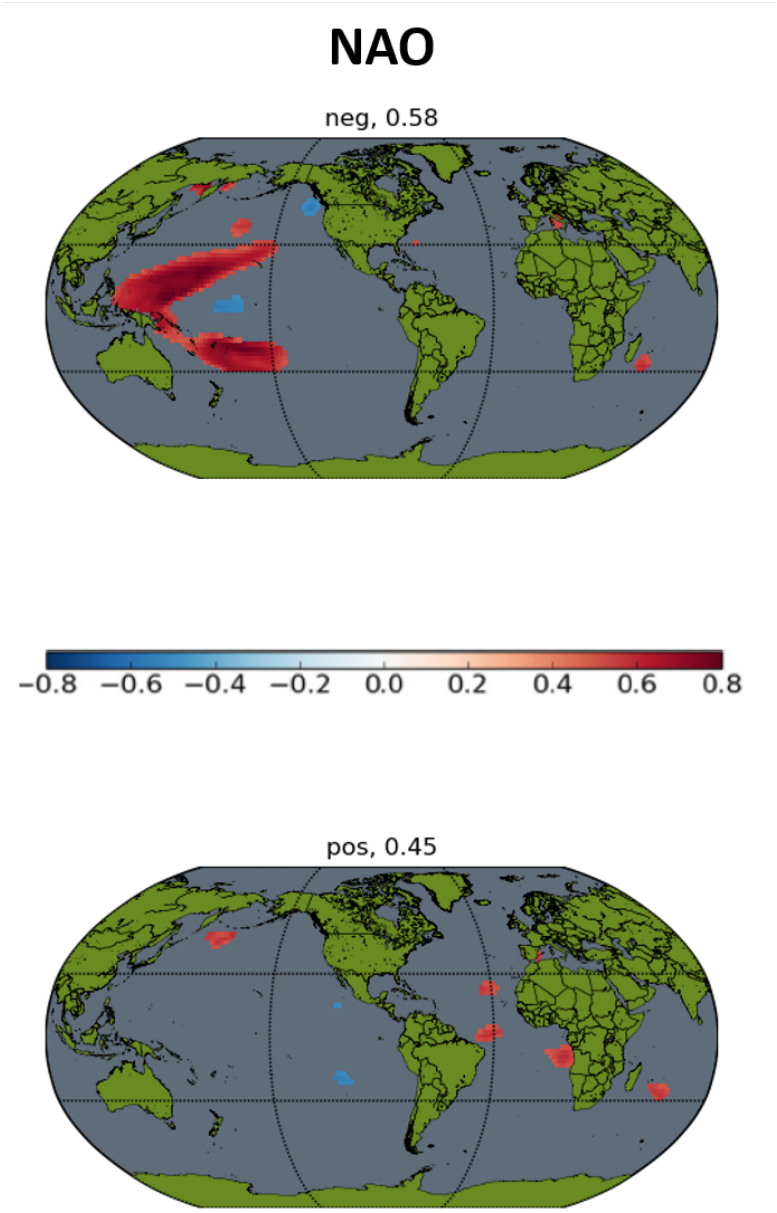

Figure A.16: Correlation maps between FMAM SST gridded anomalies and JJAS observed precipitation, generated by binning the years through NAO index.

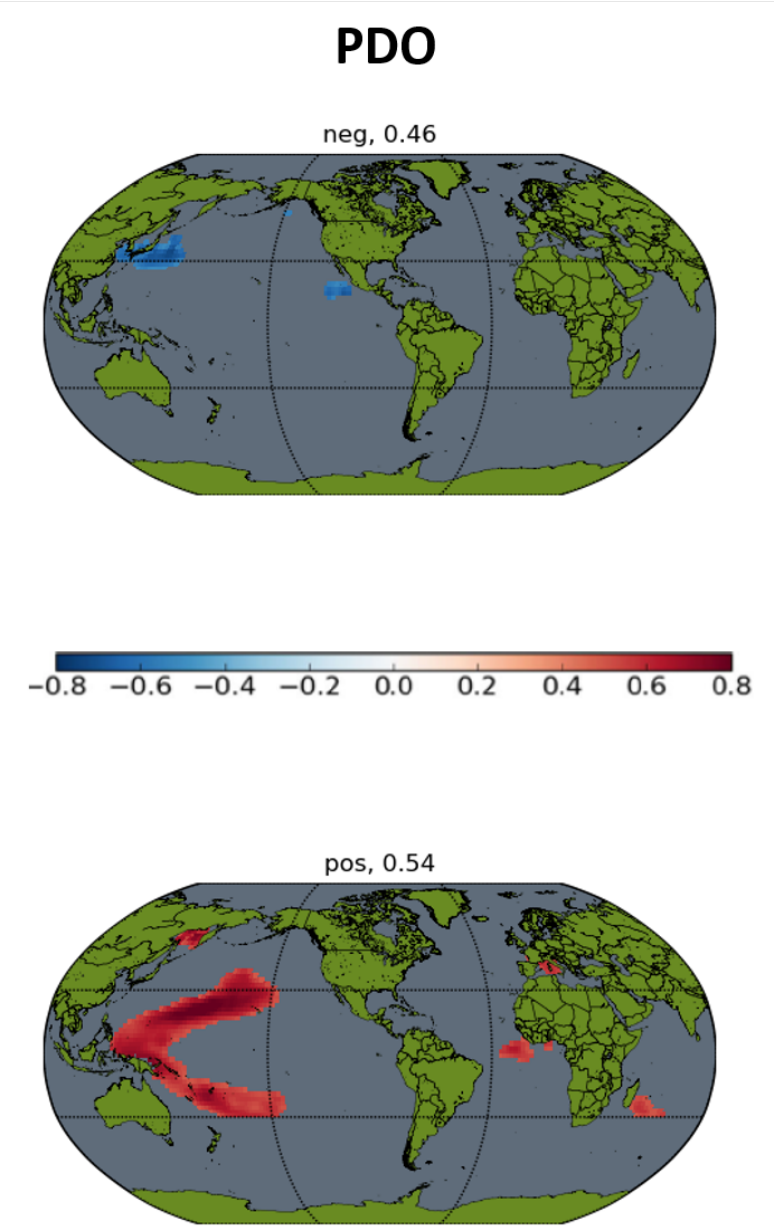

Figure A.17: Correlation maps between FMAM SST gridded anomalies and JJAS observed precipitation, generated by binning the years through PDO index.

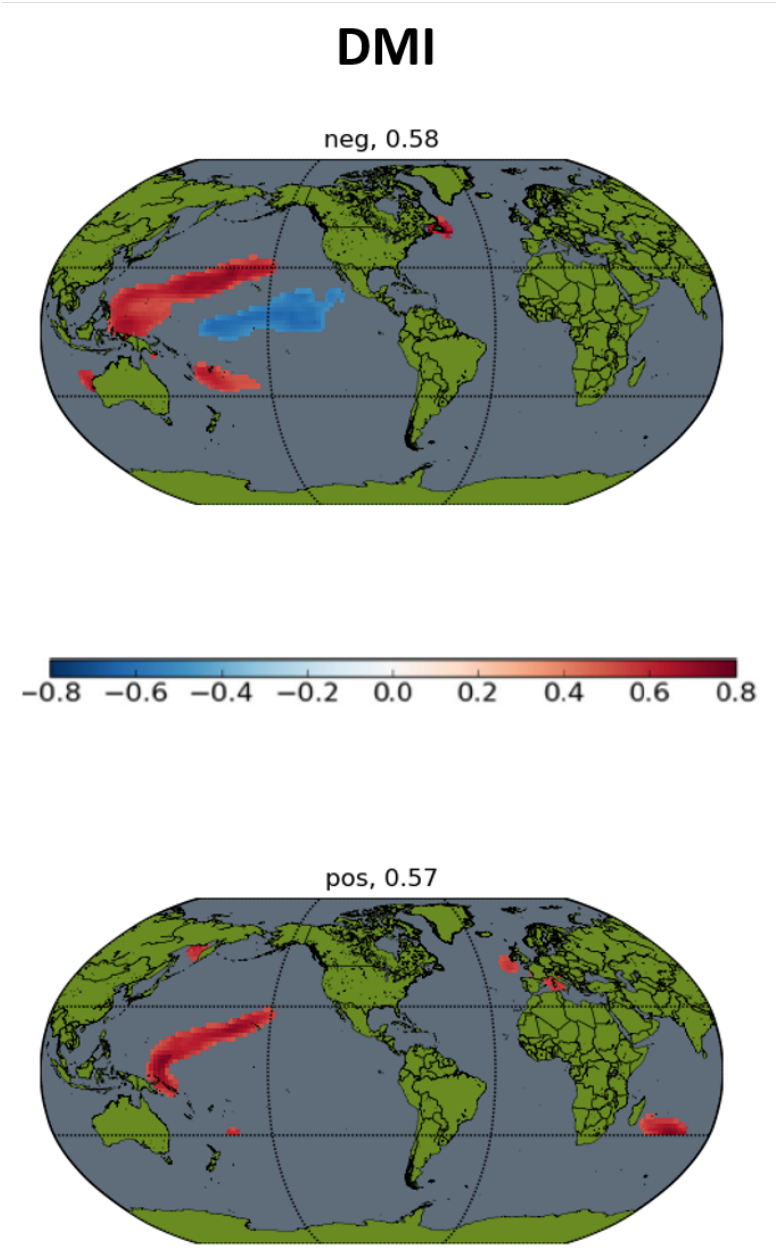

Figure A.18: Correlation maps between FMAM SST gridded anomalies and JJAS observed precipitation, generated by binning the years through DMI index.

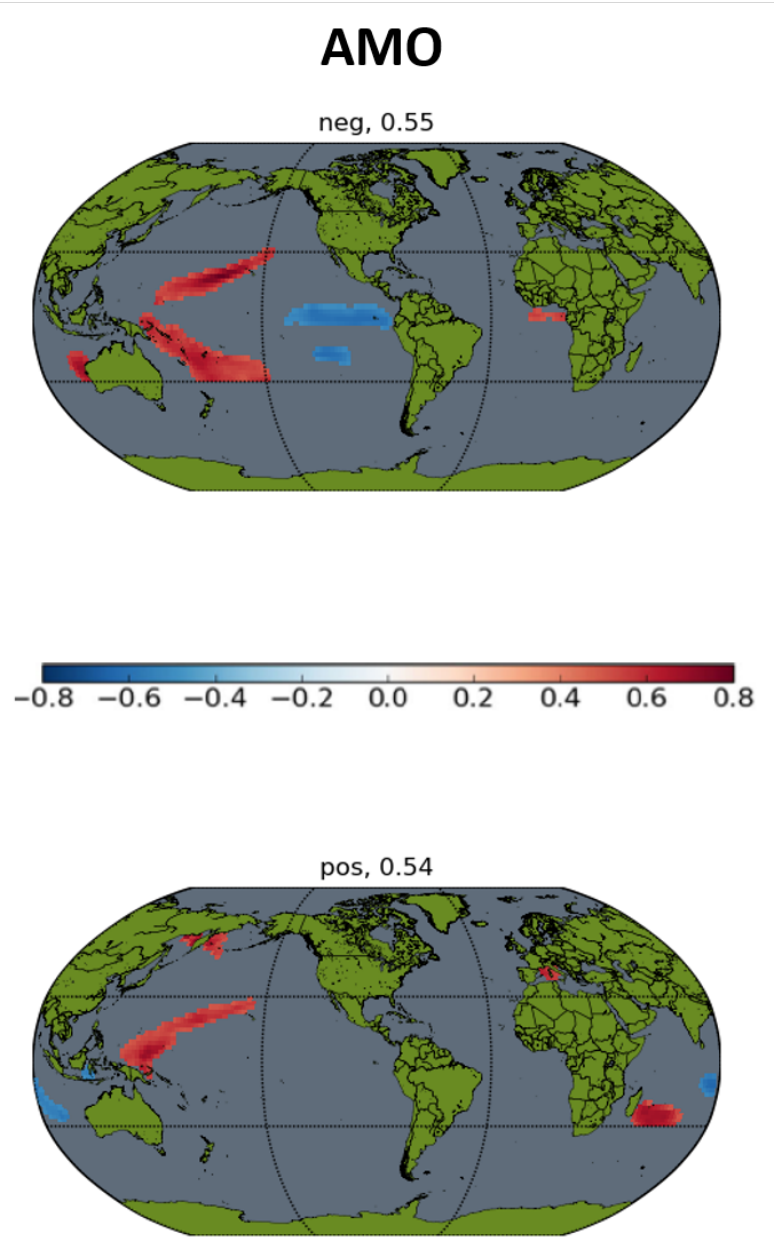

Figure A.19: Correlation maps between FMAM SST gridded anomalies and JJAS observed precipitation, generated by binning the years through AMO index.

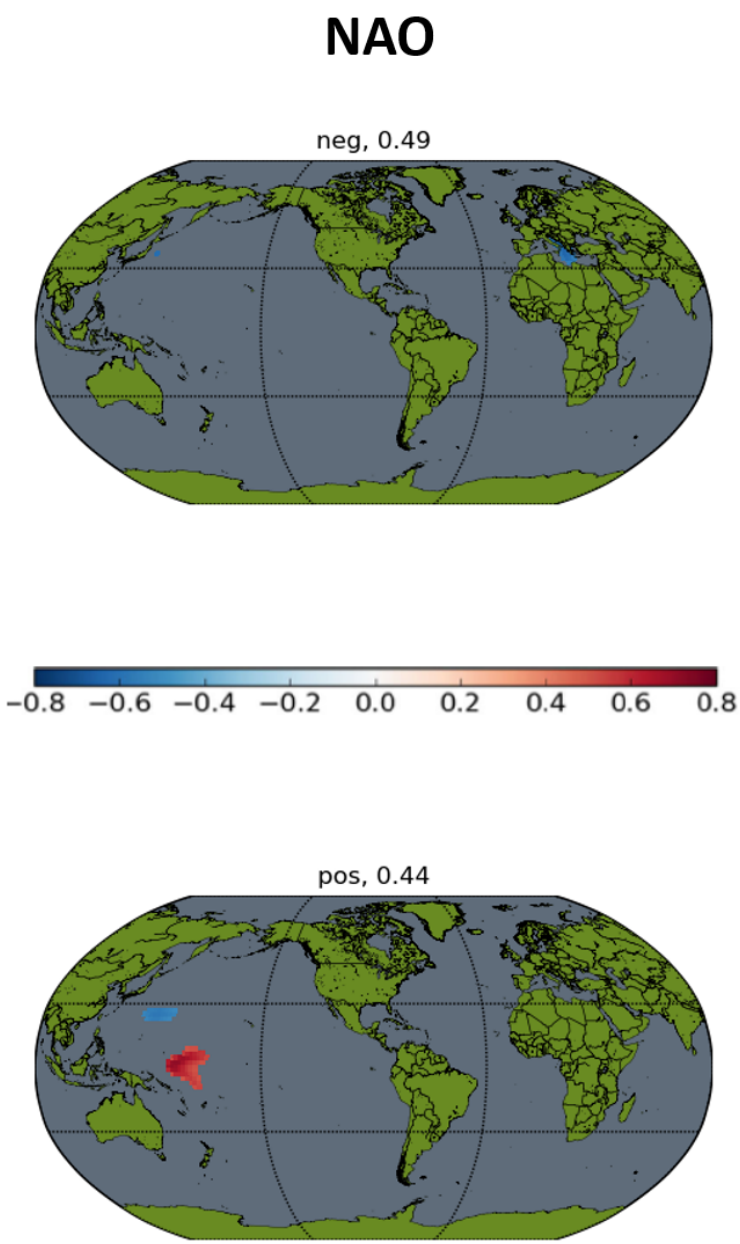

Figure A.20: Correlation maps between SOND SST gridded anomalies and JJAS observed SPEI, generated by binning the years through NAO index.

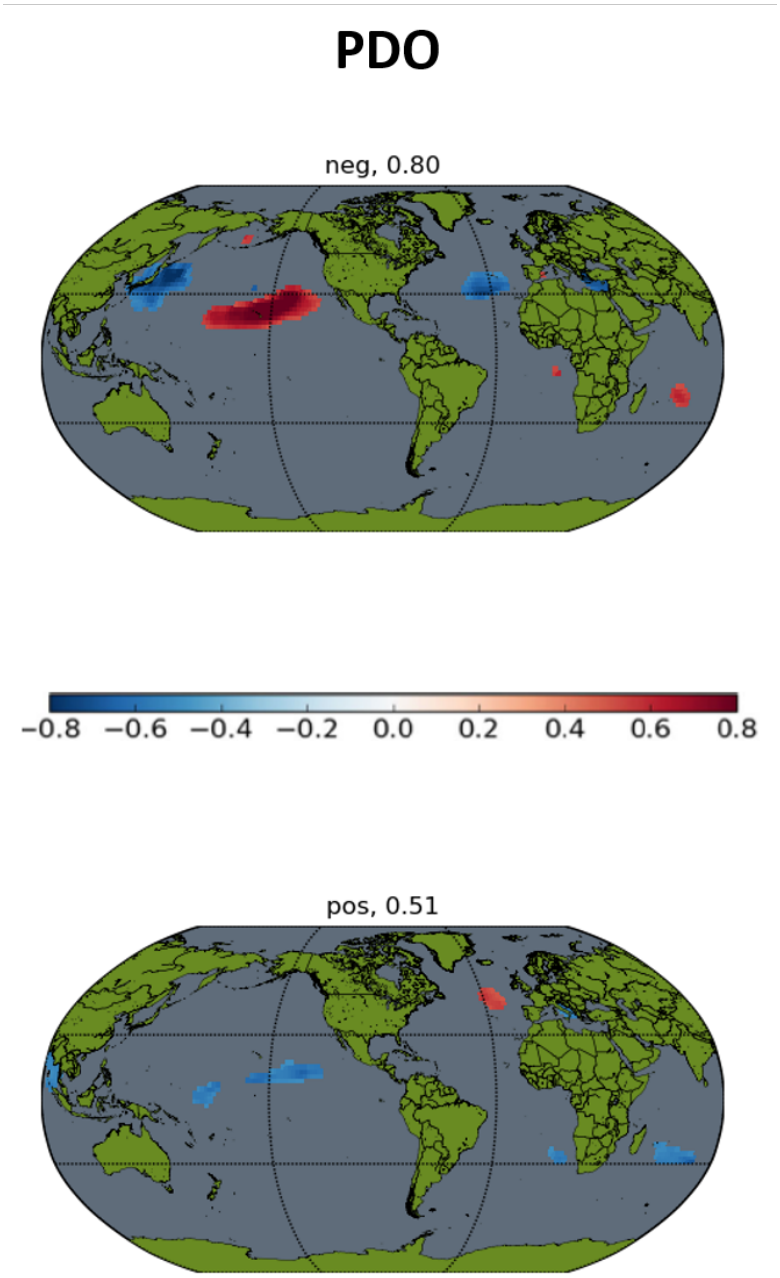

Figure A.21: Correlation maps between SOND SST gridded anomalies and JJAS observed SPEI, generated by binning the years through PDO index.

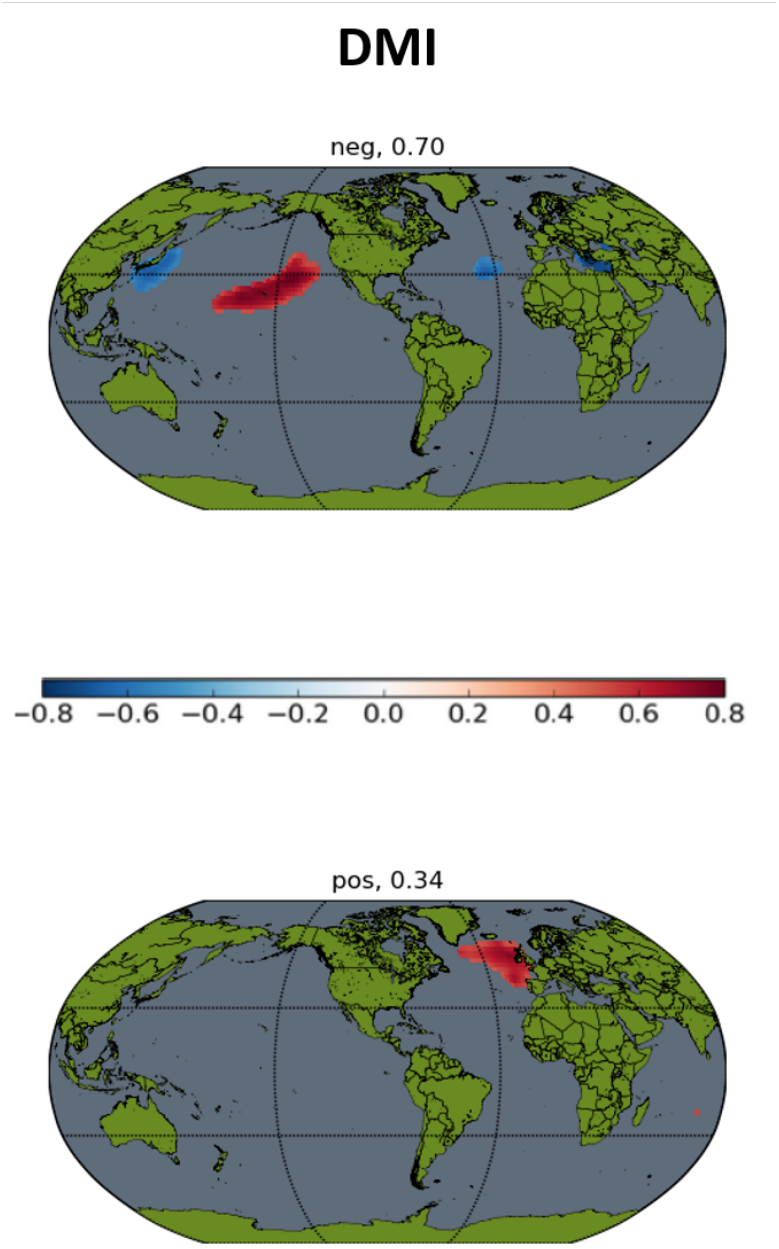

Figure A.22: Correlation maps between SOND SST gridded anomalies and JJAS observed SPEI, generated by binning the years through DMI index.

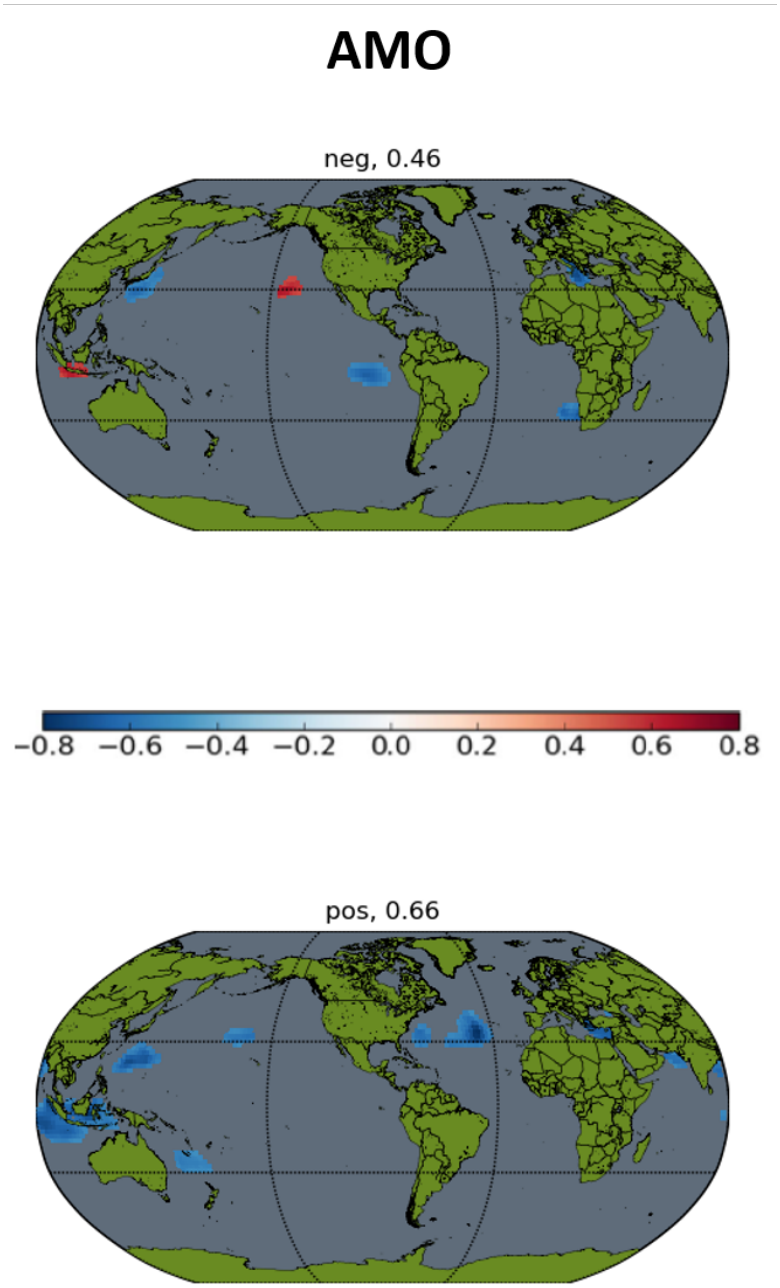

Figure A.23: Correlation maps between SOND SST gridded anomalies and JJAS observed SPEI, generated by binning the years through AMO index.

A.2.2 Multi-variate seasonal meteorological forecast

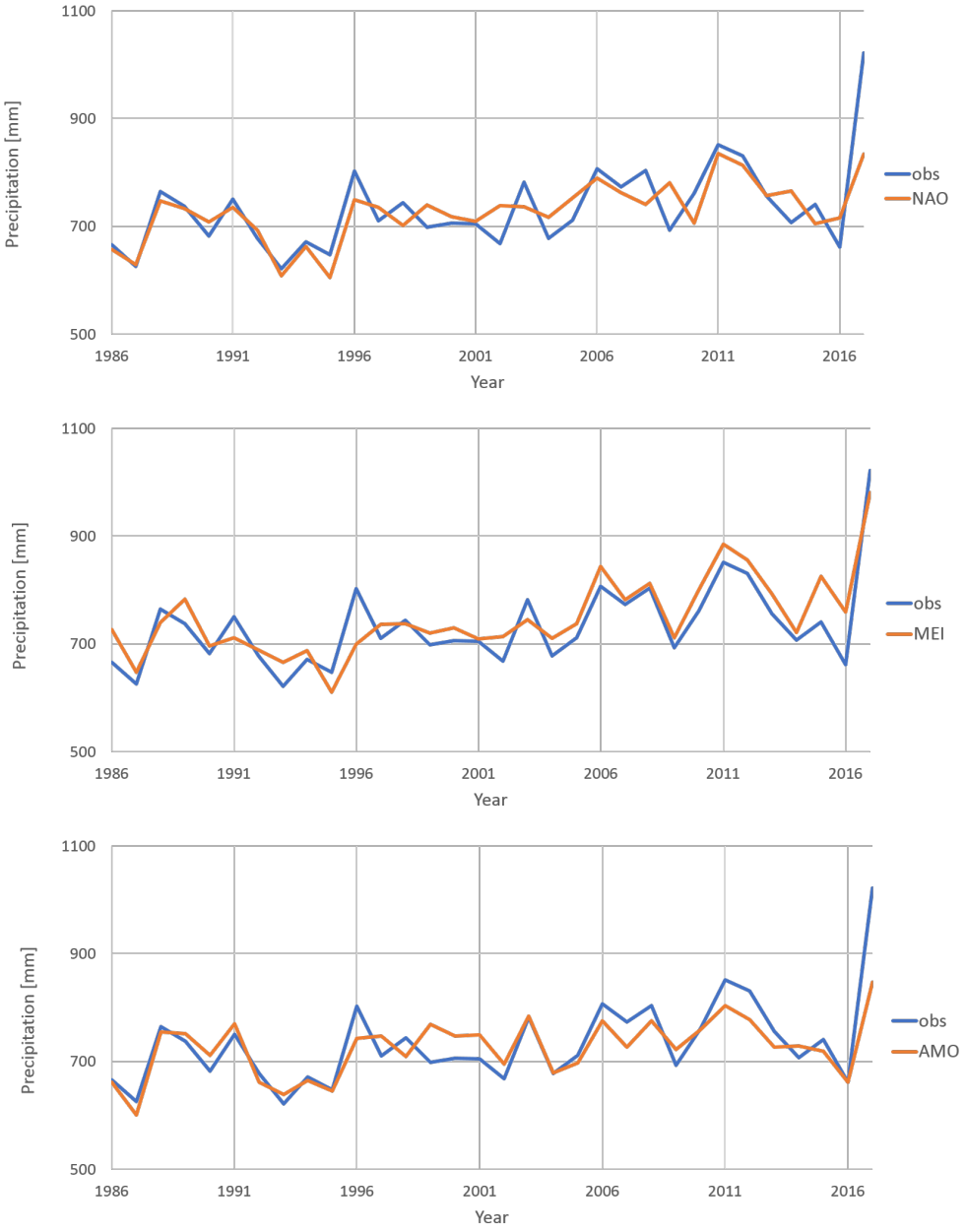

Figure A.24: Observed and predicted precipitation for univariate JJAS season: NAO (top), MEI (center), AMO (bottom).

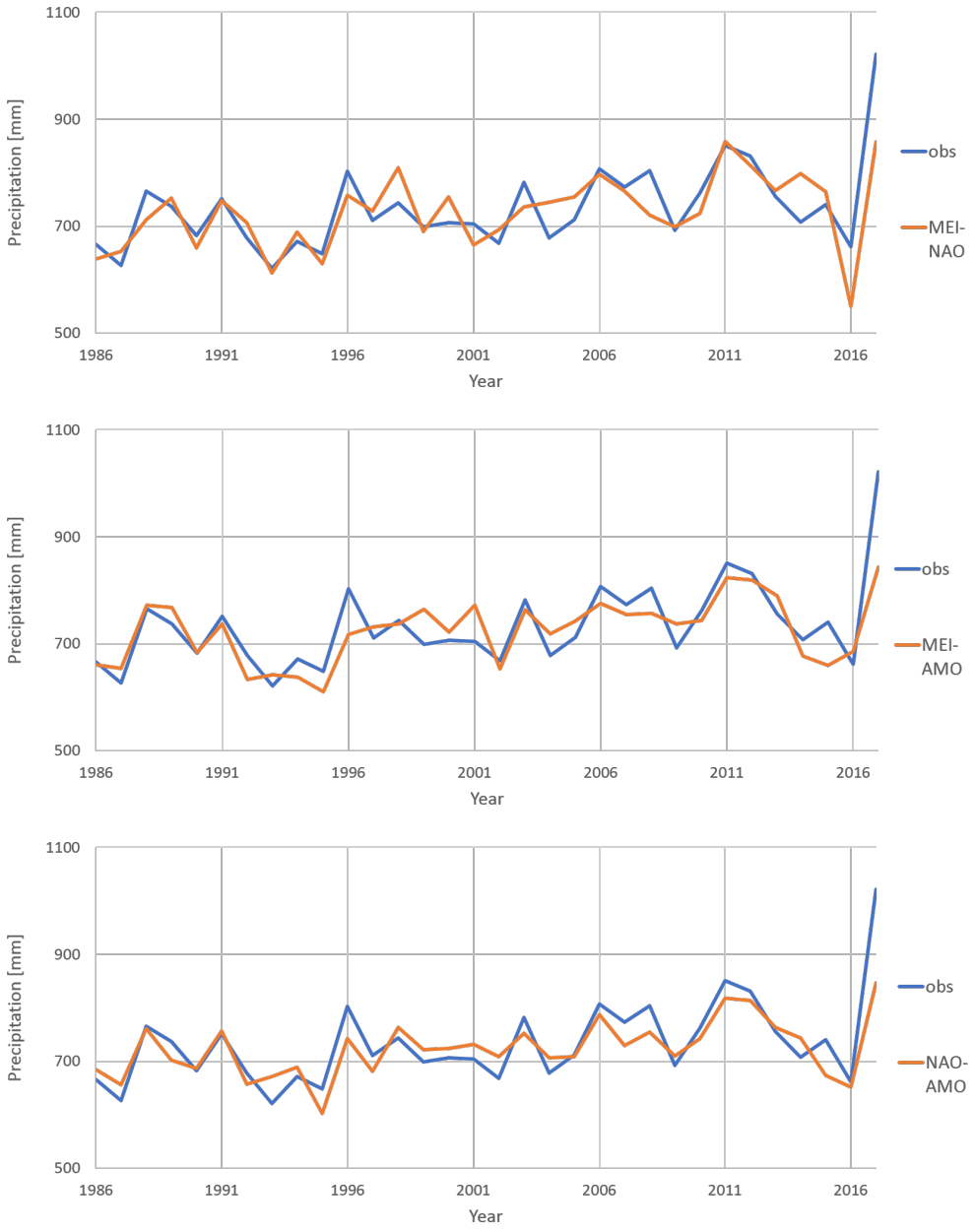

Figure A.25: Observed and predicted precipitation for bivariate JJAS season: MEI-NAO (top), MEI-AMO (center), NAO-AMO (bottom).

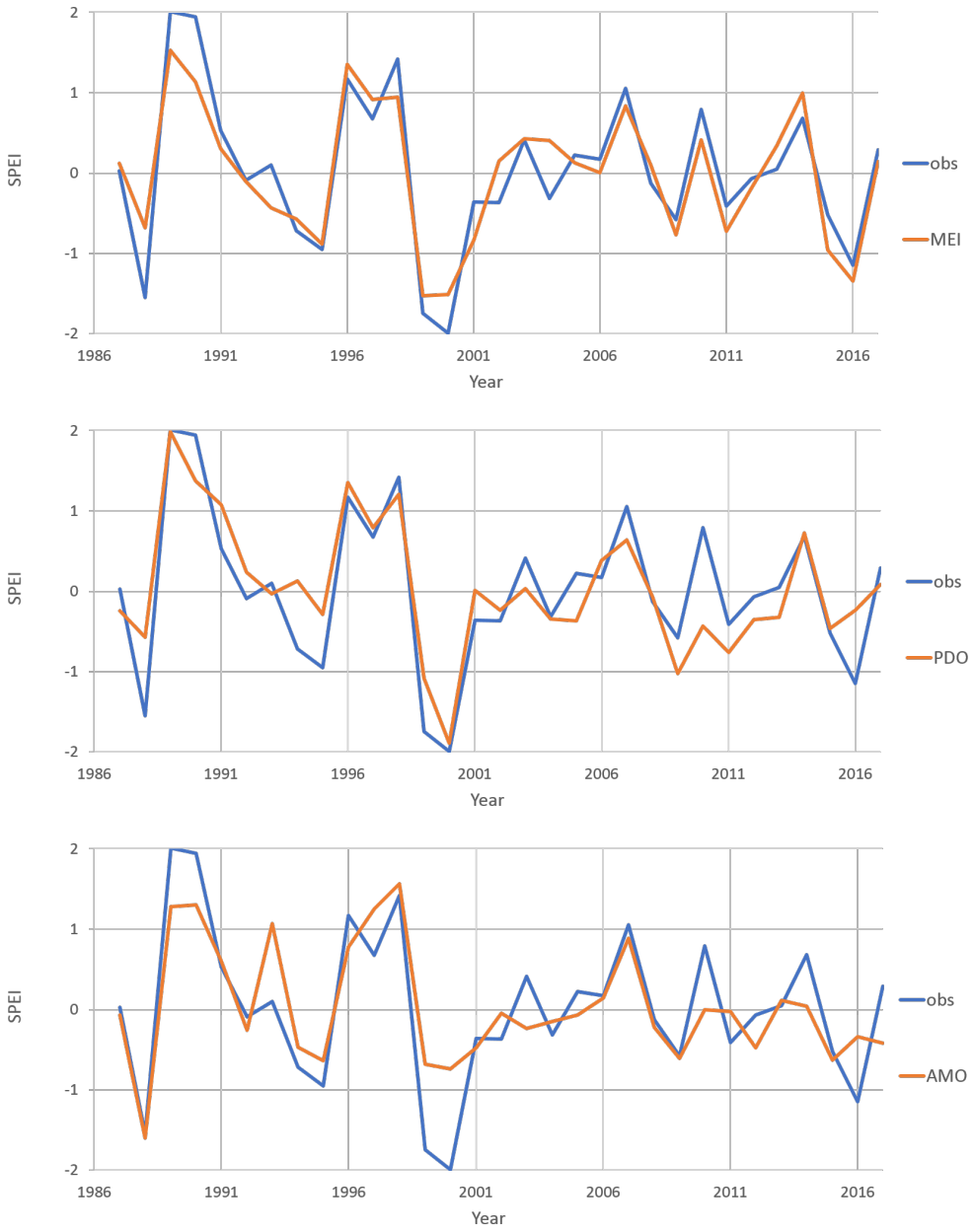

Figure A.26: Observed and predicted SPEI index for univariate JJAS season: MEI (top), PDO (center), AMO (bottom).

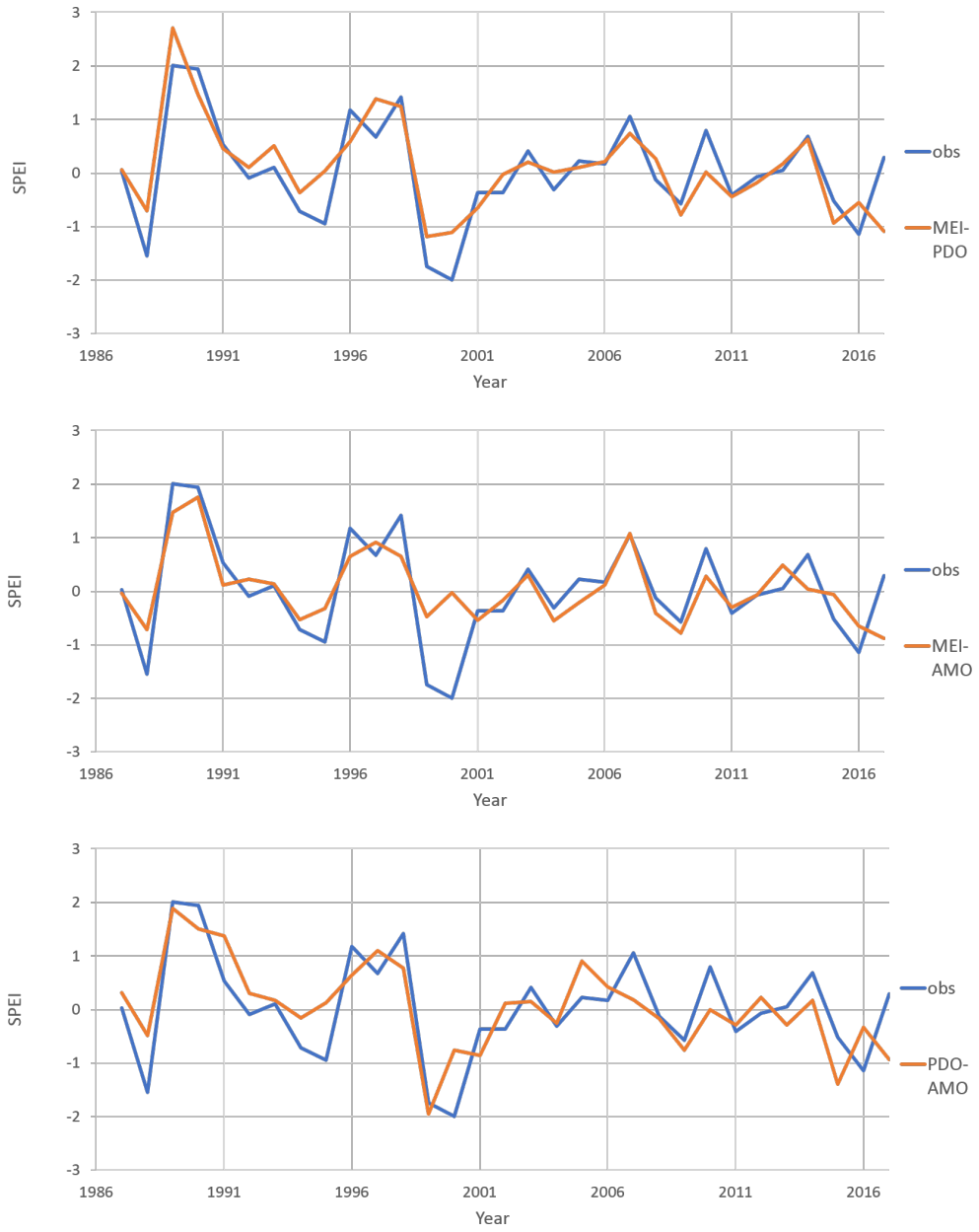

Figure A.27: Observed and predicted SPEI index for bivariate JJAS season: MEI-PDO (top), MEI-AMO (center), PDO-AMO (bottom).